Imperial College of Science, Technology and Medicine
Department of Computing

Hybrid optical and magnetic manipulation of microrobots

Maria Grammatikopoulou

Supervisor: Prof. Guang-Zhong Yang
Assistant Supervisor: Dr. Antoine Barbot

Submitted in part fulfilment of the requirements for the degree of Doctor of Philosophy in Computing of Imperial College and the Diploma of Imperial College, October 2019

Declaration

This thesis presents original work of the titled author. All material in this thesis which is not the author's original work have been referenced accordingly.

The copyright of this thesis rests with the author and its contents are licensed under a Creative Commons Attribution-Non Commercial-No Derivatives Licence. Researchers may copy and redistribute the material in any medium or format on the condition that; they credit the author, do not use it for commercial purposes and do not distribute modified versions of the work. When reusing or sharing this work, researchers should make the licence terms clear to others.

Abstract

Microrobotic systems have the potential to provide precise manipulation on cellular level for diagnostics, drug delivery and surgical interventions. These systems vary from tethered to untethered microrobots with sizes below a micrometer to a few microns. However, their main disadvantage is that they do not have the same capabilities in terms of degrees-of-freedom, sensing and control as macroscale robotic systems. In particular, their lack of on-board sensing for pose or force feedback, their control methods and interface for automated or manual user control are limited as well as their geometry has few degrees-of-freedom making three-dimensional manipulation more challenging. This PhD project is on the development of a micromanipulation framework that can be used for single cell analysis using the Optical Tweezers as well as a combination of optical trapping and magnetic actuation for reconfigurable microassembly. The focus is on untethered microrobots with sizes up to a few tens of microns that can be used in enclosed environments for *ex vivo* and *in vitro* medical applications. The work presented investigates the following aspects of microrobots for single cell analysis: i) The microfabrication procedure and design considerations that are taken into account in order to fabricate components for three-dimensional micromanipulation and microassembly, ii) vision-based methods to provide 6-degree-of-freedom position and orientation feedback which is essential for closed-loop control, iii) manual and shared control manipulation methodologies that take into account the user input for multiple microrobot or three-dimensional microstructure manipulation and iv) a methodology for reconfigurable microassembly combining the Optical Tweezers with magnetic actuation into a hybrid method of actuation for microassembly.

Acknowledgements

First and foremost, I would like to express my sincere gratitude to my supervisor Professor Guang-Zhong Yang for his support, guidance and encouragement for the past five years, during my Masters' and PhD studies. I am very grateful as he gave me the opportunity to be part of the Hamlyn Centre. Professor Yang shaped my understanding of the engineering problems in robotic surgery and, furthermore, gave me motivation through his innovative and pioneering ideas.

I would also like to thank Dr. Antoine Barbot for his assistance and his involvement in this PhD project. His expertise on microrobotics and his contribution was invaluable in shaping this PhD project.

My sincere thanks also goes to Dr. Lin Zhang who has been an excellent colleague. I learned a lot working along side of him, both during my Masters' and PhD at the Hamlyn Centre.

I would also like to thank Dr. Ebubekir Avci for helping me during the first months of my PhD and passing on his expertise on the Optical Tweezers and who, together with Prof. Yang's initiative, made me a part of their project. I would also like to further extend this thanks to Dr. Stamatia Giannarou for her useful advice during my time in the lab.

This experience would not have been the same if it wasn't for my colleagues and people I met throughout these years in the lab. Special thanks go to Mirek Janatka for his input, both on technical issues and for his moral support.

Contents

1 Introduction 1

1.1 Research Objectives 4

1.2 Thesis Overview 7

1.3 List of Publications 10

2 Literature Review 11

2.1 Robotic Systems in the Microscale 11

2.2 Applications 13

2.2.1 Cell Manipulation 14

2.2.2 Cell Characterization 14

2.2.3 Microfluidic Organs-on-chip 15

2.3 Microrobot Fabrication 17

2.3.1 2D/2D.5 Fabrication Methods 17

2.3.2 3D Fabrication Methods 18

2.3.3 Functionalization Methods 19

2.4 Visual Tracking and 3D Pose Estimation 20

2.4.1 Pose Estimation in the Macroscale 21

2.4.1.1 Depth Estimation 22

2.4.1.2 Orientation Estimation 22

2.4.2 Pose Estimation in the Microscale 23

2.4.2.1 Depth Estimation 23
2.4.2.2 Orientation Estimation 24
2.4.2.3 Pose Estimation Challenges in the Microscale Compared to the Macroscale 24
2.5 Manipulation and Control 25
2.5.1 Optical Tweezers 25
2.5.2 Optical Manipulation 26
2.5.2.1 Direct Manipulation 27
2.5.2.2 Indirect Manipulation 29
2.5.2.3 Multiple Object Manipulation 29
2.5.2.4 Haptic Feedback and Shared Control 30
2.5.3 Microassembly 31
2.5.3.1 Robotic Microassembly 32
2.5.3.2 Self-assembly and Reconfigurable Microassembly 33

3 Microrobot Fabrication 36
3.1 Two-photon Polymerization 37
3.2 Optical Microrobot Fabrication 38
3.2.1 Microrobot Design Considerations 40
3.2.2 Printing Power Effect on Feature Resolution 42
3.3 Hybrid Optical and Magnetic Microrobot Fabrication 44
3.3.1 Masking for Selective Metal Deposition 46
3.4 Microrobot Detachment 46
3.5 Conclusions 49

4 Three-Dimensional Pose Estimation of Optically Transparent Microrobots 52

4.1 Problem Definition 54
    4.1.1 Pose Estimation Problem in Microrobotics 54
    4.1.2 Microscope-Camera Model 54
    4.1.3 Image-Geometrical Model Registration 56
4.2 Microrobot 2D Position Detection 57
4.3 Microrobot Depth Estimation using Sharpness Measurements . 57
    4.3.1 Depth Reconstruction using Global Sharpness Model Approximation 58
        4.3.1.1 Global Sharpness Model Calibration 59
        4.3.1.2 Global Depth Reconstruction 59
    4.3.2 Depth Estimation using Local Sharpness Model Approximation 61
        4.3.2.1 Local Sharpness Model Calibration 62
        4.3.2.2 Optimization-based Local Depth Reconstruction 63
    4.3.3 Experimental Setup 64
    4.3.4 Microrobot Fabrication 65
    4.3.5 Experimental Results 65
        4.3.5.1 Depth Reconstruction using Global Sharpness Approximation Model 65
        4.3.5.2 Depth Reconstruction using Local Sharpness Approximation Model 67
4.4 Microrobot Depth Estimation using Convolutional Neural Networks and Recurrent Neural Networks 69
    4.4.1 Dataset Generation 70
        4.4.1.1 Data Collection 72
        4.4.1.2 Data Pre-processing 73

4.4.2 Depth Estimation Network Architecture 73
4.4.3 Experimental Setup 76
4.4.4 Experimental Results 76
4.4.4.1 Validation of Microrobot Depth Estimation using the CNN-LSTM Model 77
4.4.4.2 Results and Discussion 80
4.5 Microrobot Orientation Estimation 82
4.5.1 3D Model-based Orientation Estimation 82
4.5.1.1 Orientation Estimation with Online Template Generation 83
4.6 Microrobot Pose Estimation 83
4.6.1 Depth and Relative Orientation Estimation 84
4.6.2 Pose Estimation Network Architecture 85
4.6.3 Experimental Setup 87
4.6.4 Experimental Results 87
4.6.4.1 Test Set Validation 88
4.6.4.2 Results and Discussion 89
4.6.4.3 Comparison with VGG16 Feature Extraction Model Pre-trained on ImageNet 93
4.6.4.4 Results and Discussion 95
4.7 Conclusions 97

5 Optical Manipulation of Microrobots 100
5.1 Indirect Manipulation using Laser-driven Microrobots 101
5.1.1 Experimental Setup and Discussion 102
5.2 Gaze Contingent Control for Optical Micromanipulation . . . 104
5.2.1 System Overview 105
5.2.2 Gaze Contingent Controller 105

5.2.2.1 Eye Gaze Data Processing 106
5.2.2.2 Intention Recognition and Gaze Control . . . 107
5.2.2.3 Gaze Contingent Guidance Constraints 110
5.2.3 2D Position Detection 112
5.2.3.1 Template Matching for Spherical Object Tracking 112
5.2.3.2 Non-spherical Object Tracking 113
5.2.4 Experimental Setup 113
5.2.4.1 Microrobot Fabrication 114
5.2.5 Experimental Results 114
5.2.5.1 Gaze Contingent Controller Performance Assessment in Microassembly with 2D Visual Tracking 114
5.2.5.2 Results and Discussion 116
5.2.5.3 Manipulation of a 3D Microrobot and Template-based Orientation Estimation 117
5.2.5.4 Results and Discussion 119
5.3 Conclusions 119

6 Hybrid Optical and Magnetic Microrobots for Reconfigurable Microassembly 122
6.1 Reconfigurable Microassembly 123
6.2 Component Design and Fabrication 124
6.3 Microassembly Stages and Strategy 125
6.3.1 Assembly of Spherical Joint using the Magnetic Field . 125
6.3.2 Displacement of Assembly and Joint Rotation under the Magnetic Field using the Optical Tweezers 127

6.3.3 Disassembly of Spherical Joint under the Magnetic Field using the Optical Tweezers 127
6.4 System Dynamics 128
6.4.1 Optical Trapping Force 128
6.4.2 Viscous Drag 129
6.4.3 Thermal Force 131
6.4.4 Magnetic Force 132
6.4.5 Contact Force 133
6.4.5.1 Magnetic Force 134
6.4.5.2 Adhesion Force 134
6.4.6 Dynamic Model Assumptions 135
6.4.7 Dynamics of Individual Components before Assembly . 137
6.4.8 Dynamics of Assembled Kinematic Chain 137
6.4.8.1 Displacement Force 138
6.4.8.2 Disassembly Force 139
6.5 System Identification 140
6.5.1 Trapping Stiffness Estimation 140
6.5.1.1 Boltzmann Statistics Calibration Method . . 141
6.5.2 Drag Coefficient Estimation 142
6.6 Experimental Setup 143
6.7 Experimental Results 145
6.7.1 Reconfigurable Microassembly 145
6.7.1.1 Assembly of Spherical Joint using the Magnetic Field 145
6.7.1.2 Displacement of Assembly and Joint Rotation under the Magnetic Field using the Optical Tweezers 146

6.7.1.3 Disassembly of Spherical Joint under the Magnetic Field using the Optical Tweezers 147
6.7.2 System Identification 149
6.7.2.1 Trapping Stiffness Estimation 149
6.7.2.2 Drag Coefficient Estimation 153
6.7.3 Force Estimation 155
6.7.3.1 Displacement Force 159
6.7.3.2 Disassembly Force 159
6.8 Results and Discussion 161
6.9 Conclusions 168

7 Conclusions **169**

Permissions **175**

Bibliography **176**

List of Tables

1.1 Differences between macro and microscale robotic systems . . 2

2.1 Overview of micromanipulation systems for cell manipulation . 14

3.1 Nanoscribe's IP photoresist characteristics 39

4.1 Depth estimation model parameters 75
4.2 Metrics for validation of microrobot depth estimation 78
4.3 Pose estimation network parameters 86
4.4 Metrics for gear-shaped (left), cylindrical (middle) and helical microrobot (right) datasets 88
4.5 Metrics for proposed (left) and VGG16 pre-trained on ImageNet (right) models for the cylindrical microrobot dataset . . 94

5.1 Mean values and p-values of metrics for microassembly user experiment 116

6.1 Magnetic coil setup parameters 144
6.2 Drag force calibration parameters 154
6.3 Median of force and velocity norms for and corresponding laser power displacement force 160
6.4 Median of force norms and corresponding laser power for joint disassembly (all experiments) 162

6.5 Median of force norms and corresponding laser power for repeated joint disassembly motion 166

List of Figures

1.1 A conceptual experimental setup of an Optical Tweezers system as a master-slave robotic platform for cell manipulation. The slave component consists of the Optical Tweezers with an integrated magnetic setup placed on the piezo stage (right). Enclosed experimental environments, such as a microfluidic chip or a biological sample can be place on the sample holder for testing. The sample can be imaged through the microscope-camera system and is displayed to the operator. The master component consists of a pair of haptic devices and other devices that process the operator's sensory information, such as an eye-tracker (left). 6

2.1 Some of the microrobotic systems for cell manipulation. (a) Optical Tweezers (b) Magnetic tweezers (c) Atomic force microscopy probe (c) Mechanical micromanipulator with force sensor on tip 13

2.2 (a) A schematic of two microbeads attached to a red blood cell to characterize its mechanical properties (b) A schematic of microfluidic channels using Optical Tweezers for cell sorting 15

2.3 3D-printed microrobots used as grasping mechanisms inside an Optical Tweezers setup 18

2.4 A schematic of Optical Tweezers laser beam with a spherical object attracted towards the focus of the laser 26

3.1 Two-photon polymerization principle 37
3.2 Printing configurations 38
3.3 Rendering of the geometrical model of the two-component rotational joint (left) and of the cylindrical microstructure with cover (right) 39
3.4 Batch fabrication of microstructures. Array of cylindrical microrobots with rectangular covers (left) and an array of rotational joint microrobots (right) 41
3.5 Effect of printing power on feature resolution (20 %- 30%) . . 42
3.6 Effect of printing power on feature resolution (50 %- 55%) . . 43
3.7 Rendering of the geometrical model of the cylindrical microrobot with spherical handle and spherical tips 45
3.8 Rendering of the geometrical model of the cylindrical microrobot with one spherical handles and rectangular tips 45
3.9 Rendering of the geometrical model of the microstructures with masks for metal deposition 47
3.10 Cylindrical microrobots with rectangular (left) and spherical (right) tips with covers on top of spherical handle 48
3.11 Partially detached microrobot (only rotating part) (a) and fully detached microrobot (b) using sonication 48
3.12 Geometrical model rendering and microscope image in an Optical Tweezers setup of hybrid optical and magnetic microrobots 49

4.1 The projection model that describes the microscope-camera system (a). The three-dimensional motion results in out-of-focus point on the image (b). An example set of images shows a microrobot as projected on the image plane in different depths along the z-axis, which gives a focused (c-middle) and defocused (c-left and right) images. 55
4.2 An indicative image frame with the registered projection of the geometrical model (left). A rendering of the geometrical model (bottom right) and the image frame with which the CAD model is registered (top right) 56
4.3 Sharpness measurement and ground truth trajectory used in calibration for mapping function approximation 60
4.4 Global sharpness model approximation from calibration (top). Inverse sharpness models (bottom) 61
4.5 Local sharpness model approximations using one Gaussian curve (left). The windows and the corresponding local object pose are also shown. The sharpness values as calculated for each of the selected features (right) 62
4.6 The Optical Tweezers experimental setup. The 3D-printed microrobot array was translated using the piezo stage and was imaged through the camera-microscope system. 64
4.7 Global sharpness measurement using the Gaussian Derivative and the corresponding images from the performed experiment 66
4.8 The estimated trajectory (blue) and the ground truth trajectory of the piezo stage (red) 66

4.9 An example of local feature depth estimation using the optimization based approach. A set of local windows located at a corner feature (top) are used to calculate the sharpness (middle) of the windows. The estimated and stage relative depth (bottom) shows that the proposed method can be used to estimate local depth information as long as the changes of sharpness can be detected. 67

4.10 Indicative frames from the generated datasets. Three geometries are used for training and validation: The first is a gear-shaped microrobot, the second a cylindrical microrobot with three spherical handles and the third one a helical microrobot. 71

4.11 Example learned feature maps generated from the first, second and third pair of convolutional and max-pooling layers of the trained network for a given input image. A colormap is used to outline the different intensities within each map. 74

4.12 An overview of the proposed architecture. The network consists of five convolutional layers for feature extraction and one LSTM cell which estimates the depth of the microrobot. . . . 75

4.13 The validation results showing the sequence in which the data is given as input to the network (top). A histogram of the error distribution shows the range of error between the prediction and the ground truth for the test set (bottom). 78

4.14 A more detailed overview of the predicted trajectories. The figures depict the prediction (blue) in comparison to the ground truth depth (red). The dashed lines separate the trajectories that correspond to different microrobot 3D orientations as stated in the figure. 79

4.15 Trajectory reconstructions of microrobots with different orientations following the same trajectory 80
4.16 The proposed network architecture. The model consists of a network for relative orientation estimation and one for depth estimation using as input two image frames. 85
4.17 Estimated and ground truth of the relative orientations for the cylindrical microrobot dataset 89
4.18 Estimated and ground truth values of the absolute orientations and depth for the gear-shaped microrobot 90
4.19 Estimated and ground truth values of the absolute orientations and depth for the cylindrical microrobot 91
4.20 Estimated and ground truth values of the absolute orientations and depth for the helical microrobot 92
4.21 Estimated and ground truth values of the absolute orientations and depth for the cylindrical microrobot using the proposed and VGG16-ImageNet pre-trained networks 94
4.22 Estimated and ground truth values of the relative orientations for the cylindrical microrobot using the proposed and VGG16-ImageNet pre-trained networks 95
4.23 Estimated and ground truth values of the relative orientations about the x-axis for the cylindrical microrobot using the proposed and VGG16-ImageNet pre-trained networks 96

5.1 A view of two rotational joints used for indirect grasping inside an Optical Tweezers setup (left). The two microrobots grasping an 8 μm microsphere (right) 102
5.2 Downwards displacement of microsphere using single optical trap actuation of the fully detached rotational joint 103

5.3 Upwards displacement of microsphere using single optical trap actuation of the fully detached rotational joint 103
5.4 The system hardware components: The haptic devices, the eye tracking device, the computer screen displaying the live camera feed and the Optical Tweezers (from left to right). . . 106
5.5 The original and processed camera feeds 107
5.6 Geometrical model of the microstructure used in the second experiment 110
5.7 Registered projection of geometrical model (left) and initial pose with respect to global frame (right) 111
5.8 The operator view during the performed experiments (left). The processed image feed displaying the detected microspheres (red) and the candidate target position as calculated from the operator's gaze (right) 112
5.9 Duration for first assembly [s] 115
5.10 Duration for second assembly [s] 115
5.11 Total duration for task [s] 115
5.12 Distance over time [μm s] 115
5.13 (a) Initial orientation of microrobot with respect to global frame as viewed from the XY plane (b) Final orientation of microrobot with respect to global frame as viewed from the XY plane (c) Trajectory of x-axis of object frame (d) Trajectory of y-axis of object frame (e) Trajectory of z-axis of object frame 118
5.14 Rotation angles of the z,y and x axis of the object frame (θ_z, θ_y and θ_x) with respect to global frame 118

6.1 Rendering of the CAD models of assembly components 124

6.2 Components before and after they are assembled under the magnetic field 126
6.3 3D and 2D views of assembled kinematic chain under the magnetic field 126
6.4 The experimental setup comprises an Optical Tweezers with an integrated set of magnetic coils placed fitted on the sample holder on the piezo stage. 143
6.5 Schematic of the side view of the experimental configuration of the samples placed inside the coils and on the Optical Tweezers (left). Top view of the coils placed on the piezo stage with a glass slide containing microrobots (right). 144
6.6 Assembly of spherical joint 146
6.7 Displacement of assembly along the y-axis 147
6.8 Out-of-plane displacement of end-effector from vertical force induced but the laser 147
6.9 Disassembly of spherical joint using the Optical Tweezers under the magnetic field 148
6.10 Disassembly of the kinematic chain after deactivation of the magnetic field 148
6.11 Global frame of reference {G} and microrobot co-ordinate frame {M} 149
6.12 Relative displacement of the microrobot with respect to the mean displacement along the x-axis from Brownian motion for different laser powers 150
6.13 Relative displacement of the microrobot with respect to the mean displacement along the y-axis from Brownian motion for different laser powers 151

6.14 Probability distribution for Brownian motion displacements for different laser powers (x-axis) 152
6.15 Probability distribution for Brownian motion displacements for different laser powers (y-axis) 153
6.16 Parabolic function fitting for different laser powers (x-axis) . . 154
6.17 Parabolic function fitting for different laser powers (y-axis) . . 155
6.18 Trapping stiffness and position standard deviation as function of laser power (x-axis) 156
6.19 Trapping stiffness and position standard deviation as function of laser power (y-axis) 156
6.20 Indicative image frames from the drag coefficient calibration experiments 157
6.21 Optical trap and microrobot positions along the x and y-axis . 157
6.22 Microrobot velocity along the x and y-axis for the drag coefficient calibration experiments 158
6.23 Drag force exerted on the microrobot along the x and y-axis for the drag coefficient calibration experiments 158
6.24 Trapping force for assembly displacement for each experiment 160
6.25 Drag force for assembly displacement for each experiment . . . 161
6.26 Total displacement force for each experiment 162
6.27 Trapping force for disassembly for each experiment 163
6.28 Drag force for disassembly for each experiment 163
6.29 Total force for disassembly for each experiment 164
6.30 Trapping force for disassembly for repeated disassembly on same experiment 164
6.31 Drag force for disassembly for repeated disassembly on same experiment 165

6.32 Total force for disassembly for repeated disassembly on same experiment 165

Chapter 1

Introduction

Minimally invasive surgery has shown many advantages compared to traditional surgical techniques, such as reduced blood loss and faster patient recovery [1]. These improvements along with advances in robotics have led to the development of medical systems for minimally invasive surgical interventions. In contrast to industrial robotic systems, medical robots operate with high precision in confined anatomical spaces and highly dynamic environments. Currently available platforms, mainly of master-slave architecture such as the da Vinci® Surgical system, provide tools that allow greater dexterity in manipulation, a three-dimensional (3D) view of the anatomy and master control interfaces that improve ergonomics for the surgeon, compared to traditional minimally invasive surgery. One of the main challenges in medical robotics is miniaturization to further facilitate precision below the millimeter scale. This challenge and potential capabilities become even greater when systems move towards further miniaturization reaching the lower limits of the microscale.

Microrobotic systems have been proposed as an emerging technology that could revolutionize diagnosis, therapy and surgical interventions as they allow

	Macroscale robots	Microrobots
Dominant forces	Gravity and inertia	Adhesion and surface tension
Feedback methods	Encoders, 2D and 3D vision	2D microscope view
Degrees of Freedom	Redundancy	Insufficient for 3D manipulation
User Input	Master-slave systems, haptic devices	Video game controllers, mouse input

Table 1.1: Differences between macro and microscale robotic systems

interventions at cellular level [2].

Microrobots can be divided into tethered and untethered microrobots depending on the application and function they need to perform. Tethered microrobots are attached to a power source, an example of which are tethered microgrippers [3]. In contrast, untethered microrobots are mobile and powered externally. Consequently, they are suitable for enclosed environments where a mechanical connection to the microrobot cannot be established due to workspace restrictions, such as in microfluidic chips or anatomical spaces. Microrobot applications, due to their small scale, range from early disease diagnosis to precision microsurgery [4]. In particular, they have been proposed for *in vivo* targeted drug delivery [5] and cellular level surgery [6]. They are also a suitable tool for *ex vivo* applications aiming at early disease detection through cell biopsy. Optical Tweezers is one of the main microrobotic system for characterizing mechanical properties of cells, usually combined with fluorescence imaging and microfluidics [7, 8]. Another interesting area of application is *in vitro* cell manipulation, such as tissue engineering and cell assembly. Artificial tissue for tissue regeneration and graphing could be constructed by assembling cells in specific geometries outside of the body [9]. Cell assembly is also crucial as arranging cells in predefined geometries can give insights in investigating cancer progression [10]. These procedures are currently performed manually with simplistic tools, but precision and dexterity would greatly benefit by the development of robotic systems that facilitate these tasks. The aspiration is to develop microrobotic systems with comparable capabilities in their design, sensing and control aspects as macroscale medical robotic systems. Therefore, the focus of this thesis is to investigate the development of microrobotic systems for closed environments with the Optical Tweezers as their main source of actuation for *ex vivo* and *in vitro* applications that could be potentially used in devices such as microfluidic organs-on-chip for cell manipulation.

1.1 Research Objectives

The aim of this thesis is to investigate and address some of the engineering challenges of developing a microrobotic system for *ex vivo* and *in vitro* applications. The proposed methods are built around Optical Tweezers manipulation as they present fine precision and submicron spatial resolution making them suitable for micromanipulation of microstructures with sizes up to a few tens of microns. The challenges that are investigated in this thesis are: i) Fabricating 3D microrobots for micromanipulation, ii) how to sense microrobot position and orientation using the camera feedback, iii) developing a shared control strategy for bimanual optical micromanipulation of multiple or 3D microrobots and iv) combining optical and magnetic actuation for microassembly.

Microrobot fabrication for optical and hybrid optical and magnetic micromanipulation

Optical Tweezer's main limitations are that trapping relies on cell properties and, most importantly, cause photodamage to cells when directly grasped by the optical trap [11]. Additionally, a conventional Optical Tweezers setup is capable only of two-dimensional (2D) manipulation. These limitations could potential be addressed by fabricating or assembling 3D optically transparent microrobots than can be used to grasp microstructures or cells indirectly.

Sensing microrobot's position and orientation

Macro and microscale medical systems share a common constraint, that they are limited in their sensing aspect. This is due to scaling of the technology in the microscale and clinical restrictions in macroscale, such as sensor sterilization in surgical tools. *Ex vivo* and *in vitro* microrobotic experimental setups however have a camera, as macroscale robot systems provide an endoscopic view. Therefore, such microrobot setups rely on the camera view as their main sensing modality. Taking advantage of the fact that there is direct line of sight to the microrobot workspace, the camera feedback can be used to implement computer vision algorithms for 3D microrobot pose estimation. This would lead to providing a form of pose feedback for improved user perception and development of closed-loop control techniques.

Microrobot bimanual optical manipulation

While Optical Tweezers are capable of multiple microrobot manipulation by generating patterns of multiple optical traps, they currently provided limiting control interfaces. Current control interfaces of available micromanipulator systems allow user input through 2D mouse position or video game controllers. Consequently, bimanual task execution is challenging and requires increased user effort due to the limitations of the input devices. Therefore, one of the research objectives of this thesis is to investigate how bimanual control of mutliple microrobots can be achieved integrating human sensory information, such as the operator's gaze information, and haptic guidance.

Hybrid optical and magnetic microrobot manipulation for microassembly

Optical Tweezers can realize multiple microrobot manipulation using multiple optical traps, a property which is important for microassembly. It is of interest, therefore, to investigate how reversible microassembly could be performed *in situ* integrating magnetic actuation to be used for microassembly. Having these components integrated in one framework would lead to the

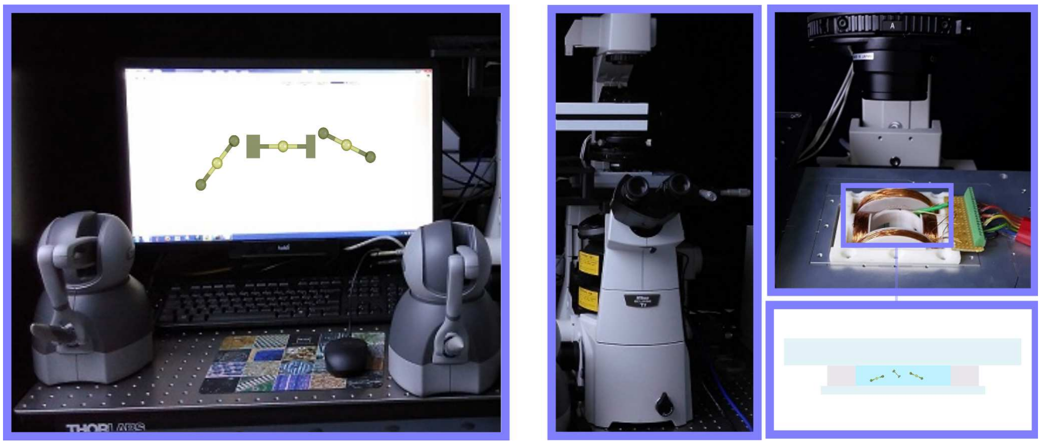

Figure 1.1: A conceptual experimental setup of an Optical Tweezers system as a master-slave robotic platform for cell manipulation. The slave component consists of the Optical Tweezers with an integrated magnetic setup placed on the piezo stage (right). Enclosed experimental environments, such as a microfluidic chip or a biological sample can be place on the sample holder for testing. The sample can be imaged through the microscope-camera system and is displayed to the operator. The master component consists of a pair of haptic devices and other devices that process the operator's sensory information, such as an eye-tracker (left).

development of a microrobotic system that allows 3D manipulation of microrobots with 3D visual-based microrobot position feedback combining two methods of external actuation which are suitable for micromanipulation in closed environments. From this point of view, such microrobot systems can be seen as master-slave robotic systems, similarly to medical robotics platforms. An indicative depiction of these components as a master-slave system can be seen in Figure 1.1. In this case, the integrated Optical Tweezers with magnetic actuation can be considered the slave component while the master side consists of a pair of haptic devices and additional devices such as the eye-tracker that is used to integrate human sensory information in the control loop.

1.2 Thesis Overview

The outline of this thesis is structured as follows:

Chapter 2 gives an overview of the current state-of-the-art of microrobotic systems for *ex vivo* and *in vitro* applications, followed by a review of their engineering aspects on microrobot fabrication, microrobot visual tracking and control strategies for optical micromanipulation. Last, an overview and the current state of microassembly techniques is given.

Chapter 3 describes the microfabrication procedure that is followed to fabricate optically transparent and hybrid optical and magnetic microrobots. The microstructures were characterized to assess the impact of parameters, such as the printing power, on feature resolution. Two detachment methods are presented assessing their effectiveness for batch microrobot detachment.

Chapter 4 investigates microrobot pose estimation using the microscope-camera feedback. Two methods for depth estimation of transparent microrobots using image sharpness measurements and model-based tracking are initially investigated. Following an assesment of these two methods, a depth estimation method is presented based on supervised learning for optically transparent microrobots of known geometry. This methodology uses Convolutional Neural Networks (CNNs) combined with a Long Short-Term Memory (LSTM) cell for depth regression. Estimating microrobot orientation is also investigated, proposing a template-based method. A vision-based method combining depth and 3D orientation using CNNs is proposed in a unified model. The model is trained and validated using microscope images and ground truth data generated from 3D-printed microrobots imaged in an Optical Tweezers setup and compared to previously proposed neural network architectures.

Chapter 5 investigates micromanipulation of optical transparent microrobots. Section 5.1 demonstrates how 3D multiple component optical microrobots can be used as grasping mechanisms for micromanipulation. Section 5.2 presents a gaze contingent control framework for optical micromanipulation. The framework comprises a strategy to recognize the operator's intentions in order to interactively place and reconfigure the optical traps using the operator's eye fixation point and haptic constraints generated from the user's eye gaze to assist positioning of the assembled microstructures. A set of experiments is performed in order to assess task completion using the proposed control framework and the standard Optical Tweezers control mode.

Chapter 6 proposes a microassembly technique that relies on hybrid optical and magnetic actuation. This method is based on creating mechanisms *in situ* using the magnetic attractive force as the assembly mechanism. The fundamental structural elements used for assembly can by actuated simultaneously by the Optical Tweezers and the magnetic field. The magnetic field if used to induce the attractive force between the components while the Optical Tweezers is used for actuation. It is demonstrated that the assembly can be reversible. An estimation of the force required for component disassembly is experimentally calculated.

The key contribution of the thesis are:

- Fabricating hybrid optical and magnetic microrobots that can be actuated simultaneously by the Optical Tweezers and the magnetic field.
- Developing a vision-based strategy for three-dimensional pose estimation of 3D-printed microrobots using state-of-the-art computer vision methods. A labelled dataset of microscope images of microrobots of different geometries was also generated in an Optical Tweezers setup.
- Proposing a control strategy for bimanual manipulation of multiple microrobots using the operator's sensory information to facilitate control of multiple or 3D microrobots.
- Introducing a setup that integrates Optical Tweezers and magnetic actuation and a methodology for reconfigurable microassembly based on optical and magnetic actuation. A design of hybrid optically and magnetically actuated microrobots is also proposed to create *in situ* multiple component 3D microassemblies in enclosed environments.

1.3 List of Publications

Contents of this thesis are presented in the following publications:

- **M. Grammatikopoulou** and G-Z. Yang. "Three-Dimensional Pose Estimation of Optically Transparent Microrobots", IEEE Robotics and Automation Letters (RA-L), (2019)
- **M. Grammatikopoulou**, L. Zhang and G-Z. Yang. "Depth Estimation of Optically Transparent Microrobots Using Convolutional and Recurrent Neural Networks," 2018 IEEE/RSJ International Conference on Intelligent Robots and Systems (IROS), Madrid pp. 4895-4900, (2018)
- **M. Grammatikopoulou**, L. Zhang and G-Z. Yang, "Depth estimation of optically transparent laser-driven microrobots," 2017 IEEE/RSJ International Conference on Intelligent Robots and Systems (IROS), Vancouver, BC, pp. 2994-2999. (2017)
- **M. Grammatikopoulou** and G-Z. Yang. "Gaze contingent control for optical micromanipulation," 2017 IEEE International Conference on Robotics and Automation (ICRA), Singapore, pp. 5989-5995, (2017)
- E. Avci, **M. Grammatikopoulou**, and G-Z. Yang. "Laser-Printing and 3D Optical-Control of Untethered Microrobots", Advanced Optical Materials, 5(19), p.1700031. (2017)

Chapter 2

Literature Review

2.1 Robotic Systems in the Microscale

The use of microrobots for manipulation on cellular level has a range of application in medical research, in diagnostics and potentially in minimally invasive surgery. For these applications, the precision and manipulation capabilities of the system are critical and require sensing and user interfacing that allow the user to interact with cells in 3D. In order to have a system with manipulation capabilities comparable to macroscale robotic systems, the components that need to be developed are the following: i) the design of 3D microrobots that allow 6-degree-of-freedom (DoF) manipulation, ii) the 3D visual feedback that provides the operator with a better understanding of the object pose in the 3D space and which is also necessary for closed-loop control, iii) the control software that allows 3D object manipulation accounting for the unknown to the user dynamics and iv) developing a setup that provides 3D actuation to facilitate tasks such as microassembly. Microrobotic platform that are used for cell manipulation and as sensing mechanisms are the Optical Tweezers, the magnetic tweezers, atomic force microscopy probes and mechanical micromanipulators (Figure 2.1). The choice on the system depends on their spatial resolution and exerted force range as well as their footprint [12]. Table 2.1 gives the spatial resolution and force range for each of these systems. Mechanical micromanipulator systems can exert larger forces, however, due to their footprint and that they are attached to a power source, they cannot be placed in enclosed environments, such as microfluidic chips. Optical Tweezers are capable of actuating microrobots externally in a closed workspace with high precision due to their spatial resolution. For cell sizes is up to a few tens of microns, they could potentially be a suitable solution for 3D micromanipulation at this scale for single cell analysis and cell biopsies.

The following review investigates the state-of-the-art in these four aspects of microrobotic systems. The investigation in this thesis is done from a system and engineering point of view, rather than investigating the materials and biological aspects of microrobotic systems. The conducted review discusses the fabrication techniques, the computer vision aspect of the systems and how the microscope-camera system is used for position feedback, the control methods of the microrobotic systems previously developed for cell manipulation and last how microassembly is performed. Systems on specific application scenarios are also presented in order to illustrate their functionality and the research issues that are emerging from the potential medical use. The majority of the research which is presented is on the Optical Tweezers. The following of the review describes the main application of Optical Tweezers for single cell analysis followed by a brief review of fabricated designs of microrobots. The next section presents the current progress on computer vision techniques for pose estimation in macroscale robotics and as well as in microrobotics followed by a review of manipulation methods on Optical

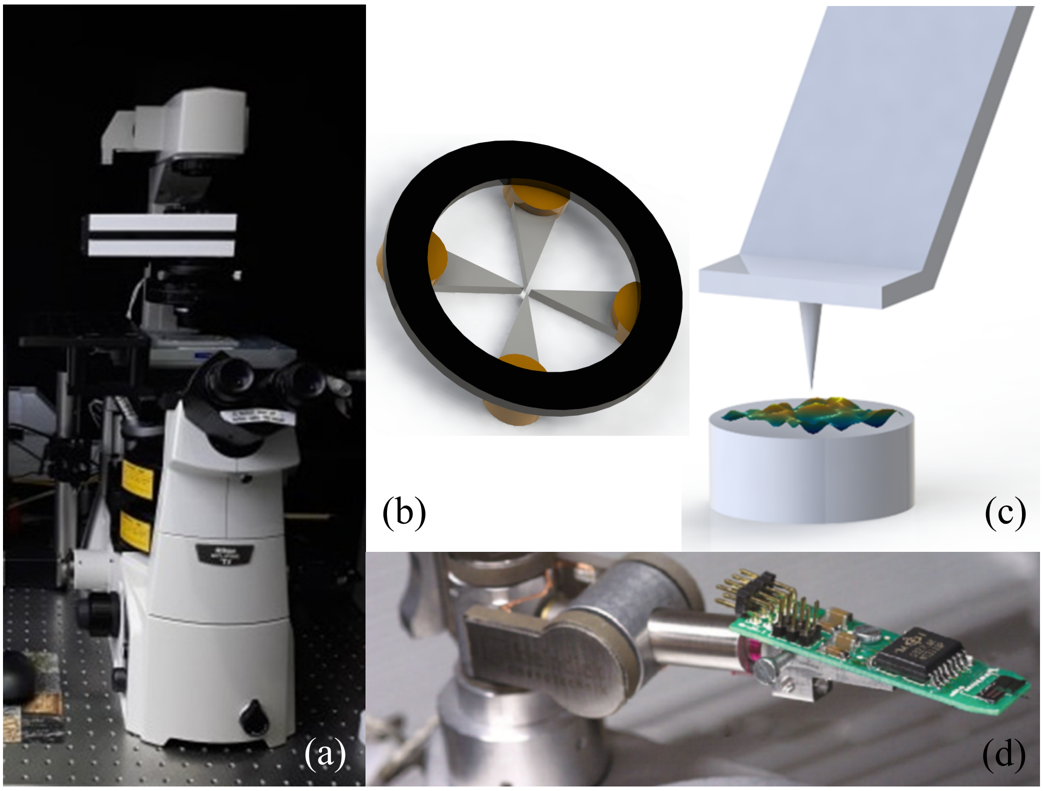

Figure 2.1: Some of the microrobotic systems for cell manipulation. (a) Optical Tweezers (b) Magnetic tweezers (c) Atomic force microscopy probe (c) Mechanical micromanipulator with force sensor on tip ©2007 IEEE [2]

Tweezers and microassembly techniques.

2.2 Applications

Single cell analysis has attracted increased interest in medicine and biological sciences. This subject studies the properties of cells or investigates their growth either of individual or a group of cells. This section of the literature review is focused on the engineering challenges that are present in single cell analysis. The main applications of single cell analysis which are discussed in the next paragraphs are cell manipulation, cell characterization and 3D cell assembly [13].

	Optical Tweezers	Magnetic tweezers	Atomic force microscopy	Mechanical micro manipulators
Spatial Resolution [nm]	0.1-2	5-10	0.5-1	3.5 - 5
Force Range	0.1 - 100 pN	10^{-3}-100 pN	10-10^{-4} pN	1 N (holding force)
Limitations	Photodamage, Sample heating	Force hysteresis	Large, high stiffness probe	Large footprint for enclosed environments

Table 2.1: Overview of micromanipulation systems for cell manipulation

2.2.1 Cell Manipulation

The majority of applications concerns individual cell positioning either in a manual or an automated manner [14]. The advantage of optical non-contact manipulation is that adhesion forces between the micromanipulator and the object are absent, object grasping and release are reversible. Due to the limited force exerted by the laser beam, Optical Tweezers are constrained to the manipulation of small objects which is however sufficient for cell-level manipulation. A detailed description of relevant research on cell manipulation using the Optical Tweezers is presented in Section 2.5.

2.2.2 Cell Characterization

Cell characterization aims to identify the mechanical properties of cells. Properties such as the elasticity and deformation can distinguish healthy from cancerous cells and also reveal information about disease progression [15]. In [16], the stiffness of human red blood cells is investigated by deforming the cell using the Optical Tweezers. Mechanical properties identification is

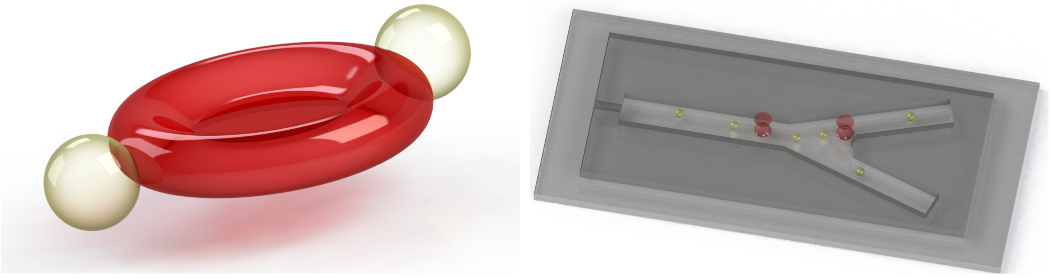
(a) Cell characterization (b) Microfluidic chip

Figure 2.2: (a) A schematic of two microbeads attached to a red blood cell to characterize its mechanical properties (b) A schematic of microfluidic channels using Optical Tweezers for cell sorting

also performed using robotic techniques, such as path planning and image processing, to enhance the manipulation capabilities of the system [17]. The cell is manipulated indirectly by two microbeads acting as handles in order to avoid photo and thermal damage of the red blood cell. A schematic of a similar configuration is shown in Figure 2.2a.

2.2.3 Microfluidic Organs-on-chip

Microfluidic organs-on-chip are a recently emerged paradigm in cell culture. These devices allow control of multiple chambers that contain a single or multiple types of cells in order to simulate cell interactions in living tissue and organs [18]. Microfluidic organs-on-chip are also capable of simulating functions such as perfusion. The aim of such devices is to generate a minimal amount of functioning tissue rather than full organs. Their development arose due to limitations of classic cell cultures which constrain organisation of cells and do not allow the study of specific effects of drugs on cell structures. Prior advances to organs-on-chip are 3D cell structures, such as organoids. Organoids are self-assembled cell microstructures, usually derived from stem cells, which exhibit some of the functionality of target organs [19]. However, in order to simulate organ functionality accurately, it is necessary to recreate tissue-tissue interfaces and cell exposure to mechanical cues, such as fluid shear stress and tension. The lack of vascularisation of this tissue is also limiting their usage. Microfluidic organs-on-chip can address some of these issues. In particular, they can re-enact flows of the vascular system and membranes can be placed inside the microchannels connecting the chambers to simulate the relevant interfaces between cell types. For example, functional lung membrane has provided with models of multi-phase gas exchange *in vitro* [20]. Microfluidic organs-on-chip have been fabricated from various materials such as glass and elastomers, an example of which is polydimethylsiloxane (PDMS). As PDMS is an optically clear material, microfluidic organs-on-chip fabricated from it are suitable for real-time optical imaging of cell interactions with their environment. All the above allow *in vitro* analysis of living cell structures in an isolated functional scenario. Therefore, microfluidic organs-on-chip can allow for real-time study of tissue development, response to targeted drug delivery or 3D cell characterization.

Optical Tweezers are a suitable actuation method for cell or micro-object in enclosed environments, such as microfluidic chips as the optical micromanipulator does not require to be physically placed into the micro-channels (contrary to mechanical micromanipulators). Therefore, Optical Tweezers have the potential to offer new ways to interact with complex organ-on-chip system. Optical Tweezers have been utilized as an actuation method for cell sorting in microfluidic environments [21–23]. During this procedure, cells are directed according to their type in a specific chamber of the microfluidic chip for cell culture purposes. In [24], optical traps are used as a switching mechanism to separate different groups of cells and direct them into the respective chambers. Other work has utilized optical traps as actuators to generate an automated flow path for cell sorting by rotating a pair of microspheres [25]. A system for cell characterization on a microfluidic environment has been also proposed measuring the optical force applied on the cells [26]. A schematic of a microfluidic chip with optical traps used to direct cells is shown in Figure 2.2b.

2.3 Microrobot Fabrication

In order to perform the above tasks, 3D microrobots need to be fabricated. Similarly to other aspects of microrobotics systems, macroscale robot fabrication techniques do not scale down and are not directly transferable to microscale fabrication. In particular, they are not suitable for microrobot fabrication as they rely on techniques and tools, such as mills and laser cutters, which can not be used in the microscale and do not have the required precision and minimum resolution. Alternatively, microrobot fabrication has been relying on micromachining and methods that are relevant to micro-electro-mechanical systems fabrication. Microfabrication methods can be categorized into 2D/2.5D and 3D fabrication methods. A brief description of the main methodologies is given in the following section.

2.3.1 2D/2D.5 Fabrication Methods

Two-dimensional fabrication methods have been well-established and developed due to their applications in the semi-conductor industry for sensor and electric circuit fabrication. These methods are considered 2D as they generate a surface by depositing layers of materials to construct a specific planar geometry. The materials which are used in this process include metals, sil-

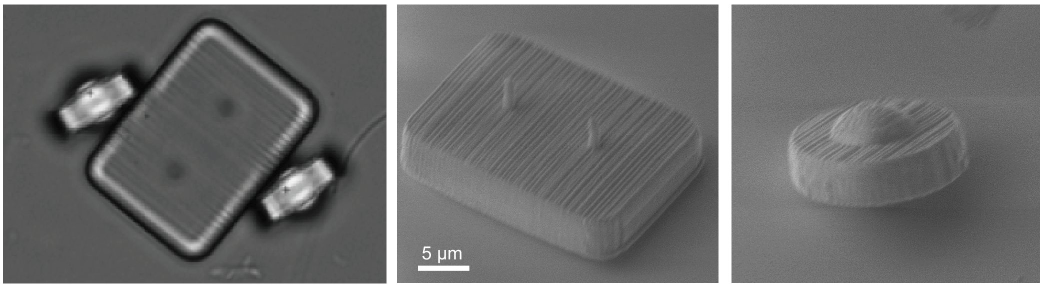

Figure 2.3: 3D-printed microrobots used as grasping mechanisms inside an Optical Tweezers setup ©2016 IEEE [29]

icon and photoresists. For microrobot fabrication, the SU-8 photoresist is a widely used material for the generation of optically transparent planar microgrippers [27]. Alternative, metals such as iron and nickel have been used to fabricate planar magnetic microrobots. Multi-material layer deposition with embedded hydrogels allows to make 3D magnetically actuated microstructures from 2D layers using conventional 2D photolithography [28]. Two-dimensional lithography can be followed by an additional step that allows etching part of the material in order to create some 3D features on the planar geometry. This can be achieved using a focused ion beam or by electrical discharge machining. The combination of 2D lithography with etching is referred to as 2.5D fabrication. However, this method of creating 3D features is of low accuracy and time consuming.

2.3.2 3D Fabrication Methods

Advances in microfabrication technology have led to the development of methods that allow the fabrication of 3D microstructures. This is due to the introduction of the two-photon polymerization technique. This method was initially introduced in 1997 by Maruo *et. al* [30] and is now used by commercially available systems, such as the Nanoscribe 3D-printer. Two-photon polymerization is a process in which a monomer is polymerized under the irradiation of a laser beam. Most common substrates on which the microstructures are printed are glass and silicon wafers. Commercially available photoresists such as Nanoscribe's IP resists, are widely used but also costum-made resists with additional functionality have been developed [31]. Initially, two-photon polymerization was employed for the fabrication of microscale optical elements, such as optical gratings [32]. However, the method's potential to realize 3D arbitrarily-shaped geometries, found immediate application in microrobotics as soon as commercial systems using this technology became available. Two-photon polymerization has allowed the fabrication of 3D arbitrarily shaped microrobots giving the potential of adding more degrees of freedom to the design. As the 3D-printed microstructures are optically transparent, they are suitable for actuation using the Optical Tweezers. Microstructures have been developed to be used as micromachines [33], tools in optical manipulation for manual [29] and automated control [34] potentially for cell manipulation within enclosed environments, such as microfluidic chips.

2.3.3 Functionalization Methods

As mentioned, conventional resists have the property of being optically transparent, however they lack of additional functionality. To this end, functionalization of the material has been proposed. The main motivation for material functionalization for microrobots is for actuation, such as magnetic or light actuation [35], to reduce adhesion forces or to facilitate chemical bonding for microassembly [36]. Metal deposition has been used to coat the polymer surface with metals, such as nickel or titanium, in order to create magnetically actuated untethered microrobots [37]. The deposition layers can include single or multiple materials [38]. Multiple component magnetic microrobots have been also fabricated using this two-step procedure of 3D-printing and metal deposition [39]. Other applications include the fabrication of scaffolds for 3D cell cultures, in which 3D-printed scaffolds are deposited with a metal layer in order to be actuated by the magnetic field [40]. Alternative approaches, modify or embed particles in the photoresist to induce actuation [41, 42]. Metal deposition has also been used in order to use heating of the metal layer for a laser source to induce flows for microobject gripping [43].

2.4 Visual Tracking and 3D Pose Estimation

From the description of microrobot fabrication methods, it can be seen that the created microrobots lack of on-board sensing with regards to their positioning within their workspace. This is one of the main of microrobotic systems, unlike macroscale robot systems, which use encoders to provide position feedback either in the joint space or in the task space. Therefore, closed-loop control strategies, especially in the 3D space, are very limited. Previously proposed closed-loop control methods are implemented for the 2D space. One solution to overcoming this issue is to use the microscope-camera feedback as the main sensor for pose feedback. Hence, estimating microrobot's position and orientation from the microscope-camera feedback could be a means of position sensing for control and improved perception purposes. Previous research has utilized the camera view extensively to calculate the 2D position of microrobots for 2D closed-loop control in various setups, such as scanning electron microscopes, magnetic and Optical Tweezers setups as well as in atomic force microscopy. Therefore, it is of interest to develop methods that can estimate microrobot 3D position and orientation.

In the following, a review of relevant methods for 3D object pose estimation in macroscale systems is presented to serve as a reference of how and if these techniques could be scaled down and adapted in microscale. Then, the current state-of-the-art for depth and orientation estimation in microscale systems is discussed.

2.4.1 Pose Estimation in the Macroscale

Estimating the 3D pose of objects has been investigated extensively in macroscale as it is essential for robotic manipulation and scene understanding. In particular, visual servoing is essential in object localization for robotic grasping [44] and improving localization of robotic arms when the visual feedback is combined with encoder readings. The latter has been important for tool tracking in minimally invasive surgery as the discrepancies from the encoder readings have to be compensated for increased tool precision [45] and for real-time intraoperative simultaneous display of multiple imaging modalities [46].

Pose estimation methods can be categorized as: Feature-based, template-based, neural networks and statistical methods. Feature-based methods can use 2D to 3D known point correspondences for algorithms such as the Perspective-n-Point algorithm [47]. In case of unknown correspondences, algorithms such as the Iterative Closest Point, do not required knowing the exact 2D to 3D point correspondences [48]. Template-based methods assume that the geometrical model of the object is known and rely on generating images of known object poses and matching to the closest appearance [49]. In the recent years, approaches using CNNs arose and are increasingly being used also for pose estimation. Other approaches include combination of feature extraction using CNNs combined with inference models to estimate object pose [50]. Depth and orientation estimation have also been considered as independent problems. A review on depth and orientation estimation methods is presented in the following section in order to assess how these methods could be potentially applicable in microrobotic setups.

2.4.1.1 Depth Estimation

Classic reconstruction methods make use of multi-view epipolar geometry in order to recover depth information in stereo reconstruction algorithms [51]. Such methods require views from multiple cameras and also rely on accurate camera calibration. Other methods use defocus information, referred to as depth from focus (or defocus) methods [52]. In particular, the focus information from two images with different levels of focus can be used to estimate the 3D position of an object [53]. Similar methods have been used for removing blurriness due to camera motion [54] and also for automatic focusing on microscopes [55]. These methods are applicable to single view images. Recent approaches utilize supervised learning using labelled single images. In particular, supervised learning uses a dataset of monocular images their corresponding depth maps as labels, which can be acquired using depth cameras [56]. Other depth estimation are used for scene reconstruction from a moving camera using convex optimization [57] or by combining information of multiple CNNs using Conditional Random Fields [58] and Point Spread Function Convolutional Layers [59].

2.4.1.2 Orientation Estimation

Estimating object orientation has been investigated also as an independent problem to depth estimation. Traditional methods include using state estimation approaches such as using Extended Kalman Filtering with angular position measurements from robot sensors [60]. Template matching has also been considered for object orientation estimation [61]. More recently, neural networks have been employed for orientation estimation. In particular, a method of estimating the relative orientation between two camera poses has been proposed in [62]. Other methods attempt to incorporate learning of a Riemmanian manifold in order to obtain more accurate orientation space estimations using CNNs [63].

2.4.2 Pose Estimation in the Microscale

In the following, a presentation of the current state-of-the-art for microrobot position and orientation estimation is given.

2.4.2.1 Depth Estimation

In microrobotic systems, proposed methods are dependent on the respective system setup. Model-based approaches, using the microrobot's geometrical design for reference, estimate the microstructure's pose for assistance in microassembly [64, 65]. Shape estimation for haptic feedback has also been considered in [66]. A model-based optimization solution is proposed in [67] for intraocular microrobot localization. In [68], the velocity of helical microswimmers along the microscope z-axis is estimated for surface reconstruction using prior calibration of the microrobot's velocity along the z-axis. Depth recovery has been investigated for setups inside a scanning electron microscope [69]. Cui *et al.* [70] have proposed a method for estimating the 3D position and the rotation on the x-y plane. In [71], estimation of multiple depths for objects in different heights within the scene is performed using the sharpness measurements locally in the image. Other applications include depth recovery of microgrippers and carbon nanotubes for automation purposes using variance-based sharpness calculations [72] and micropipette depth tracking using particle filters for 3D reconstruction of microstructure geometries [73].

2.4.2.2 Orientation Estimation

Orientation estimation in microscale systems has been investigated by Kudryavtsev *et. al* for experimental setups inside scanning electron microscopes proposing a geometrical solution to estimate orientation [74].

2.4.2.3 Pose Estimation Challenges in the Microscale Compared to the Macroscale

As seen from the overview of the work presented in the previous section, feature-based stereo methods rely on the perspective camera projection model to get the 3D position of a point from triangulation using different camera views. This approach is not applicable in the microscale for two reasons: i) the camera projection model is orthogonal and therefore depth information is not observable and ii) most microrobot setups have only one camera view. For these reasons and as most microrobot manipulation platforms have a mounted microscope-camera system for observation, depth from focus methods and Neural Networks approaches are more suitable for pose estimation in the microscale. Neural networks require a ground truth labelled dataset so they are not applicable to all setup. However, for an Optical Tweezers system with 3D-printed microrobots, a ground truth dataset can be generated for training and validation. To this end, the proposed methods in this thesis use a depth from focus and a CNN approach.

2.5 Manipulation and Control

The applications presented in the previous sections illustrate that precise 3D manipulation is required. Manual control is challenging due to the scaling effect in the microscale, the small number of DoF and lack of 3D position feedback. To this end, automation of tasks and shared control schemes could potentially improve accuracy and precision in cell manipulation. A number of control and visual servoing techniques have been proposed for magnetic and mechanical microrobots, Optical Tweezers and atomic force microscopy probes [75]. As the focus in this thesis is Optical Tweezers actuation, an introduction on their operation principle and control strategies is presented in this section followed by a review on automation and manual techniques as well as haptic feedback frameworks for cell manipulation using Optical Tweezers.

2.5.1 Optical Tweezers

Optical Tweezers were firstly introduced by Arthur Ashkin in 1970 [76]. In 2018, he was awarded the Nobel Prize in Physics for introducing Optical Tweezers and for their applications in biology, together with Gérard Mourou and Donna Strickland who contributed further on the technology. Optical Tweezers are a tightly focused laser beam which can attract objects with sizes from a few nanometres up to a few tens of micrometers towards the focus of the laser beam. Microobjects are attracted towards the focus when gradient forces are dominant, while radiation pressure attracts it towards the direction of the optical axis of the beam (Figure 2.4). There are several models that describe the force field generated by the laser beam of the Optical Tweezers. The accuracy of the model depends on the size of the trapped

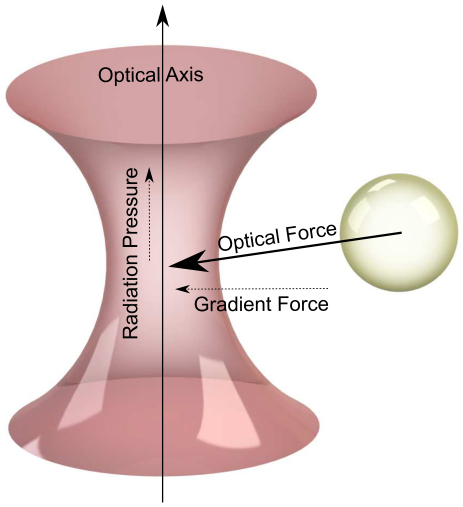

Figure 2.4: A schematic of Optical Tweezers laser beam with a spherical object attracted towards the focus of the laser

particle with respect to the wavelength of the laser beam of the Optical Tweezers. If the size of the trapped object is much larger than the wavelength of the laser beam, then the ray-optics model [77] describes the exerted forces accurately. Otherwise, if the trapped object is much smaller than the wavelength of the beam, then Maxwell's electromagnetic equations describe the Optical Tweezers force model. Closed-form analytical solutions can only be obtained for very few geometries, such as spherical [78] and cylindrical particles [79]. In other cases, the force field of non-spherical micro-structures has been investigated using T-matrix calculations [80] or can be calculated through numerical methods and computational models [81].

2.5.2 Optical Manipulation

The focus of the review on control strategies is on automation techniques for non-contact manipulation of a single or multiple groups of cells using the Optical Tweezers. The two main manipulation techniques that are developed in the literature are direct and indirect object manipulation. Direct manipulation refers to immediate trapping of the manipulated object by the laser beam. Indirect manipulation uses an intermediate optically trapped microstructure to manipulate the desired microbject.

2.5.2.1 Direct Manipulation

A number of frameworks have been proposed for automated cell transportation within a fluid medium by directly trapping the microparticle. The objective of achieving precise micromanipulation can be decomposed in the following issues that have to be tackled: i) The object needs initially to be stably trapped by the laser beam. ii) Following this, its position and orientation must be regulated in the 3D space taking into account the dynamics of the object moving within the fluid medium. iii) It is also essential that the object is transported along an obstacle-free path while the object is maintained within the trapping radius of the laser beam. Some of the traditional robotic techniques can be employed to some of the previously mentioned problems. The proposed frameworks are implemented on conventional or Holographic Optical Tweezers.

Classical control methods such as a proportional-derivative controller can be used to regulate the microparticle position on the 2D image plane [82]. A simplified and commonly used mathematical description of the system dynamics assumes spherical objects and the optical trapping is described by the ray-optics regime [83]. The model is a function of the viscous drag coefficient and the trapping stiffness of the optical trap which are dependent on the respective experimental setup. For systems described by the spring force dynamic model, adaptive control techniques can be employed requiring no prior system calibration [84]. Using this control technique, position regulation on the 2D plane can be achieve while the parameter estimator converges to the actual values of the coefficients of viscous drag and trapping stiffness when starting from an initial estimate. Adaptive control is also applied in order to estimate the acceleration and velocity of the particle [85,86]. Three-dimensional positioning and rotation presents additional challenges due to the number of DoFs of the Optical Tweezers systems, the lack of position feedback and the unknown trapping force behaviour for non-spherical structures. In the relevant research, control methods for 3-DoF rotation of spherical objects have been reported on Holographic Optical Tweezers which have more DoF than the conventional Optical Tweezers as they allow splitting of the laser beam on multiple planes [87].

The ray-opitcs model in the previously mentioned work is relatively accurate for microobjects with dimensions more than 10 μm. However, for smaller objects the random perturbations due to Brownian motion are more evident and have a noticeable effect on trapping and transportation. Therefore, the spring force model can be extended by considering the random perturbation of the microobject due to Brownian motion as a stochastic model. Kalman filtering has been used in order to estimate the tracked particles position [88]. An analytical expression connecting the trapping probability and the maximum micro-object velocity is formally derived in [89] and is taken into consideration in the nonlinear controller design.

Path planning techniques are also employed to assist cell transportation. To take into account the dynamic changes of the environment, the random motion of the obstacles can be described using stochastic modelling. In particular, in [90] a partially observable Markov process is used to model the random motion. An alternative approach uses a constraint based switching controller that achieve simultaneously obstacle avoidance and consistent object trapping during transportation based on geometrical modelling of each scenario [91]. Traditional robotics approaches are also employed for obstacle avoidance such as the A-star algorithm for path planning [92].

2.5.2.2 Indirect Manipulation

Despite the advantages of non-contact manipulation, optical trapping can cause damage to the cells due to the induced laser power [11]. Therefore, it is important to minimize cell exposure to the laser beam. To this end, methods for indirectly manipulating cells have been developed. Arai *et al.* have proposed a methodology for Holographic Optical Tweezers to translate and rotate a spherical object using two spherical beads in 3D [93]. Holographic Optical Tweezers have been also used to manipulate lipid nanotubes using optically trapped microspheres that adhere on the tube [94]. Another approach suggests non-spherical microtools fabricated using SU-8 for improved dexterity in manual 2D cell manipulation [95].Stable grasping configurations for object manipulation can also be generated by synthesizing 3D gripping formations using multiple spherical microbeads [96]. The problem is formulated as a constrained optimization problem that has to satisfy the 3D form closure properties for stable grasping. Alternatively, the gripping configuration of the microbeads can be formed as a region-control problem [97]. Other proposed control strategies use the concept of indirectly pushing the microobject using microbeads rather than caging in order to further reduce laser irradiation [98].

2.5.2.3 Multiple Object Manipulation

The problem of manipulating multiple objects using Optical Tweezers can also be considered as a swarm, multi-agent robotic system due to multiple optical trap generation [99]. This approach is effective when multiple cells have to be transferred in a specified formation. Chen *et al.* proposed a potential-field based controller in order to move the microparticles automatically to a desired position while preserving a fixed optical trap configuration [100]. A swarm-inspired technique is employed in [101] to assist simultaneous position control of a group of microobjects. Multiple groups of objects are manipulated by controlling both the laser source locally and the piezo stage for transportation outside of the image field of view in [102].

2.5.2.4 Haptic Feedback and Shared Control

Force feedback can further facilitate micromanipulation by conveying micoscale force interactions to the operator and help the user overcome unfamiliar microscale force dynamics. This gives rise to two different approaches that integrating haptic feedback and haptic guidance into the control framework.

Haptic feedback aims at measuring the force interactions in the microworld, either through vision feedback or force sensing depending on the setup, and then render them to the user. One of the first systems coupling the macro and microscale force interactions in Optical Tweezers was developed by Arai *et al.* [103]. Similar frameworks have been presented for atomic force microscopy systems [104, 105]. Avoiding instabilities and ensuring a real-time control cycle are the two main issues that have to be addressed when force measurement is performed. In the case of Optical Tweezers, the exerted forces on the microobjects are measured visually through image processing techniques which also require prior parameter calibration [106]. An alternative event-based image processing technique to the frame-based approach is proposed in [107] to minimize image processing delays and ensure smooth force rendering to the operator. Haptic feedback on atomic force microscopy systems has also been exploited as a sensing means for microstructure shape reconstruction [66].

Haptic guidance is based on virtual force which aim to assist the operator in completing a specific task. This concept is known as Active Constraints/Virtual Fixtures [108]. Despite the fact that automation can be a solution for task completion, it excludes the operator from the control loop. Therefore, it is desirable to combine the machine intelligence and the human input in the control system. A potential field approach on Optical Tweezers was developed in [109] in order to guide the operator during object transportation while limiting the user dynamics by compensating the drag force. A similar framework has been presented in [110] on an atomic force microscopy system using haptic guidance along an optimized obstacle-free path during single object transportation. Compared to the actual force rendering systems, virtual guidance frameworks present increased stability due to the absence of high gains which are necessary for coupling between the micro and macro world [111].

In this thesis, one of the research objectives is to develop a shared control interface for multiple microrobot and 3D microrobot manipulation integrating haptic guidance and also human sensory information that facilitates multiple microrobot manipulation.

2.5.3 Microassembly

One of the aims of developing accurate micromanipulation strategies is to use microrobots as a means to perform assembly in the microscale. A motivation for this is the assembly of devices when fabrication techniques cannot produce specific devices. Moreover, it can facilitate *in situ* assembly when direct delivery of microrobots to specific areas is challenging. These devices could then be used for cell manipulation. Microassembly can be performed by an operator with some parts of the tasks performed automatically or it can take place spontaneously, in the case of self-assembly.

2.5.3.1 Robotic Microassembly

One method of assembly is by using a robotic micromanipulation system. In [112], 3D magnetically driven intraocular microrobots are assembled from planar nickel-coated components which are bonded with ultraviolet-cured glue. Different types of microgrippers have been proposed in order to facilitate assembly. These can employ either a passive or active form of actuation. Passive and compliant microgrippers have been proposed for micromanipulation [3] and microassembly [113]. Active forms of actuation include piezo and shape memory alloy grippers. In [114], a microassembly platform is proposed consisting of a two-fingered piezo gripper with a silicon end-effector that is capable of handling objects with sizes of a few tens of microns. The goal of this platform is to assemble micro-components that can be used in larger component assemblies. Shape memory alloy microgrippers have also been proposed for microcomponent assembly and for assembling scaffold for tissue engineering [115]. Alternative methods of gripping include strategies such as using optically controlled microbubbles for microassembly [116].

The accuracy and precision of assembly can be improved by automating parts of the assembly procedure. A closed-loop approach using model-based visual position feeback for micro-electro-mechanical systems microassembly is presented in [117]. Sensing of the position of piezo actuated cantilevers used for microassembly is considered in [118], which is then used in closed-loop control. More than one microrobots can be used in control strategies, such as caging, in which the grasped micro-object is surrounded by the microrobots that are considered as multiple end-effectors [119]. Other approaches include shared-control user interfaces to assist microassembly [120].

2.5.3.2 Self-assembly and Reconfigurable Microassembly

As can been seen from the processes described for robotic microassembly, most of the techniques are manual. However, manual assembly is time consuming and therefore not suitable for batch microassembly. Moreover, it requires dexterity and precision and the operator must take into account microscale dynamics. To this end, more versatile techniques emerged such as self-assembly and reconfigurable microassembly. Self-assembly refers to assembling components into larger 3D microstructures using dominant microscale forces or external force fields. External assembly mechanisms include magnetic or electrostatic actuation [121]. For any of the proposed techniques, although they allow self-assembly from multiple components, they do not allow disassembly due to the bonding methods used which are not reversible as in [121]. Reconfigurable microassembly facilitates component restructuring to create different geometrical patterns in order to adapt the functionality of the robot to multiple tasks. For example, reconfigurable systems in the millimeter scale have been proposed consisting of up to 20 individual components that can be reconfigured for rolling and climbing [122]. Diller *et. al* use external magnetic fields and electrostatic forces as the assembly force and anchoring mechanism respectively [123]. In particular, the magnetic attractive force is generating by an external field to create attraction between rectangular components that have an embedded permanent magnet in their core surrounded by an insulating material to reduce the magnetic force between the components allowing reconfiguration. The individual components used in the presented techniques are sized at around 500 μm.

Optical Tweezers have also been used as a microassembly platform. Components can be self-assembled and bound together using biomolecules which are coated on the top of the structures [36,94] or they can be assembled using the laser beam for *in situ* polymerization [124]. However, this method makes assembly permanent and not reconfigurable. Reconfigurable microassebly has been proposed to assemble scaffolds for tissue engineering inside an Optical Tweezers setup [125]. The components, with sizes from 5 to 10 μm, are 3D-printed using two-photon polymerization and assembled using the Optical Tweezers and they can be reconfigured as the components are complementary to each other and can be manually disassembled.

In this thesis, reconfigurable microassembly is investigated using a combination of optical and magnetic actuation to assembly microcomponents into larger assemblies.

Chapter 3

Microrobot Fabrication

This chapter presents the fabrication procedure of optical and hybrid optical and magnetic microrobots used for indirect microobject manipulation and for reconfigurable microassembly. One of the issues investigated is how more degrees-of-freedom can be incorporated into the fabricated microrobots. This can be addressed either by 3D-printing the microstructure in a single step or by assembly individual components to create an optically transparent articulated microrobot. Both approaches are investigated. In addition, it is desirable to use a combination of the Optical Tweezers and the magnetic field for micromanipulation and microassembly. This chapter describes how 3D optically driven microrobots are fabricated using the two-photon polymerization technique. A characterization of the effect of the printing power is presented to investigate the impact of the printing power in the feature resolution of the printed structures. The fabrication procedure of microrobots which are actuated both by the Optical Tweezers and the magnetic field is also presented by selectively coating parts of the 3D-printed microstructures

---

Contents from this chapter have been published in: **Laser-Printing and 3D Optical-Control of Untethered Microrobots**, E. Avci, M. Grammatikopoulou, and G-Z. Yang., Advanced Optical Materials, 2017

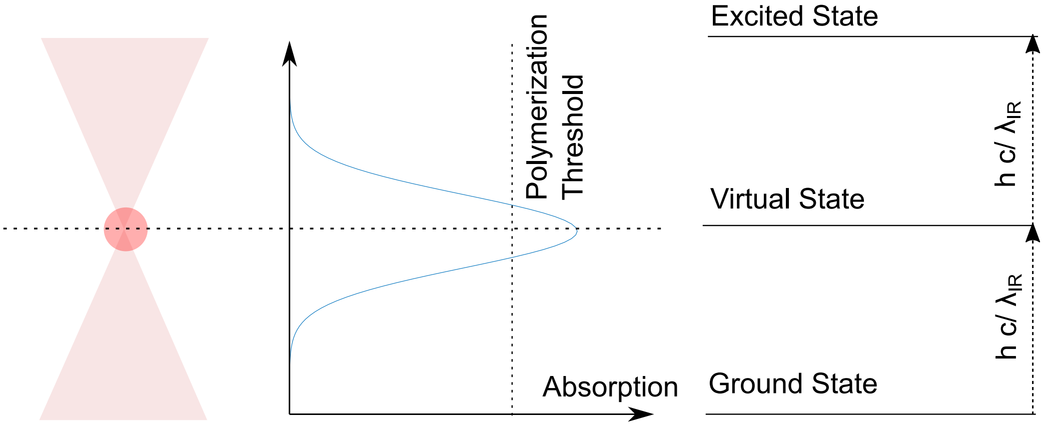

Figure 3.1: Two-photon polymerization principle

with a nickel layer.

3.1 Two-photon Polymerization

Two-photon polymerization technology is based on two-photon absorption, where an atom absorbs two photons in order to move to a higher energy state (Figure 3.1). This excitation leads to resist polymerization at the focus of the laser. This method of polymerization came to improve the spatial resolution of one-photon absorption for polymerization where the absorption of a single photon of higher energy is needed for the transition to a higher energy state. Two-photon absorption can be achieved by near-infrared femtosecond lasers in contrast to one-photon absorption which is achieved by visible ultraviolet light. The spatial resolution that is achieved in two-photon polymerization is approximately 100 nm. Commercially available systems use two-photon polymerization for 3D-printing microstructures, such as Nanoscribe, which is also the system that has been used in this research.

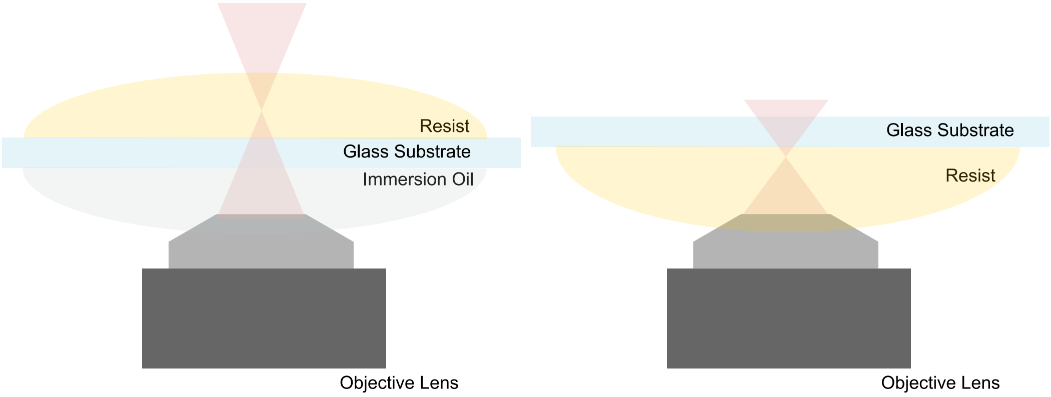

(a) Upwards (Conventional) (b) Downwards (Dip-In)

Figure 3.2: Printing configurations

3.2 Optical Microrobot Fabrication

Taking advantage of the capabilities of two-photon polymerization in microfabrication, any computer-generated geometrical design can be realized for microrobot design. As the actuation system that is used is the Optical Tweezers, it is required that optically transparent objects are fabricated. Commercially available photoresists have properties that allow optical trapping and are the ones that were used for the fabrication of the microrobots presented in this thesis. The resists which were used are the negative tone IP-L 780 and IP-Dip Nanoscribe photoresists. IP-L is used to achieve the highest resolution that Nanoscribe is capable of and is of low viscosity. IP-Dip is of higher viscosity than IP-L and is used for Dip-In Lithography. The characteristics of each resist are shown in Table 3.1. Each resist is designed to be used with a specific printing configuration as shown in Figure 3.2. The conventional upwards configuration (Figure 3.2a) is suitable for printing small-sized structures with IP-L 780 for designs that do not require material support. This is because the IP-L 780 resist has very low viscosity and is not able to provide support to the microstructure and, therefore,

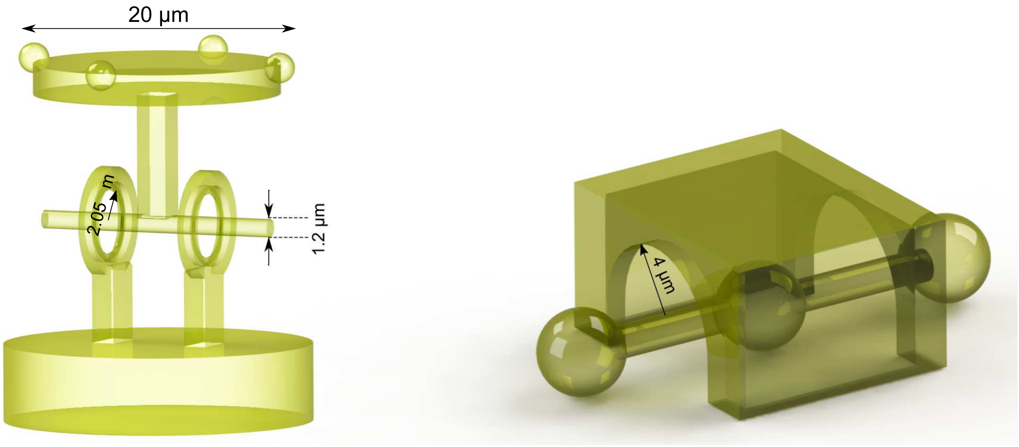

Figure 3.3: Rendering of the geometrical model of the two-component rotational joint (left) and of the cylindrical microstructure with cover (right)

Photoresist	IP-L 780	IP-Dip
Refractive index	1.48	1.52
Developer	PGMEA/IPA	PGMEA/IPA
Exposure	780 nm	780 nm

Table 3.1: Nanoscribe's IP photoresist characteristics

can result to parts of the microstructure collapsing. In addition, the laser is irradiating through polymerized parts of the structure which can affect the spatial resolution of the features of the microstructure. On the other hand, IP-Dip is used the Dip-In configuration in which case the printing direction is downwards. Therefore, printing through the polymerized part of the resist is avoided. In addition, as IP-Dip is more viscous than IP-L, it can provide material support for example in the case of microstructures with hollow parts.

For the Nanoscribe 3D-printer, the detection of the interface between the glass slide and IP-L can be realized automatically. This is particularly useful for batch printing of microstructure arrays as the interface is found for every new microstructure. This is important as each microstructure starts to be printed at the same distance from glass slide surface. On the contrary, this cannot be realized automatically for IP-Dip on glass substrate and has to be performed automatically. In the case of IP-Dip, the resist should be placed on indium tin oxide glasses for automatic interface detection by the software. However, indium tin oxide glass slides are thicker than the conventional glass slides which makes them unsuitable to be imaged in an Optical Tweezers setup as the Optical Tweezers objective lens has a very small field of view and makes it impossible to focus through a thick glass slide. Alternatively, some sacrificial height needs to be added on the microstructure on the design step so that the part of interest of the microstructure is always printed above the glass surface.

One of the main advantages of the described system is that they are capable of batch fabrication. Therefore, every design that is investigated is printed in large arrays that makes testing and characterization easier. This makes it possible to assess the repeatability of the fabrication of each design. It also very importantly provides a method of having redundancy in the number of available microstructures for testing in case some of them are damaged or lost.

3.2.1 Microrobot Design Considerations

As the two-photon polymerization technology has the potential of fabricating 3D microrobots with suitable refractive index for optical manipulation, the next consideration is how to incorporate multiple degrees-of-freedom in the design. It is also significant to ensure the mobility of the microstructure which can be hindered by adhesion forces. This is particularly challenging as one of the characteristics of Nanoscribe photoresist is that they are de-

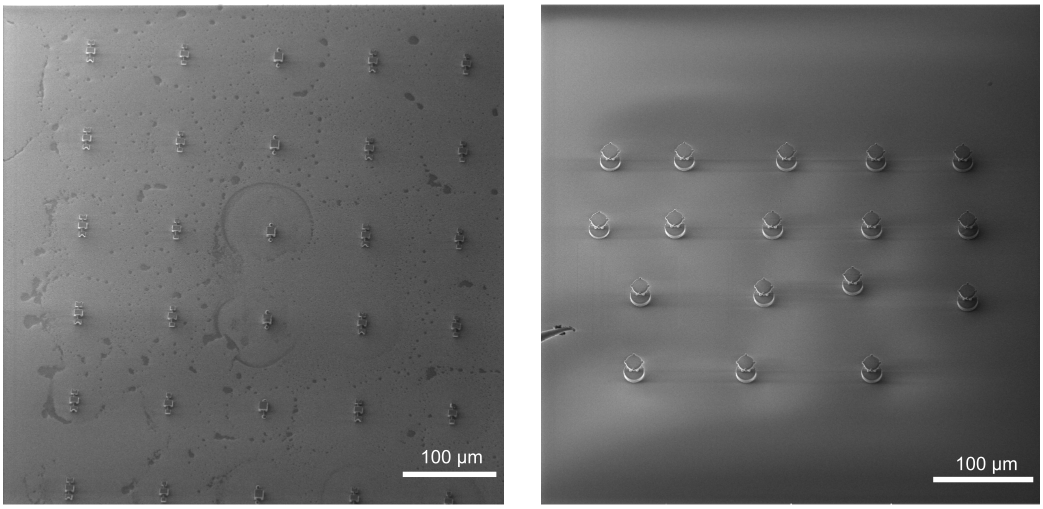

Figure 3.4: Batch fabrication of microstructures. Array of cylindrical microrobots with rectangular covers (left) and an array of rotational joint microrobots (right)

signed so that the material adheres strongly on glass. There are several approaches in fabricating 3D microrobots which can achieve non-planar motion. One approach is to fabricate the individual components that comprise this mechanism and then assemble them mechanically, usually manually, using mechanical micromanipulators. This approach require a method of attaching the components to each other, usually through chemical bonding [36]. Moreover, manual assembly requires dexterous and high precision manipulation and is time consuming, and almost impossible, for batch fabrication and assembly of mechanisms. In the following, two methods are investigated: i) printing of a microstucture with multiple components as a single structure and ii) combining optical and magnetic actuation to assemble a kinematic chain. Before explaining how hybrid optical and magnetic microrobots are fabricated, it is described how the printing laser power affects the resolution of the features the fabricated microstructures and how optical microrobots are fabricated.

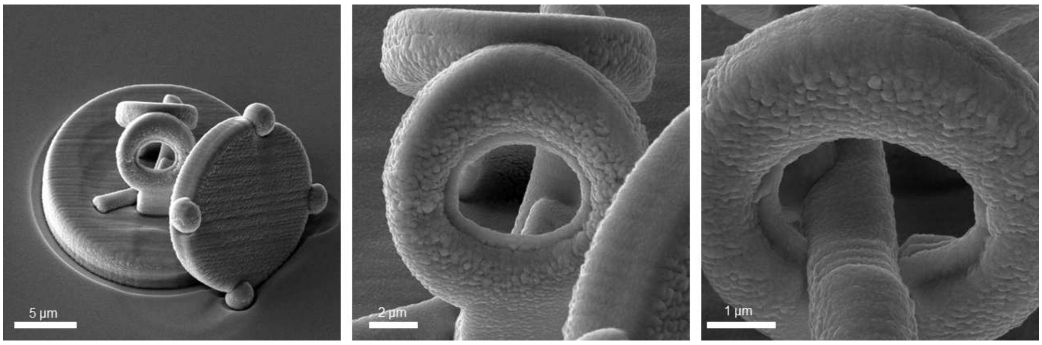

(a) 20 %

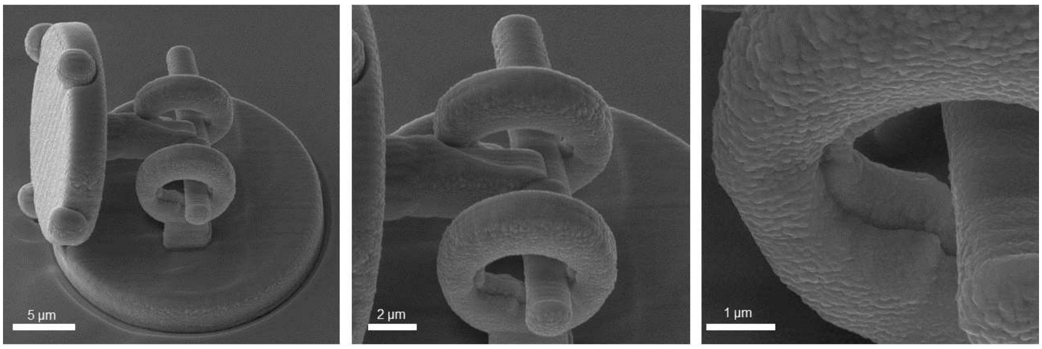

(b) 25%

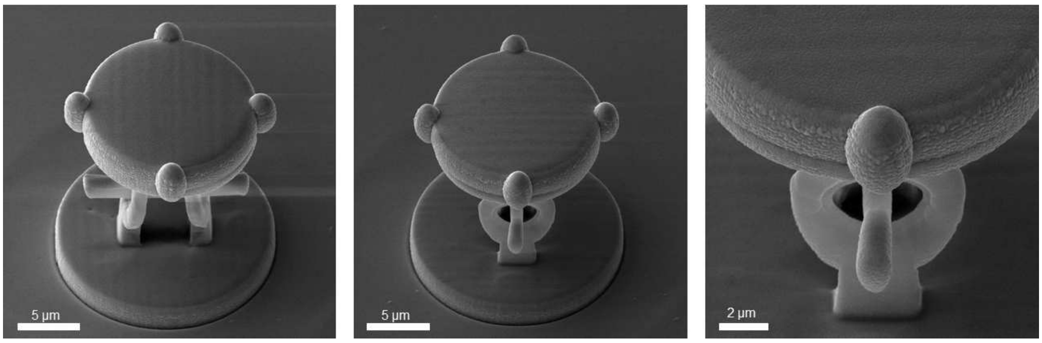

(c) 30%

Figure 3.5: Effect of printing power on feature resolution (20 %- 30%)

3.2.2 Printing Power Effect on Feature Resolution

An array of microstructures is printed with different printing powers to assess its effect on the microstructures (Figure 3.4). The array was printed using the IP-Dip resist in the Dip-in configuration. The printing power effect is investigated on the design of a multiple component rotational joint for out-

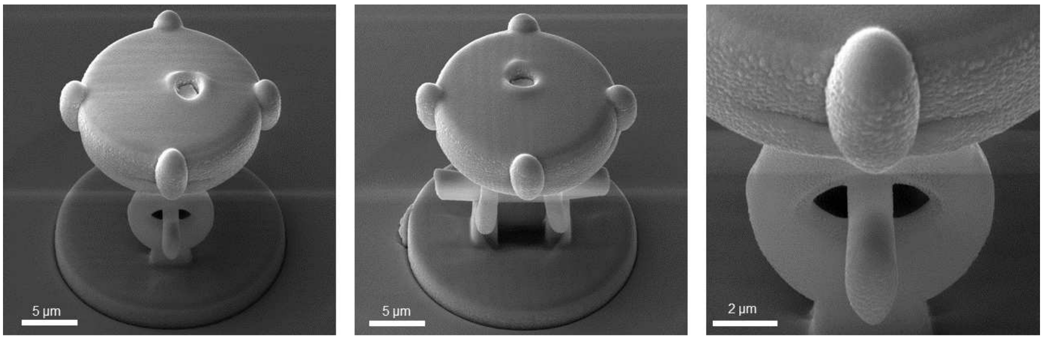

(a) 50%

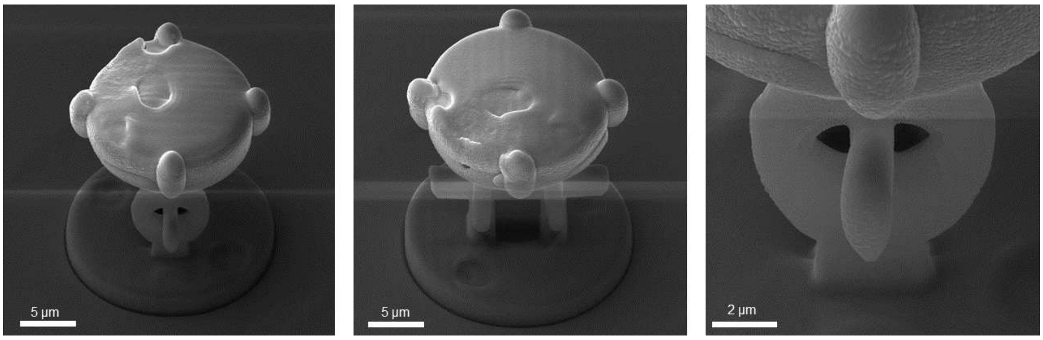

(b) 55%

Figure 3.6: Effect of printing power on feature resolution (50 %- 55%)

of-plane rotation. A rendering of the Computer-aided design (CAD) model is shown in Figure 3.3. The features of interest are the gaps that appear in the designs, as indicated by the dimensions of Figure 3.3. The distance between the components is essential as it also affects the contact area between them. This consequently affects adhesion between the components which is a determining factor of the mobility of the microrobot. In order to observe the microstructures in higher detail, the array of the rotational joint structure was coated by a layer of silver using thermal evaporation deposition.

An array of the rotational joint microrobot was printed with different laser powers. The power is referred by the scaling factor of the maximum power that the laser is capable of. The range of power scaling which is used is between 20 % to 55 %. From Figure 3.5a, it can be seen that for low laser powers, in this case up to 20 %, the material presents low stiffness and is more flexible. However, the rotating part of the microstructure cannot be supported by the base of the joint and the top part is collapsing. Figure 3.5b shows that for a 5 % increase, higher polymer stiffness can be achieved with satisfactory feature resolution (Figure 3.5b-middle and right). It is also worth noting that as the rotating part is collapsed on the base but is also supported by it, the rotating component has not been printed merged with the base of the joint. In contrast, it is observed that for a further 5% increase of the laser power, the features of the rotating part and the base of the joint start to merge and, therefore, the rotating part is printed on an upright position (Figure 3.5c). For power scalings larger than 50%, the laser is also overheating the resist causing bubbling (Figure 3.6). It can also been seen from Figures 3.5c (right) and 3.5a and b (right) that the higher the laser power, the lower the feature resolution is.

It is worth noting that the minimum resolution that can be achieved also depends on the expiration date of the resist. It has been experimentally observed that the older the resist, the lower power is needed to polymerize it. Hence, the feature resolution degrades over time for older resists. However, the overall trend of the impact of laser power on printing resolution can be generalized with slight adjustments on the power scaling parameter depending on the system, the laser calibration and the resist.

3.3 Hybrid Optical and Magnetic Microrobot Fabrication

The above procedure is for the fabrication of polymer components which can be manipulated by the Optical Tweezers due to the transparency and the

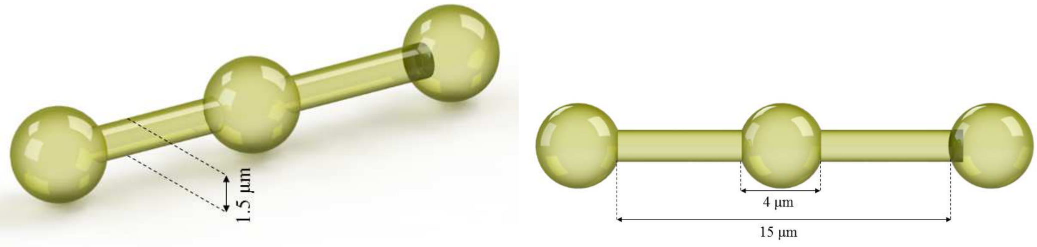

(a) 3D view (b) Top view

Figure 3.7: Rendering of the geometrical model of the cylindrical microrobot with spherical handle and spherical tips

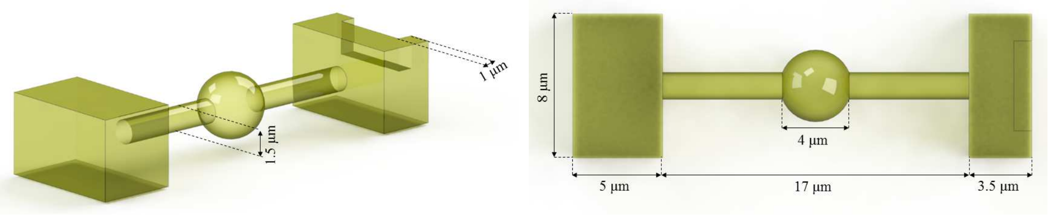

(a) 3D view (b) Top view

Figure 3.8: Rendering of the geometrical model of the cylindrical microrobot with one spherical handles and rectangular tips

refractive index of the resist. In order to create microstructures that are also responsive to the magnetic field, the surface needs to be coated with a magnetic material. However, it is also important that optical trapping can be simultaneously achieved. The motivation for creating hybrid actuated microstructures is so that the individual components are assembled using the magnetic force and actuated by the optical force as described in Chapter 6. The fabrication procedure to achieve selective metal deposition for hybrid optical and magnetic actuation is described in the following section.

3.3.1 Masking for Selective Metal Deposition

In order to fabricate microrobots which can be actuated both by the Optical Tweezers and the magnetic field, the polymer surface needs to be deposited with a ferromagnetic material selectively in specific areas. The aim is to allow optical trapping of a spherical handle in the middle of the cylinder, while the remaining part of the cylinder and its tips can be magnetized. The motivation is that other microstructures, that can also be magnetized, are attracted to it in order to form an assembled kinematic chain. Therefore, only specific areas of the microstructure have to be deposited with metal while the spherical handle remains optically transparent. To achieve this, a mask is printed above selected areas of the structure which is used to cover the surfaces that need to be grasped by the laser. A similar approach for selective metal deposition has been used in [43]. The virtual geometrical model of the microstructures with the corresponding masks and dimensions are shown in Figure 3.9. A 3D-printed pair of microstructures is also shown in Figure 3.10. After printing, the array of microstructures are deposited with a 100 nm layer of nickel using the sputtering method. The masks are removed after the metal deposition during the detachment procedure of the microstructures from the glass substrate.

3.4 Microrobot Detachment

After fabrication, the microstructures need to be removed from the glass and transported to the workspace of interest, which in this work is a closed space filled with a liquid medium such as deinonized water. The microstructures can be removed from the glass slide individually using micromanipulators or by sonication, which is a batch detachment method.

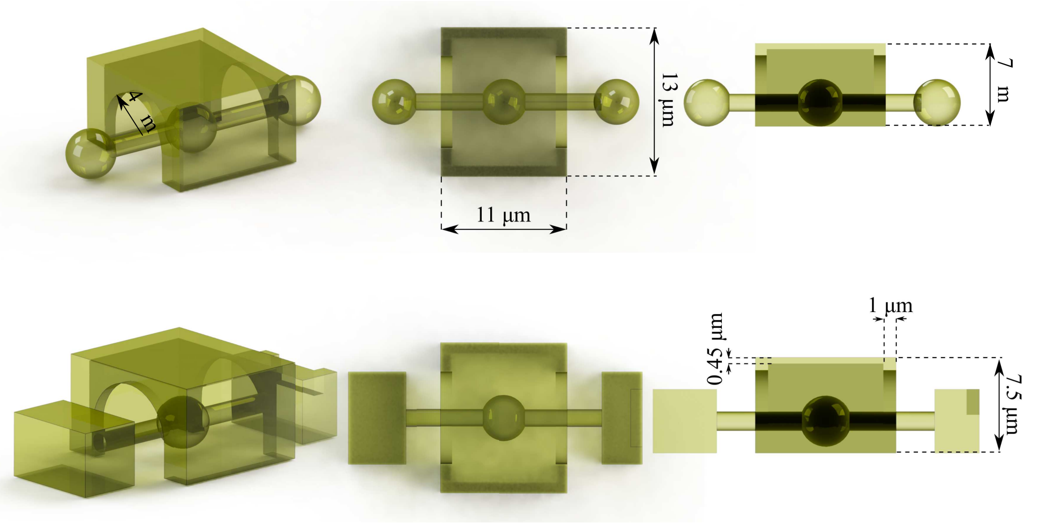

Figure 3.9: Rendering of the geometrical model of the microstructures with masks for metal deposition

The detachment procedure using mechanical micromanipulators is the following: The glass slide, on which the microstructures are printed, is placed inside the SEM (Tescan, Czech Republic). The chamber contains a set of up to four micromanipulators (MM3A, Kleindiek Nanotechnik, Germany). Each microstructure is detached individually. The advantage of this approach is that mechanical micromanipulators render relatively large forces, therefore they can overcome the adhesion between the base of the microstructure and the glass substrate. However, this method has a low success rate as the detached microstructure falls again on the substrate and hence can adhere o the glass substrate. It is also time consuming for detachment of large batches of microstructures. An alternative method of microrobot detachment is sonication. This methods relies on applying ultrasonic sound waves on particles to induce motion. The advantage of this method is that it is suitable for batch microrobot detachment, however the detached microrobots need to be retrieved and transferred to the workspace of interest. The retrieval step be-

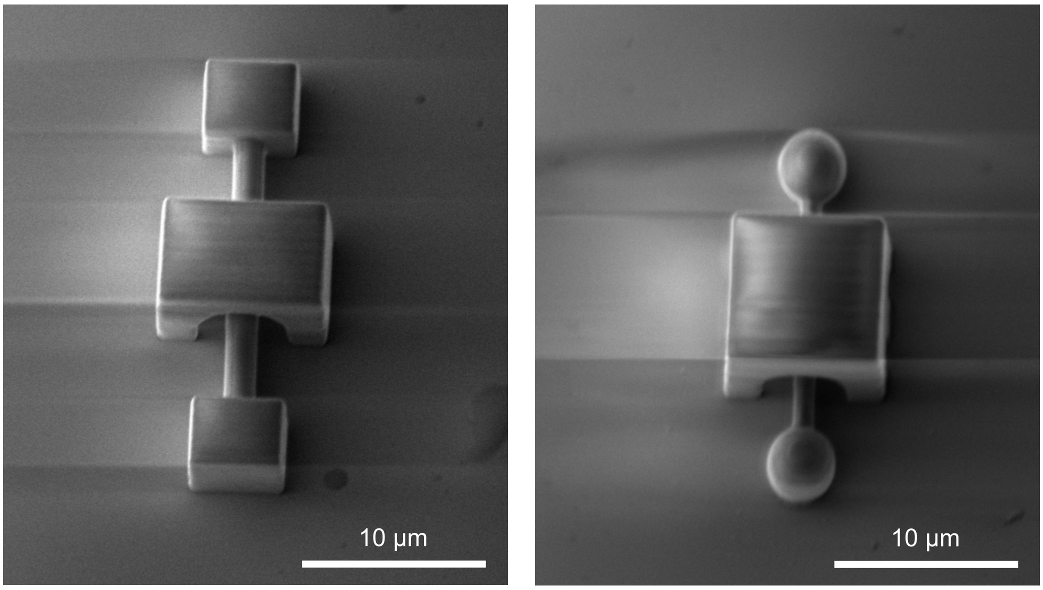

Figure 3.10: Cylindrical microrobots with rectangular (left) and spherical (right) tips with covers on top of spherical handle

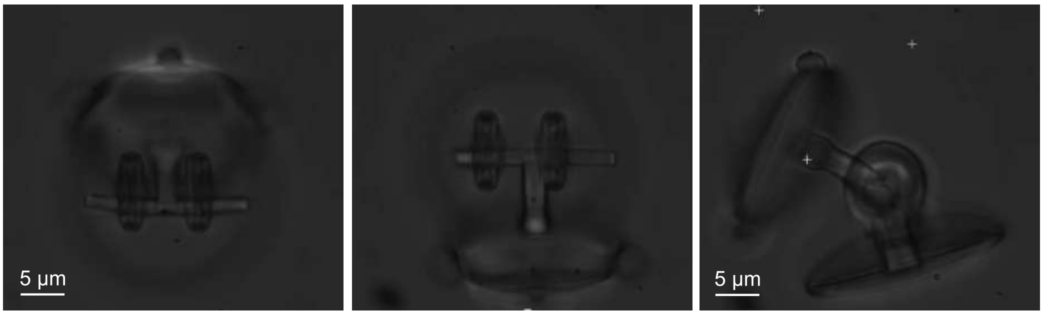

(a)

(b)

Figure 3.11: Partially detached microrobot (only rotating part) (a) and fully detached microrobot (b) using sonication

comes less challenging if the microrobots are confined in a small workspace and detached directly in it. Therefore, the sample with the 3D-printed microrobot is directly placed inside the sonication bath and is later placed inside the Optical Tweezers, enclosing all detached microrobots in a defined and relatively small workspace. The duration of sonication is usually between 5 to 10 seconds. The detached microrobots are suspended within the liquid

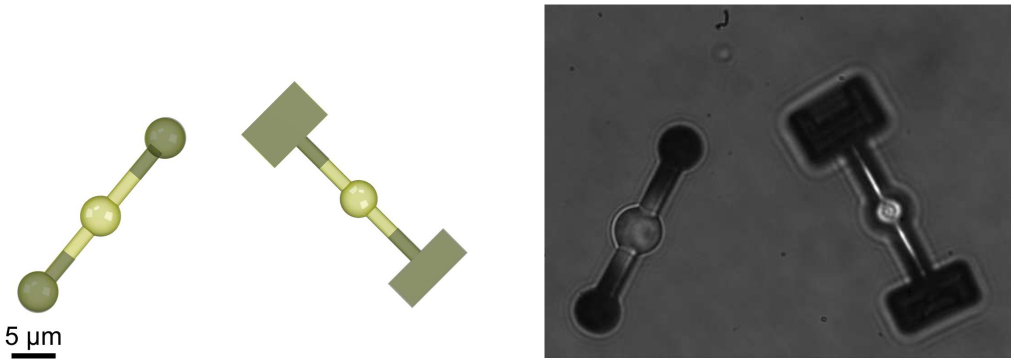

(a) CAD model rendering

(b) Image from Optical Tweezers camera feedback

Figure 3.12: Geometrical model rendering and microscope image in an Optical Tweezers setup of hybrid optical and magnetic microrobots

and are less likely to be attached again on the glass substrate. The duration determines whether the microstructure is partially or fully detached from the glass. A microstructure is partially removed when the mobile components are detached from each other while the base of the microstructure remains attached on the glass substrate. An example of fully and partially detached microrobot, where only the rotating part is detached, are shown in Figure 3.11. In the case of hybrid optical and magnetic microrobots, the mask for deposition is also detached. An indicative image of two hybrid optical and magnetic microstructures acquired from the camera-microscope system inside an Optical Tweezers setup is shown in Figure 3.12.

3.5 Conclusions

This chapter presents the fabrication method of optical and hybrid optical and magnetic microrobots. The main design consideration is how to create 3D multiple component microrobots. Two methods are proposed: The first is one-step 3D printing of a multiple component optically transparent mechanism. The impact of the printing power in feature resolution is also assessed. It is shown that higher laser powers degrade feature resolution and as a result obstructs printing a multiple component mechanisms as their features merge. The second method to create articulated mechanisms is to assemble them using individual components that are simultaneously actuated by the Optical Tweezers and the magnetic field. The methodology of fabricating hybrid optical and magnetic microrobots was described followed by a description of the detachment method used in the experiments. It is stated that individual detachment using a set of mechanical micromanipulators has a lower success rate and than sonication, which is also more suitable for batch microrobot detachment.

Chapter 4

Three-Dimensional Pose Estimation of Optically Transparent Microrobots

This chapter investigates depth and orientation estimation of 3D-printed microrobots inside an Optical Tweezers setup. Section 4.1 describes the problem definition and the geometry of the projection model of the camera-microscope model of an Optical Tweezers imaging system. The detection of the 2D position of the microrobot is described in Section 4.2. In Section 4.3, two methods of depth estimation are presented; i) using the overall sharpness of the image frame which corresponds to features in multiples depths

---

Contents from this chapter have been published in: **Depth estimation of optically transparent laser-driven microrobots**, M. Grammatikopoulou, L. Zhang and G. Yang, In: 2017 IEEE/RSJ International Conference on Intelligent Robots and Systems (IROS) ©2017 IEEE, **Depth Estimation of Optically Transparent Microrobots Using Convolutional and Recurrent Neural Networks**, M. Grammatikopoulou, L. Zhang and G-Z. Yang, In: 2018 IEEE/RSJ International Conference on Intelligent Robots and Systems (IROS) ©2018 IEEE and **Three-Dimensional Pose Estimation of Optically Transparent Microrobots**, M. Grammatikopoulou and G-Z. Yang, In: IEEE Robotics and Automation Letters 2019 (RA-L) ©2019 IEEE from within the object and ii) utilizing the local sharpness around distinct features for single depth recovery at specific regions of the object. The first method aims to provide an overall measurement for the z-displacement of the object, while the second takes into account local changes of sharpness which might be attributed to object 3D rotation rather than displacement along the microscope z-axis. The motivation for the global and the local approach stems from the fact that the overall sharpness measure can not infer directly the depth of a 3D microstructure in case of simultaneous 3D translation and rotation. The proposed methodologies are validated through experimental results which are compared with ground truth data. Section 4.4 investigates depth estimation of optically transparent microrobots of an arbitrary geometry using a learned regression model which is independent of the microrobot's orientation and is robust to different illumination levels. The method relies on a ground truth dataset generated from recorded experimental data used to train and validate the proposed CNN-LSTM model for regression. The proposed model decouples the 3D orientation and translational motion variations of the microrobot. In Section 4.5, orientation estimation is investigated both as separate problem using an optimization-based, a template-based approach and also as part of pose estimation using CNNs. Section 4.6 proposes a methodology for estimating the depth and 3D orientation of a microrobot of known geometrical model in an Optical Tweezers setup. This frameworks attempts to predict the 6-DoF pose of 3D geometries. A supervised learning method using CNNs is employed to estimate the depth of the microrobot and its relative orientation between two image frames. The trained model is validated using microscope ground truth trajectories of three different microrobot designs.

4.1 Problem Definition

This section describes the problem of pose estimation in microrobotic systems compared to macroscale and presents the projection model of such systems.

4.1.1 Pose Estimation Problem in Microrobotics

The conventional Optical Tweezers setup has a single camera, hence stereo methods for 3D reconstructions are not applicable to this and many other microrobotic setups. The camera projection model is also different to macroscale camera systems which are described by the perspective projection model. The microscope-camera model of an Optical Tweezers system is described by the orthographic projection model, in which all rays are parallel to the optical axis and in which the distance along the z-axis between the centre of projection and the projection plane is too large. This results in unobservable motion along the z-axis (Figure 4.1a) while the limited working distance of the microscope lens results in parts of the microrobot being defocused during 3D motion rather than scaling as it happens in the large-scale (Figure 4.1b).

4.1.2 Microscope-Camera Model

Let $\mathbf{p_o} = [p_x \; p_y \; p_z]^T \in \mathbb{R}^3$ and $\mathrm{R_o} = \mathrm{R_x}(a_x)\mathrm{R_y}(a_y)\mathrm{R_z}(a_z) \in \mathbb{R}^{3x3}$ be the position and the orientation of the object frame $\{\mathrm{o}\}$ placed at the centre of mass of the microrobot with respect to a fixed co-ordinate frame, with $\mathrm{R_i}(a_i) \in \mathbb{R}^{3x3}$ the rotation matrix through an angle a_i about the axis i with $i = \{x, y, z\}$ and $\mathrm{R_o}$ the rotation matrix of the frame $\{\mathrm{o}\}$ describing the orientation of the microrobot relative to the fixed frame. The above configuration is imaged through a microscope-camera system described by the

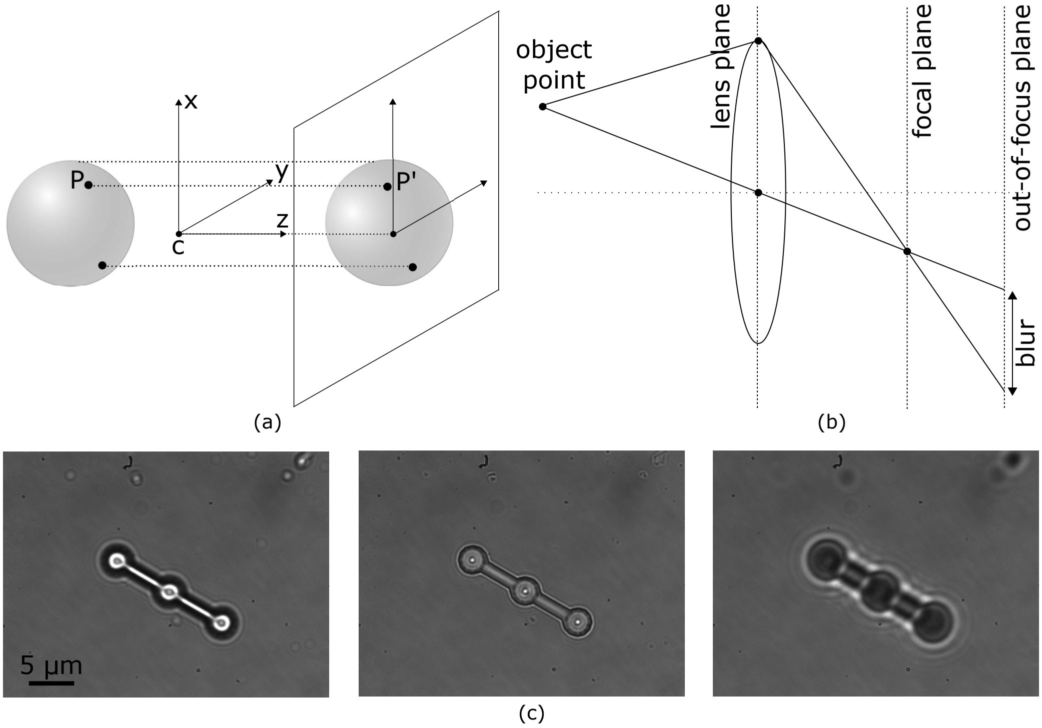

Figure 4.1: The projection model that describes the microscope-camera system (a). The three-dimensional motion results in out-of-focus point on the image (b). An example set of images shows a microrobot as projected on the image plane in different depths along the z-axis, which gives a focused (c-middle) and defocused (c-left and right) images.

orthographic projection model. The projection $\mathbf{p_c} \in \mathbb{R}^2$ of a point $\mathbf{p} \in \mathbb{R}^3$ on the image plane is described as follows:

$$\mathbf{p_c} = \mathrm{KP}\ (\mathrm{R}\mathbf{p} + \mathbf{t}),\ \mathrm{P} = \begin{bmatrix} 1 & 0 & 0 \\ 0 & 1 & 0 \end{bmatrix} \tag{4.1}$$

where $\mathrm{K} \in \mathbb{R}^{2x2}$ the matrix of the intrinsic parameters of the model, P the orthographic projection matrix given by (4.1) and $\mathrm{R} \in \mathbb{R}^{3x3}, \mathbf{t} \in \mathbb{R}^2$ the extrinsic parameters obtained by the registration of the 3D model of the microrobot with the image frame.

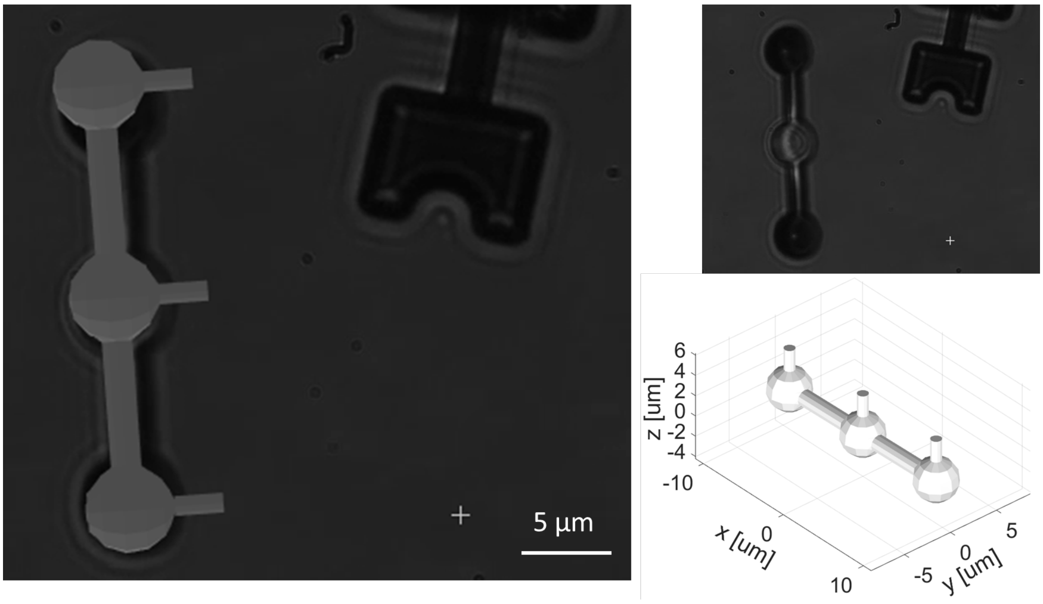

Figure 4.2: An indicative image frame with the registered projection of the geometrical model (left). A rendering of the geometrical model (bottom right) and the image frame with which the CAD model is registered (top right)

4.1.3 Image-Geometrical Model Registration

As the geometrical model of the microrobot is known, it is used to register the microrobot with the image frame during initialization. The corresponding points between the projection of the microrobot on the image plane and the 2D projection of 3D points geometrical model of the microrobot are manually selected for the initial pose. The 2D projection of the 3D points of the geometrical model are registered with the microscope image depicting the initial pose of the microrobot. Once their projection is registered, the extrinsic parameters $\mathrm{R}, \mathbf{t}$ are then estimated as follows, in order to obtain an absolute estimation of the orientation with respect to a fixed co-ordinate frame:

$$
\begin{aligned}
\mathrm{R},\, \mathbf{t} = \arg\min \| \mathbf{p_{ci}} - \mathrm{K}\,\mathrm{P}\,(\mathrm{R}\ \mathbf{p_{Mi}} + \mathbf{t}) \|^2 \\
\text{s.t}\ \ \mathrm{R}^T\,\mathrm{R} = \mathrm{I}_{3\times3}
\end{aligned}
\tag{4.2}
$$

where $\mathbf{p_{Mi}} \in \mathbb{R}^3$ the i_{th} vertex of the point cloud of the geometrical model and $\mathbf{p_{ci}} \in \mathbb{R}^2$ its projection on the image plane. An indicative registered frame with the CAD model of the microrobot is shown in Figure 4.2.

4.2 Microrobot 2D Position Detection

The 2D position of the microrobot is detected as follows: First, edge detection is used followed by discarding small unconnected edges that consist of a number of pixels below a specific threshold. The remaining edges are thickened in order to obtain a closed external contour. Last, as the contour might still not be closed, the convex hull of the detected thickened edges is obtained for the centre calculation. Using the convex hull of the edges might result to a less accurate object contour but is more robust in obtaining a closed area for 2D position calculation.

4.3 Microrobot Depth Estimation using Sharpness Measurements

This section describes two strategies for recovering z-translation using sharpness measurements. The first method gives a depth estimation that describes the overall object displacement. The second method attempts to estimate a local sharpness model for single object features. In the following, the term global sharpness model refers to the function that maps a sharpness value to the corresponding object z position relative to the focus plane approximated by a sum of Gaussian curves. The term local sharpness denotes the approximation of the mapping function that relates a single sharpness value to the corresponding depth of an individual object feature by one Gaussian curve. The motivation for developing these two methods is that the first method does not tackle the problem of interfering object features at different depths that are visible due to transparency. In addition, a holistic focus measurement cannot distinguish whether changes in the sharpness are cause by displacement along the z-axis or by 3D object rotation, as this motion also results to parts of the object being focused or defocused.

4.3.1 Depth Reconstruction using Global Sharpness Model Approximation

This method aims to reconstruct the overall displacement of the object by using a global representation of the sharpness model. This method uses the full image that includes the object without occlusions for sharpness calculation. In order to estimate the translation along the z-axis of the object, the mapping between the sharpness measurements for each image frame and the corresponding z-position of the object must be established. The focus measurement ϕ that is used in this case is the Gaussian Derivative [126]:

$$\phi = \sum (I * G_x)^2 + (I * G_y)^2, \tag{4.3}$$

$$G(x,y) = \frac{1}{2\pi\sigma^2} e^{\left(-\frac{x^2+y2}{2\sigma^2}\right)} \tag{4.4}$$

$$G_x = \frac{\partial G(x,y)}{\partial x},\ G_y \frac{\partial G(x,y)}{\partial y} \tag{4.5}$$

4.3.1.1 Global Sharpness Model Calibration

Prior to estimating the trajectory along the z-axis, a calibration routine has to be performed to establish the mapping between sharpness and the displacement along z. An indicative set of calibration data is shown in Figure 4.3, which include the depth measurements, the image sequence and the corresponding sharpness values for each frame. The calibration trajectory corresponds to scanning the microstructure along its height on an upwards and a downwards trajectory. The calibration data is used to approximate the sharpness model as a function $\phi(z_{total})$ of the overall object displacement z_{total} by fitting a sum of N Gaussian curves (Figure 4.4 - top)

$$\phi(z_{total}) = \sum_{i=1}^{N} \alpha_i e^{-\dfrac{(z_{total} - b_i)^2}{{c_i}^2}} \tag{4.6}$$

where α_i the maximum amplitude of the i_{th} Gaussian term, b_i the depth at which the sharpness is maximum and c_i the standard deviation.

4.3.1.2 Global Depth Reconstruction

The global sharpness approximation as a function of the depth cannot be used directly to reconstruct the z-displacement as the Gaussian functions are not invertible. In particular, it can be seen that two different depths can correspond to the same sharpness value (Figure 4.4). For this reason, the sinusoidal calibration trajectory can be divided in two sections to which a sum of one-sided Gaussian curves can be fitted (Fig 4.4 -(top) left and right of dashed line). The corresponding inverted functions $z_i = f^{-1}(\phi)$ are depicted in Figure 4.4 (bottom) (here $i = 1, 2$). The switching between the curves z_1 and z_2 (Figure 4.4 - left and right of dashed line) is determined

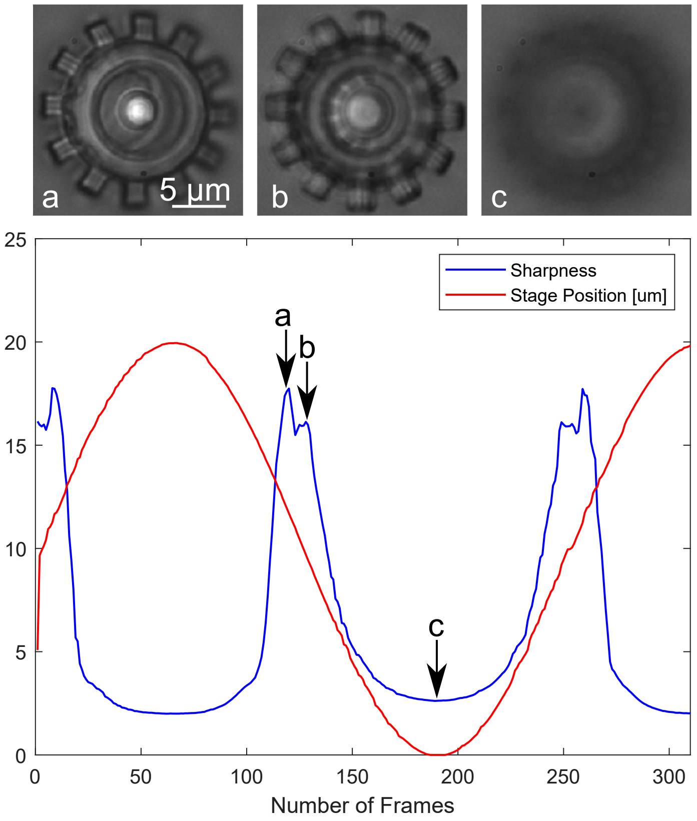

Figure 4.3: Sharpness measurement and ground truth trajectory used in calibration for mapping function approximation

by some conditions. In particular, these switching conditions are defined by the sign of the rate of change of the focus measurement $\Delta\phi$, the sign of the update rate of the estimated depth Δz and the range at which the estimated depth belongs to. Continuous switching can be ensured since a continuous z-trajectory is assumed and high alterations of the depth cannot be performed.

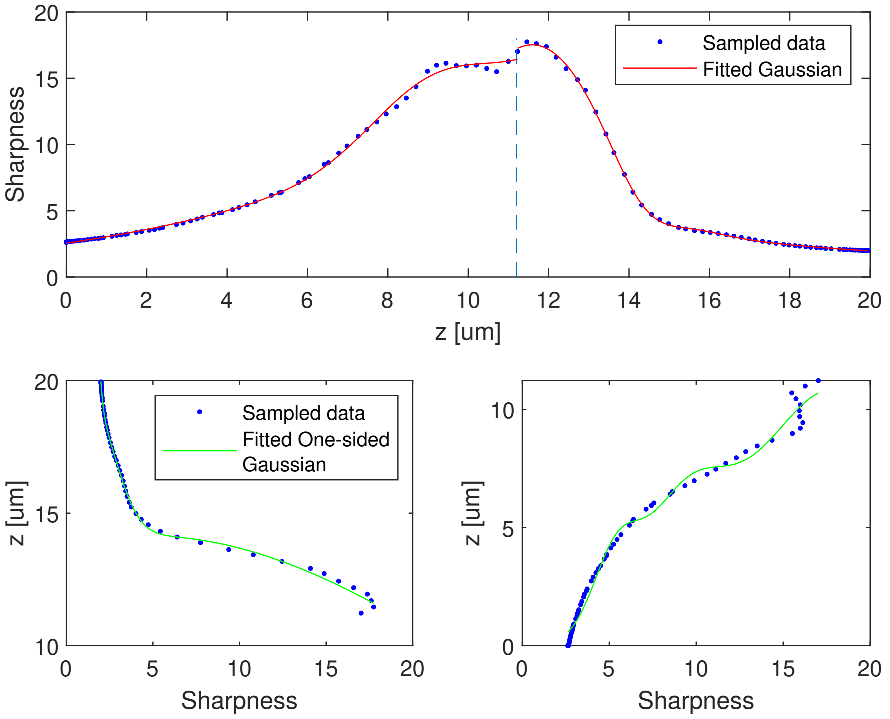

Figure 4.4: Global sharpness model approximation from calibration (top). Inverse sharpness models (bottom)

4.3.2 Depth Estimation using Local Sharpness Model Approximation

The previous approach is sufficient for depth reconstruction when the sharpness functions has a dominant peak that can describe the object displacement along the z-axis. Due to object transparency, the features below or above the focus plane contribute to the total sharpness measurement when using as input to the calculations the whole image frame. This is also indicated by the fact that the sharpness measure for the whole image is approximated by a sum of Gaussian terms. This implies that the contribution of the dominant features of the microstructure to the single sharpness measurement can cor-

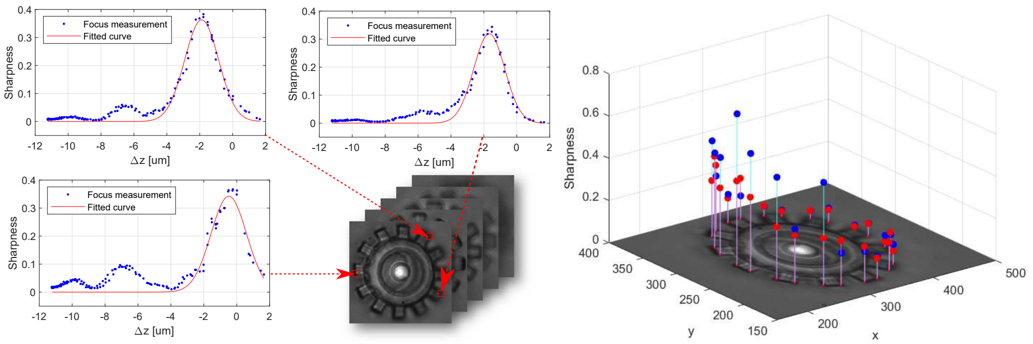

Figure 4.5: Local sharpness model approximations using one Gaussian curve (left). The windows and the corresponding local object pose are also shown. The sharpness values as calculated for each of the selected features (right)

respond to different depths. In addition, during 3D rotation, different parts of the object become defocused, resulting to changes in the overall sharpness measurement. Hence, the overall sharpness measure cannot identify whether defocusing occurs only locally at the object due to rotation or if it is uniform due to translation along the z-axis.

In order to get the corresponding depth of single features, smaller windows around single features of the object are obtained. The centres of the local windows are obtained by the projection of the registered 3D points of the CAD model on the image frame. The initial 3D orientation of the object is estimated as presented in 4.1.3. Estimating the orientation and the 2D position of the object is necessary to obtain a window that contains only the feature of interest.

4.3.2.1 Local Sharpness Model Calibration

Similarly to the global sharpness method, a calibration routine is performed in order to establish the mapping between the sharpness and the depth of a single feature without interference by neighbouring features. It is shown that when the window is sufficiently small and contains single depth features, the sharpness model can be approximated with one Gaussian curve (Figure 4.5). The features which are selected for the calibration are the corners of the teeth of the microgears. A square window of 15x15 pixels, which corresponds to 1.1 μ m^2, around the feature was created assuming that the interference from the neighbouring features is minimized (Figure 4.5). It can be seen that there is a minor overlap between the corner and the edge features of the microgear teeth. However, the overlapping is sufficiently small so that the local sharpness can be approximated by a single Gaussian term. The focus measure which is used in this case is the Gray-Level Normalized Variance [127]. The reason for using a different focus measure in this case is because a normalized measure is needed in order to have the same reference among all the fitted functions. In addition, the Gaussian Derivative is less sensitive to individual smaller peaks caused by the interfering object features.

4.3.2.2 Optimization-based Local Depth Reconstruction

After the local sharpness models are established, the local depth $\hat{z}$ is determined by minimizing the distance between the measured sharpness on the local window ϕ_m and the expected sharpness value from the derived Gaussian curve:

$$\hat{z} = arg\min \left\| \phi_m - \alpha_i e^{-\frac{(\hat{z}-b_i)^2}{{c_i}^2}} \right\| \tag{4.7}$$

By using this optimization method, the individual curves don't need to be inverted. Moreover, by expanding the window more features are included and the right hand side of the equation can be expressed as a sum of Gaussians, using the functions defined for the known features in the calibration procedure.

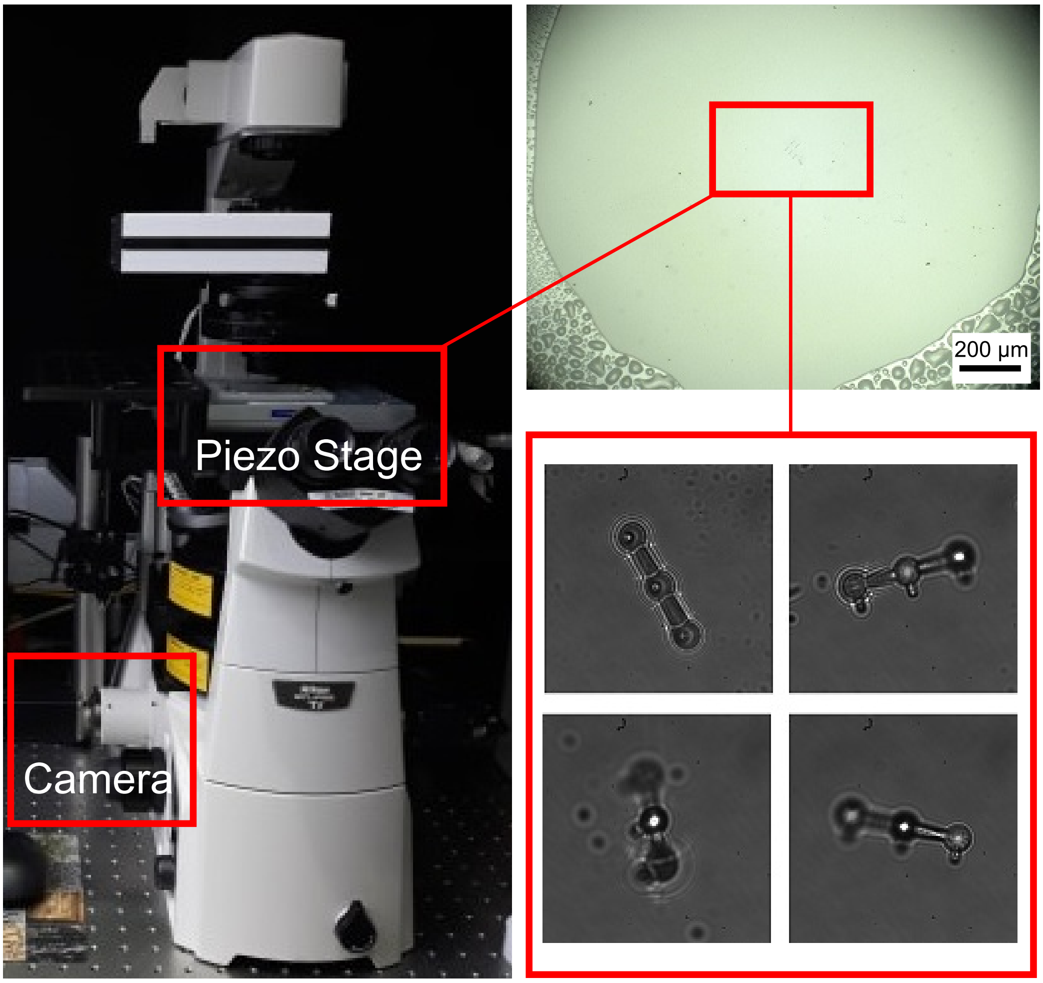

Figure 4.6: The Optical Tweezers experimental setup. The 3D-printed microrobot array was translated using the piezo stage and was imaged through the camera-microscope system.

4.3.3 Experimental Setup

The components of the hardware experimental setup include an acoustic-opto deflector Optical Tweezers (Elliot Scientific, UK) and an integrated 3D micromanipulation piezo stage which is used to simulate the object trajectories. A Charged-coupled Device (CCD) camera (Basler AG, Germany) and an immersion oil lens optical microscope (Nikon Ti) with 100x magnification are used to capture the live feed during the experiment. The experimental setup is shown in Figure 4.6.

4.3.4 Microrobot Fabrication

The designs used in the experiments are 3D-printed gear-shaped microstructures. The height of the structure is 11.2 μm. The microstructures were printed using the Nanonsribe 3D-printer (Nanoscribe, Germany) and the IP-L photoresist. The printing power was set to 25 %. The structures were printed on a glass substrate, placed in deionized water and kept fixed on the glass substrate.

4.3.5 Experimental Results

The proposed methodologies are evaluated and compared to the ground truth data. The object motion is generated by translating the piezo stage along the z-axis and keeping the camera position fixed. The piezo stage trajectory is used as the ground truth data for the experimental validation.

4.3.5.1 Depth Reconstruction using Global Sharpness Approximation Model

The depth of the 3D-printed microstructure is estimated by using the calibrated sharpness approximation model in a new image sequence. The new image sequense is generated by translating the stage by a different trajectory than the calibration one. In this case, a triangular trajectory was chosen but alternative motions could also be performed. The focus measurement of the new sequence is calculated and the resulting sharpness for each frame is shown in Figure 4.7. The calculated sharpness values are used to estimate the depth according to the switching conditions and the calibrated Gaussian

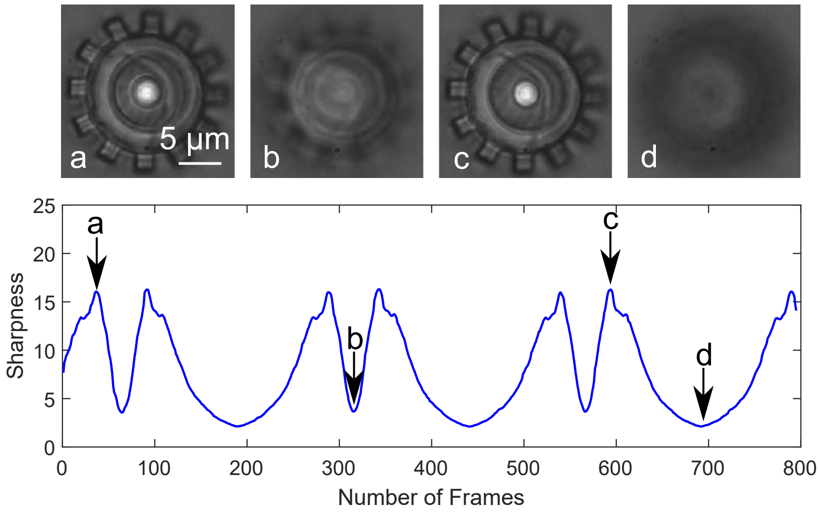

Figure 4.7: Global sharpness measurement using the Gaussian Derivative and the corresponding images from the performed experiment

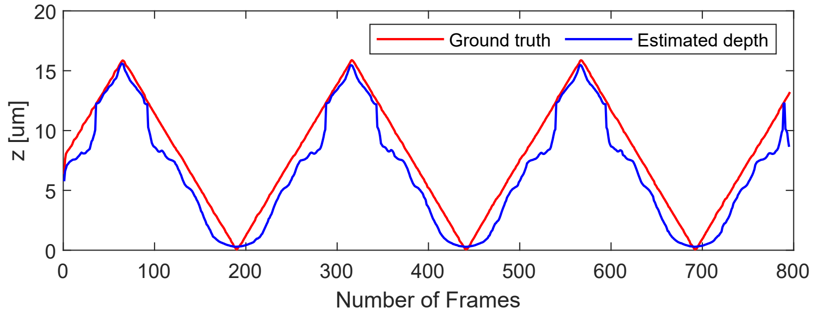

Figure 4.8: The estimated trajectory (blue) and the ground truth trajectory of the piezo stage (red)

model as described in section 4.3.1. As shown in Figure 4.8, the estimated depth trajectory follows the stage trajectory that is used as the ground truth.

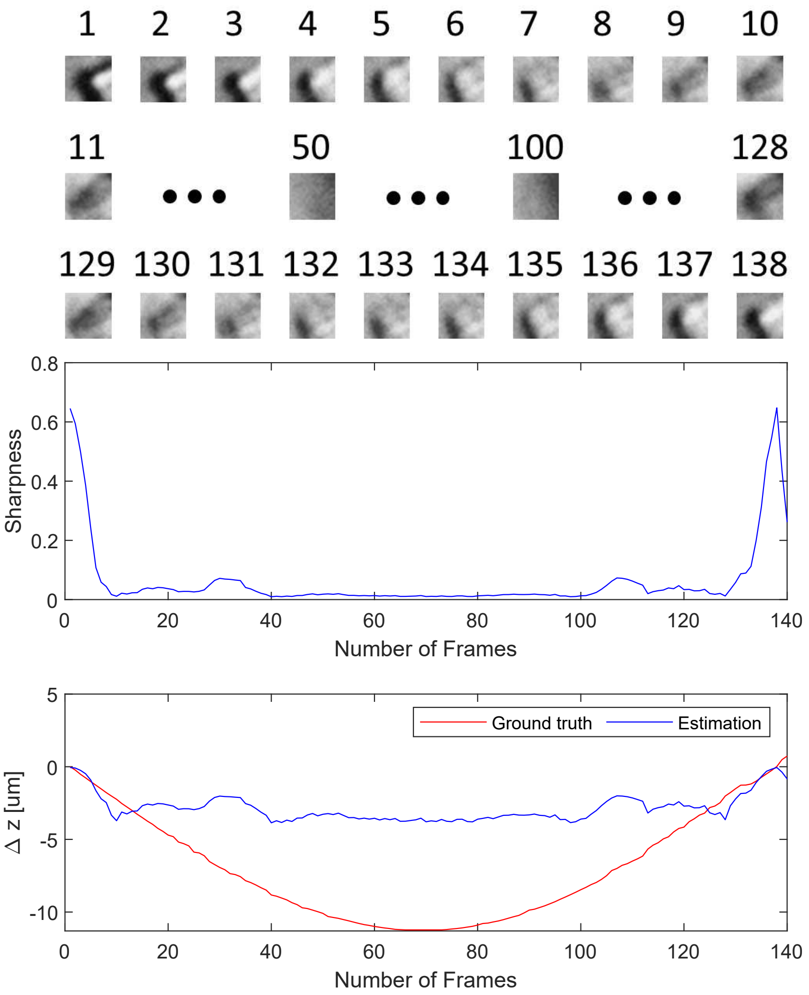

Figure 4.9: An example of local feature depth estimation using the optimization based approach. A set of local windows located at a corner feature (top) are used to calculate the sharpness (middle) of the windows. The estimated and stage relative depth (bottom) shows that the proposed method can be used to estimate local depth information as long as the changes of sharpness can be detected.

4.3.5.2 Depth Reconstruction using Local Sharpness Approximation Model

To confirm that the proposed method can estimate the relative depth of the local features on the microstructure, the translational stage is moved by following a sine wave trajectory. For each local feature, a depth relative to the initial position is estimated by using the calibrated parameters of the 1D Gaussian model. As shown in Figure 4.9 (top), a set of local windows are cropped around the corner features in the sequence of image frames of the performed experiment. The estimated relative depth follows the reference stage movement as long as the sharpness of the window changes. If the sharpness value does not change, which indicates the focus plane does not intersect with the microstructure, the proposed method assumes that the object is static. This could also be attributed to limitations of the used optimization method, which was the Quasi-Newton optimization algorithm. When the focus plane intersects the microstructure again (i.e. part of the object is in focus), the relative depth of the feature can be estimated, as shown in Figure 4.9. It is worth noting that the reconstruction error is similar for all three phases as the object trajectory is periodic.

It is worth noting that the calculated sharpness measures for each individual feature can also reveal information about the object orientation. In particular, Figure 4.5 (right) depicts the selected features as projected on the image and their corresponding sharpness values. It is shown that the features on the right of the gear-shaped microrobot are at lower depths compared to the features on the left. This can also be visually verified since the right features are more blurry than the ones on the right. This information can be fused with the results from a 3D orientation estimation method to account for misalignments in the orientation or detect the out of focus parts of the microstructure. Therefore, the local depth estimation can be related the relative z-displacements of the object features to the estimated orientation.

4.4 Microrobot Depth Estimation using Convolutional Neural Networks and Recurrent Neural Networks

The previous methodologies rely on the calibration routine performed before estimation. The estimated sharpness model corresponds to a specific microrobot orientation. Therefore, each model is valid when the microrobot is only translating and not rotating. In addition, the sharpness model relies on the illumination level of the images obtained during the calibration procedure. To tackle these problem, more high-dimensional features are necessary for depth estimation. CNNs have the advantage of being able to learn high-dimensional data-specific feature maps. To this end, a learning depth regression model is proposed that uses microrobot-specific information from monocular microscope image sequences that show simultaneous microrobot 3D translation and rotation. The aim of the proposed methodology is to estimate the motion of the microrobot along the z-axis independently of i) the microrobot's 3D orientation, ii) the image illumination levels using machine learning to derive a regression model that describes the mapping between the current image frame and the corresponding depth. For 3D-printed microrobots of known geometries, a dataset can be generated consisting of a set of microscope images and the corresponding 3D positions and orientations of the microrobot. The labelled data is used to train a model that predicts the position of the microrobot along the z-axis using as input the current image frame obtained by the microscope-camera system.

4.4.1 Dataset Generation

A ground truth dataset of microscope images of microrobots of known 3D positions and 3D orientations is generated by 3D-printing multiple microrobots in different orientations. The dataset contains sequential and non-sequential orientations for training. The non-sequential data contain orientation displacements up to 5 degrees about each axis while the sampled continuous rotations include orientation differences up to 20 degress for the gear-shaped microrobot and up to 10 for the cylindrical microrobot dataset. For the non-sequential data, in order to generate a representative dataset that spans sufficiently the configuration space of the microrobot, the 3D orientations are drawn randomly from a uniform distribution:

$$p(x) = \begin{cases} \frac{1}{b-a} & \text{if } a \leq x \leq b \\ 0 & \text{otherwise} \end{cases} \tag{4.8}$$

where $x = a_x, a_y, a_z$ with a_x, a_y, a_z the rotation angles about the x, y and z axis of the fixed frame with $a = 0^o$, $b = 360^o$. Hence, the 3D orientation of each microrobot is equal to $R = Rot_x(a_x)\, Rot_y(a_y)\, Rot_z(a_z)$ where $Rot_x(a_x)$, $Rot_y(a_y)$, $Rot_z(a_z)$ the rotation matrices about the x, y, z axis of a fixed frame respectively. In addition, a set of videos of a 360^o rotation about the x-axis performed in steps of 4^o and a rotation of 360^o about the y-axis in steps of 10^o and a fixed rotation of 5^o about the z-axis were acquired. These configurations were chosen so that sequences of frames that correspond to discretized 360^o rotations of the object around different axis are also included.

The microrobots are 3D-printed in specific orientations using the Nanoscribe 3D-printer (Nanoscribe, Germany). The IP-L photoresist was used for

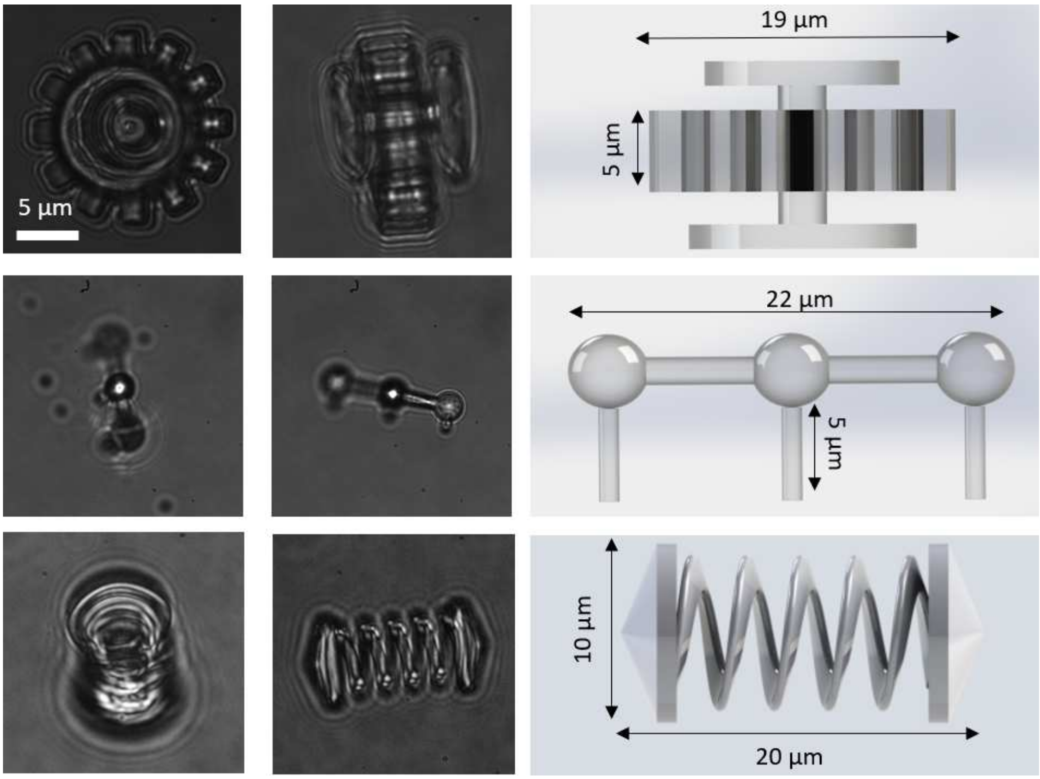

Figure 4.10: Indicative frames from the generated datasets. Three geometries are used for training and validation: The first is a gear-shaped microrobot, the second a cylindrical microrobot with three spherical handles and the third one a helical microrobot.

printing the microrobot arrays following the conventional upwards printing configuration. Three microrobot designs are considered as depicted in Figure 4.10. The first one is a gear-shaped microstructure (Figure 4.10-top), the second geometrical model is a cylinder with three spherical handles (Figure 4.10-middle) which is one of the two component designs of the hybrid optical and magnetic microrobot presented in Chapters 3 and 6, and the third one is a helical microrobot (Figure 4.10-bottom).

4.4.1.1 Data Collection

The printed microrobots are kept fixed on the glass slide and placed on the piezo stage to generate the ground truth trajectories. For each orientation $\boldsymbol{\phi}_i = [\alpha_{xi}\ \alpha_{yi}\ \alpha_{zi}]^T \in \mathbb{R}^3$, the microrobots are translated using the piezo stage along the z-axis to generate the trajectory. Our assumption is that keeping the microrobots fixed on the glass substrate and moving the glass slide with the stage produces an image which is equivalent to keeping the stage fixed and having the microrobots moving freely within the fluid medium as this is the only way of producing ground truth trajectories where the depth and orientation of the microrobots are known. Different levels of illumination are used during image acquisition to make the learned model robust to changes in illumination. Each recorded trajectory consists of 250 image frames that correspond to one orientation and multiple depth values as the microrobot is translated along the z-axis in either a sinusoidal or triangular trajectory. The gear-shaped microrobot dataset consists of 167 discrete orientations while the cylindrical and helical microrobot datasets of 178. As each orientation corresponds to 250 image frames and depth values, the gear-shaped and the cylindrical robot datasets consist of 41750 and 44000 unique image frames with ground truth depth and 3D orientation values respectively. Some example image frames with the corresponding CAD designs of the microrobots are shown in Figure 4.10. For each orientation, the microrobot is translated along a known trajectory on the z-axis by controlling the piezo stage of the microrobotic platform. The range of the motion of the piezo stage is 16.5 μm. This range was chosen as it scans sufficiently the 3D dimensions of the selected designs shown in Fig 4.10. This range minimized the acquisition of frames in which the microrobot is not visible, which is along the smallest dimension of the structure. On the other hand, some configurations are at the limits of range of motion. The illumination levels vary across the captured videos for increased robustness. The first frame of each recorded video corresponds to the position where the microrobot is fully focused, i.e 0 displacement along the z-axis with respect to the focus plane.

4.4.1.2 Data Pre-processing

After the data is collected, each image frame is cropped around the 2D position of the microrobot to contain only the microrobot in the field of view. The original image dimensions are 648 x 488. The 2D detection of the microrobot is performed as in Section 4.2. A further scaling down to 70% of the cropped image is then performed. This is to increase the speed of calculations and the size of data that need to be processed but without removing necessary information for model training. In addition, the images are zero-padded to avoid missing information by applying the convolutional filters on the edges of the image. The depth values are also normalized so that the zero displacement corresponds to the image frame in which the microrobot is most in focus. The dimension of the processed image frame that is given as input to the network is 240x224. The pairs of images for the training set are given as input to the network in a non-sequential order. For the test set, images are ordered in sequences in which the microrobots are in similar depths but in different neighbouring orientations in order to simulate the estimation of a continuous sampled rotation with ground truth data (Figure 4.18 - absolute orientation).

4.4.2 Depth Estimation Network Architecture

The network architecture comprises five convolutional layers combined with a recurrent layer, in particular an LSTM cell. Each convolutional layer is

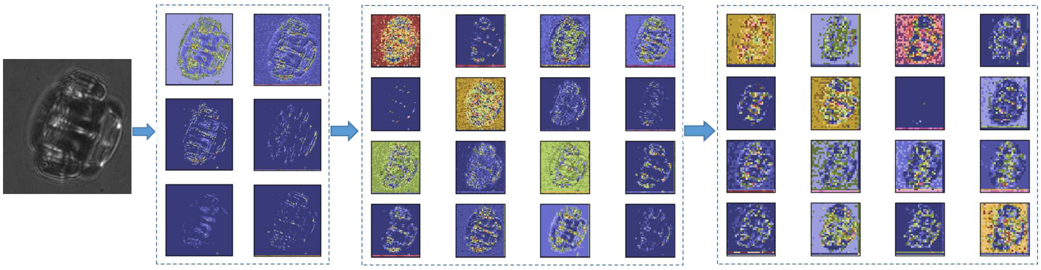

Figure 4.11: Example learned feature maps generated from the first, second and third pair of convolutional and max-pooling layers of the trained network for a given input image. A colormap is used to outline the different intensities within each map.

followed by a max-pooling layer. The convolutional layers are necessary so that the network learns data-specific features which are correlated to the geometry of the microrobot. In comparison to the sharpness measurement used as features in Section 4.3, the learned feature maps describe a more generalized mapping between the current image and the corresponding depth. In particular, features such as image sharpness, depend on the respective 3D orientation of the microrobot and on the image illumination level. The derived feature maps are downsampled by the max-pooling layers. An indicative set of feature maps from the first three convolutional and max-pooling layers of this implementation is shown in Figure 4.11.

Following the convolutional and max-pooling layers, a recurrent layer is used to regress the depth of the microrobot. More specifically, an LSTM cell calculates the output of the regression model. The LSTM cell is preferred to dense layers as it keeps a short-term memory of the previously estimated values minimizing discontinuities in the prediction of continuous trajectories for real-time depth estimation. The cost function $c(\hat{z}_i, z_i)$ is defined as the mean squared error between the output layer values and the corresponding

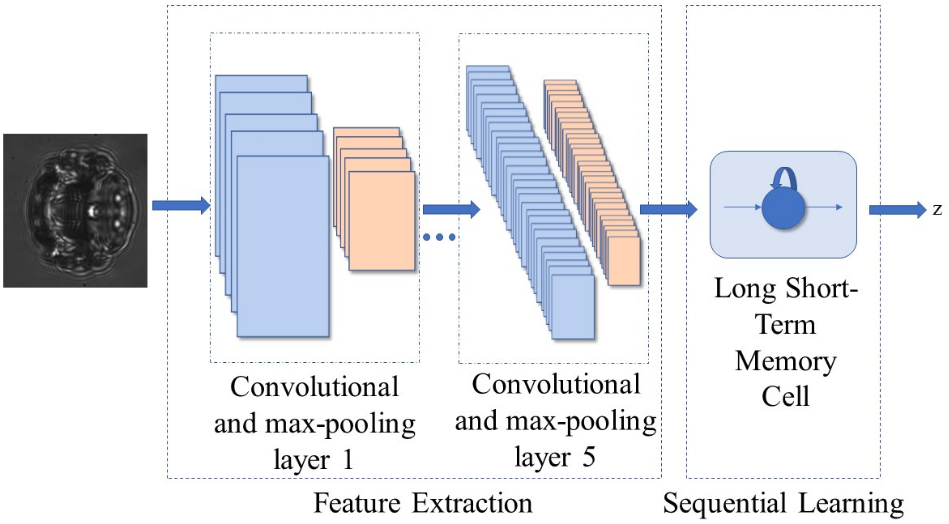
Convolutional and max-pooling layer 1
Convolutional and max-pooling layer 5
Long Short-Term Memory Cell
z
Feature Extraction
Sequential Learning

Figure 4.12: An overview of the proposed architecture. The network consists of five convolutional layers for feature extraction and one LSTM cell which estimates the depth of the microrobot.

Layer		**Parameters**
Convolutional	1	Kernel: 2 × 2, Stride: 1, Filters: 16
Max-pooling	1	Kernel: 2 × 2
Convolutional	2	Kernel: 2 × 2, Stride: 1, Filters: 16
Max-pooling	2	Kernel: 2 × 2
Convolutional	3	Kernel: 2 × 2, Stride: 1, Filters: 32
Max-pooling	3	Kernel: 2 × 2
Convolutional	4	Kernel: 2 × 2, Stride: 1, Filters: 32
Max-pooling	4	Kernel: 2 × 2
Convolutional	5	Kernel: 2 × 2, Stride: 1, Filters: 64
Max-pooling	5	Kernel: 2 × 2
LSTM cell	1	Units: 50

Table 4.1: Depth estimation model parameters

ground truth depth:

$$c(\hat{z}_i, z_i) = \frac{1}{N}\sum_{i=1}^{N}(\hat{z}_i - z_i)^2 \tag{4.9}$$

where $\hat{z}_i, z_i$ the predicted and ground truth depths respectively for the i_{th} sample and N the number of training samples. The optimizer which is used is the Adam Optimizer with learning rate equal to 0.001 while the training set is divided into batches of 20 samples. Each convolutional layer is followed by an exponential linear unit activation function while the LSTM cell is followed by a linear activation function. The number and sequence of layers and the network parameters are given in Table 4.1.

4.4.3 Experimental Setup

The experimental setup consists of an Optical Tweezers (Elliot Scientific, UK) with a mounted XYZ-Axis Nanopositioner (Mad City Labs Inc.). The microrobots are imaged through a high-speed CCD camera (Basler AG, Germany) and an oil immersion lens microscope (Nikon Ti) with 100x magnification. The hardware setup is depicted in Figure 4.6. The regression model is implemented in Python using TensorFlow. A workstation with an NVIDIA GeForce GTX Titan X graphics card, an Intel Xeon CPU (3.4 GHz) and 62.8 GB of RAM was used for the training of the network. The size of the training set is 5.8 GB and the training time was 3 hours and 22 min.

4.4.4 Experimental Results

The design that is used for depth estimation is a gear-shaped microstructure. The geometrical model and the dimensions of the microrobot are shown in Figure 4.10 (top). The array of microrobots was fabricated using Nanoscribe 3D-Printer and the IP-L Photoresist (Nanoscribe, Germany). The laser power was set to 22 % . The printing duration for each microrobot is 20 seconds and each recorded microrobot trajectory has a duration of 8.3 seconds. These times indicate that generating the presented dataset of microscope images and ground truth trajectories for a specific geometrical model is not restrictively time consuming. The dataset can be extended if additional data is neeeded. Furthermore, the dataset for each geometry has to be generated once for each similar imaging setup. The choice of generating a relatively small-sized dataset for learning is to determine what is the minimum amount of data needed for model training without increasing unnecessarily the overhead of the microfabrication and data generation procedures. The microrobot design was selected to demonstrate the tracking of a complex geometry with features visible from within the structure. In an Optical Tweezers setup, the transparency of 3D-printed microrobots is visible and, although it could be overcome by fabricating opaque microstructures, this alteration would significantly impact the trapping force. This particular design could be used for actuation within a microfluidic chip or for cell manipulation. Alternative designs could be used depending on the task and the application.

4.4.4.1 Validation of Microrobot Depth Estimation using the CNN-LSTM Model

In contrast to the training set, the validation set images are not shuffled and are given as input in a sequence of continuous positions in order to assess the prediction of continuous trajectories. The order in which the test set images are given as input to the model can be inferred from the ground truth trajectories shown in Figure 4.13 (top). The trajectories are either sinusoidal, triangular or saw-tooth waves but alternative trajectories could be performed. Each peak corresponds to a separate trajectory and a different microrobot 3D orientation, as shown in Fig 4.14. Figure 4.15 depicts the result of estimating a sinusoidal and a triangular trajectory along the z-axis

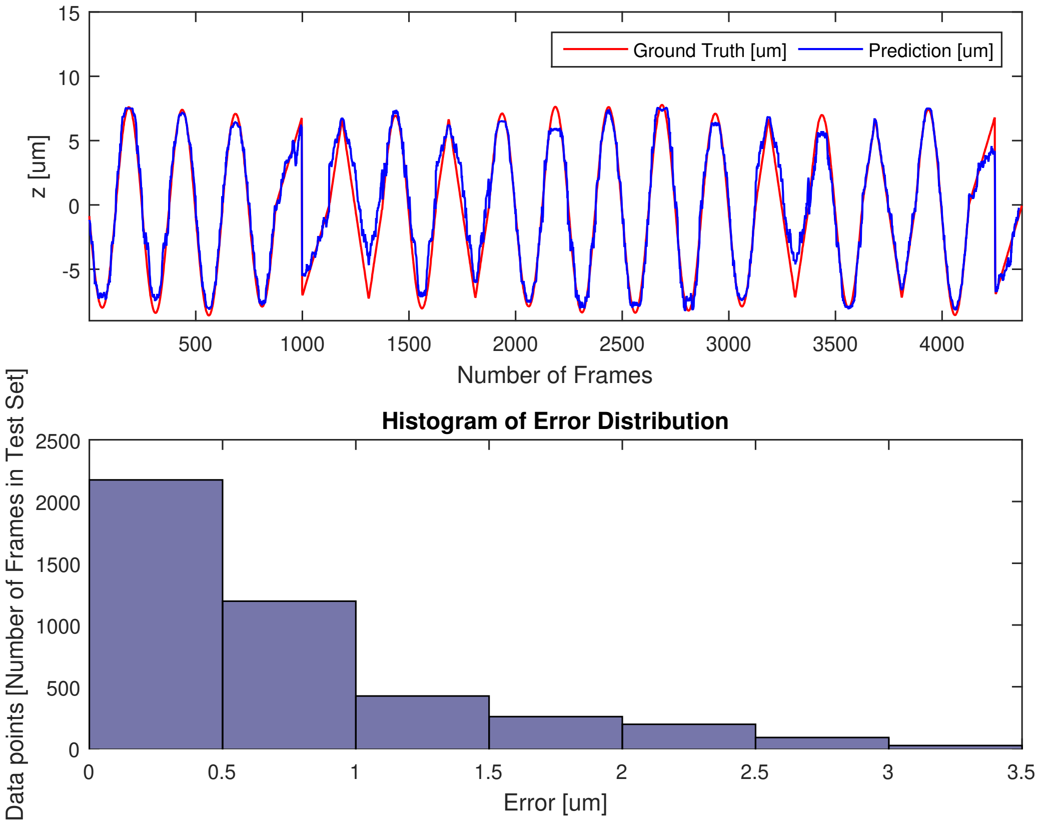

Figure 4.13: The validation results showing the sequence in which the data is given as input to the network (top). A histogram of the error distribution shows the range of error between the prediction and the ground truth for the test set (bottom).

for microrobots of different orientation using the pre-trained regression model presented in Section 4.4.2.

Metric		**Value**
Median error	$[\mu m]$	0.501
Mean error	$[\mu m]$	0.708
Minimum error	$[\mu m]$	0.0001
Maximum error	$[\mu m]$	3.45

Table 4.2: Metrics for validation of microrobot depth estimation

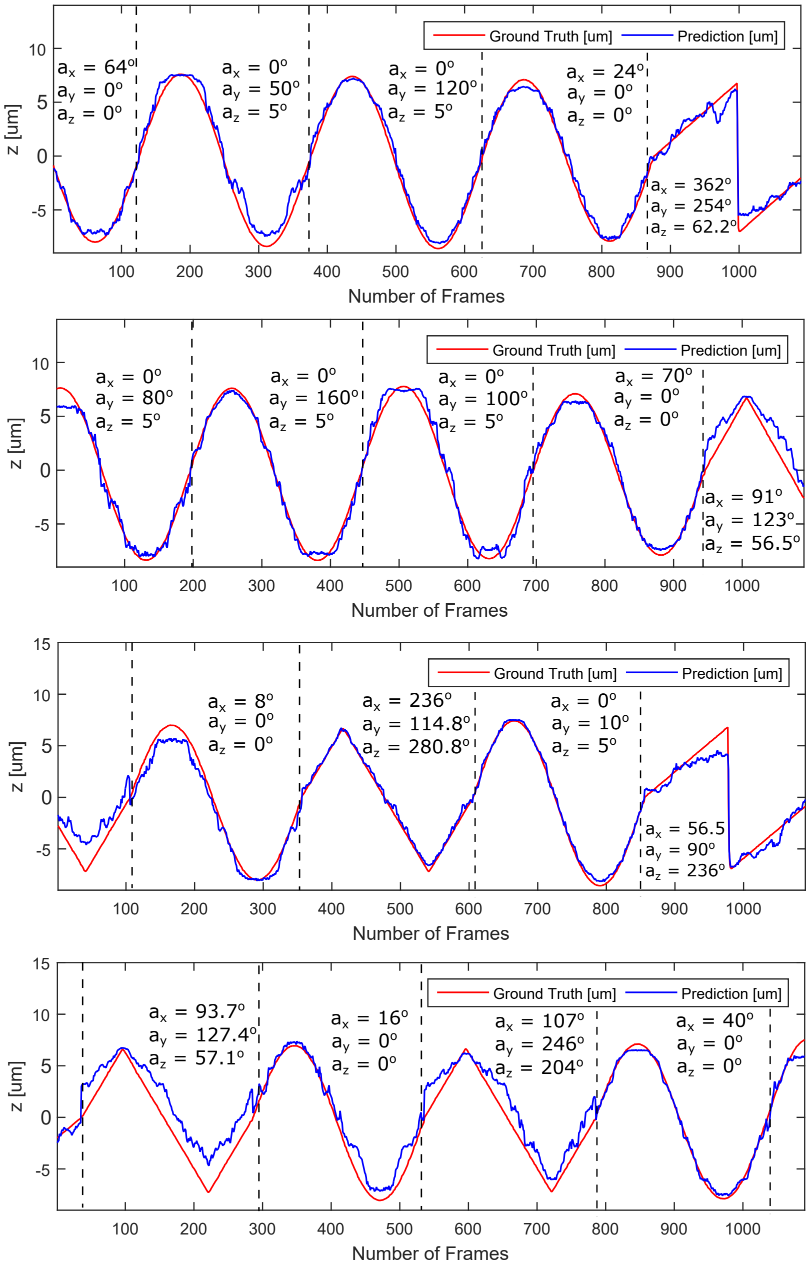

Figure 4.14: A more detailed overview of the predicted trajectories. The figures depict the prediction (blue) in comparison to the ground truth depth (red). The dashed lines separate the trajectories that correspond to different microrobot 3D orientations as stated in the figure.

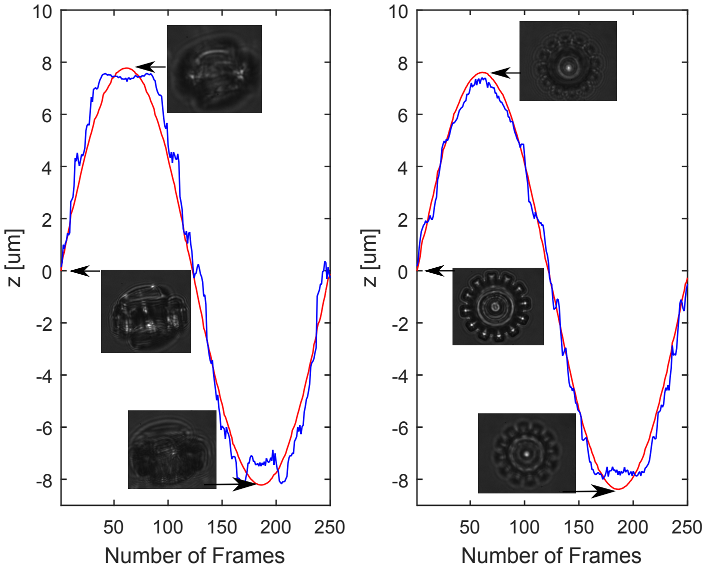

(a) Sinusoidal trajectory

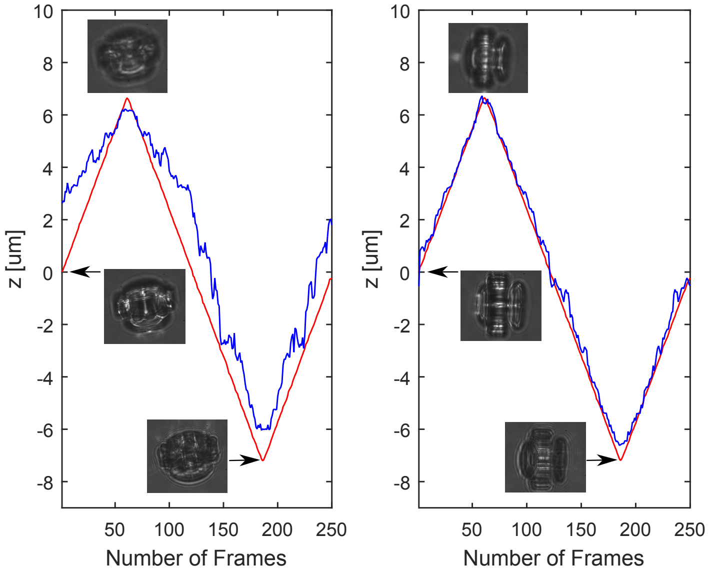

(b) Triangular trajectory

Figure 4.15: Trajectory reconstructions of microrobots with different orientations following the same trajectory

4.4.4.2 Results and Discussion

The depth values estimated by the proposed trained CNN-LSTM network are depicted in Figure 4.14 for a more detailed overview. The metrics used to assess the accuracy of the predictions are shown in Table 4.2. The mean error is 0.708 μm, which indicates that in average the model demonstrates submicron accuracy. In order to asses the effect of outlier error values to the mean value, the median error is also calculated which is equal to 0.501 μm. The calculated median error is equal to 3 % of the overall range of the motion (16.4 μm) (Table 4.2). It is also worth noting that the the error ranges from 3 to 3.45 μm (maximum error - Table 4.2) for 24 images out of 4360 as it can be seen in Figure 4.13 (bottom). Finally, for 88 % of the predicted values the error is below 1.64 μm which is equal to 10 % of the range of motion. The histogram of the error distribution for the test set is shown in Figure 4.13 (bottom).

The presented metrics show that the trained model can reconstruct the continuous trajectories that belong to the test set although the frames during training were randomly re-ordered. In Figure 4.15, the same trajectory is followed by microrobots with different 3D orientations. Figure 4.15 shows that an indicative sinusoidal and triangular set of trajectories can be estimated for the given test set images. Figure 4.15b indicates that the error range is varying between the reconstructions. This could be attributed to the fact that similar images might have already been used during training resulting to a more accurate prediction. This error could be reduced by adding more data to the training and testing set. The microrobot's pose at the top, bottom and middle of the trajectory are also shown in Figure 4.15.

As mentioned, the motivation for training the network with a small-sized dataset is to determine whether a regression model can be trained without generating a large number of training and testing data, making the proposed method more applicable for real-time estimation and to reduce overhead in computation and dataset generation. Since the CAD model of the microstructure is available, the dataset can be extended for further training.

4.5 Microrobot Orientation Estimation

In this section, a model-based orientation estimation method is described. The optimization-based orientation estimation method presented in Section 4.1.3 requires known point correspondences. As it is restrictive to assume accurate knowledge of point correspondences in every image frame, a template-based method is also proposed which is based on matching the appearance of the image frame to the best match from a number of generated templated of possible orientations.

4.5.1 3D Model-based Orientation Estimation

The 3D orientation of the microstructure is estimated using online model-based templates. The motivation for using model-based template matching rather than the optimization problem defined in Section 4.1.3 is that the feature correspondences need to be tracked in every subsequent frame. This is not feasible when the object is rotating in the 3D space since the initial correspondences might be occluded and also not be clearly visible due to image blurriness. The templates are generated from a number of possible relative rotations by an angle step $\Delta\theta$ with respect to the current orientation of the microstructure. The generated templates are matched with the filled extracted object contour on the current image frame. Kalman filtering is also performed for more consistent orientation estimation.

4.5.1.1 Orientation Estimation with Online Template Generation

The optimization approach of Section 4.1.3 needs robust tracking of the corresponding points at each subsequent frame. It also requires that the corresponding features are always visible. Therefore, template matching is employed in this stage using online generated templates derived relatively to the previously estimated object orientation. The templates are generated from a series of all possible orientation changes, i.e all possible rotations around the axis of the global frame, by a small angle step $\Delta\theta$, including the last estimated orientation. The possible micro-gear orientations are projected on the image plane to create the library of the templates. The number of generated templates is constant for every iteration. The similarity measure which is used for the matching is the normalized cross-correlation which is equal to:

$$\gamma = \frac{\sum\limits_{x,y}(I(x,y) - \bar{I}_{u,v})(t_m(x-u,y-v) - \bar{t}_m)}{\left(\sum\limits_{x,y}(I(x,y) - \bar{I}_{u,v})^2 \sum\limits_{x,y}(t_m(x-u,y-v) - \bar{t}_m)^2\right)^{0.5}} \tag{4.10}$$

where I the processed current image, $\bar{t}_m$ the mean of the template and $\bar{I}_{u,v}$ the mean of the region within the template. The recovered rotation from an indicative motion sequence is shown in demonstrated in the experiments of Section 5.2.

4.6 Microrobot Pose Estimation

The previously presented template-based orientation estimation method relies on online template generation, which can be time consuming for real-time estimation. In addition, as only a finite number of templates can be generated from discrete and fixed angle steps, an error will always exist between the template pose and the actual microrobot pose. Moreover, it is desirable that depth and orientation are combined into a unified framework. This section presents a methodology for estimating the depth and 3D orientation of a microrobot of known geometrical model in an Optical Tweezers setup using supervised learning in a unified framework. Estimating the orientation is a more complex problem than depth estimation. The orientation space has a higher dimension and is not a Euclidean space but a Riemmanian manifold. Therefore, estimating a pose globally from a single image is a challenging problem. A global search of the whole orientation space is difficult due to ambiguities and due to the existence of multiple solutions. However, in this method, relative differences are estimated localizing the search in the mathematical space and, hence, not facing ambiguity issues. This is more intuitive as continuous trajectories are estimated and, therefore, the consecutive orientations are close. For this reason, the Euler angle representation is chosen to describe the orientation. In the following, the network architecture is presented followed by a description of the experimental setup and the validation results.

4.6.1 Depth and Relative Orientation Estimation

The z co-ordinate and the 3D relative orientation of the object are calculated using a CNN model. The absolute 3D orientation of the microrobot is obtained by registering the virtual geometrical model with the initial microrobot pose as described in Section 4.1.3. It assumed that the microrobot is registered in the beginning of every estimation process to obtain the absolute orientation.

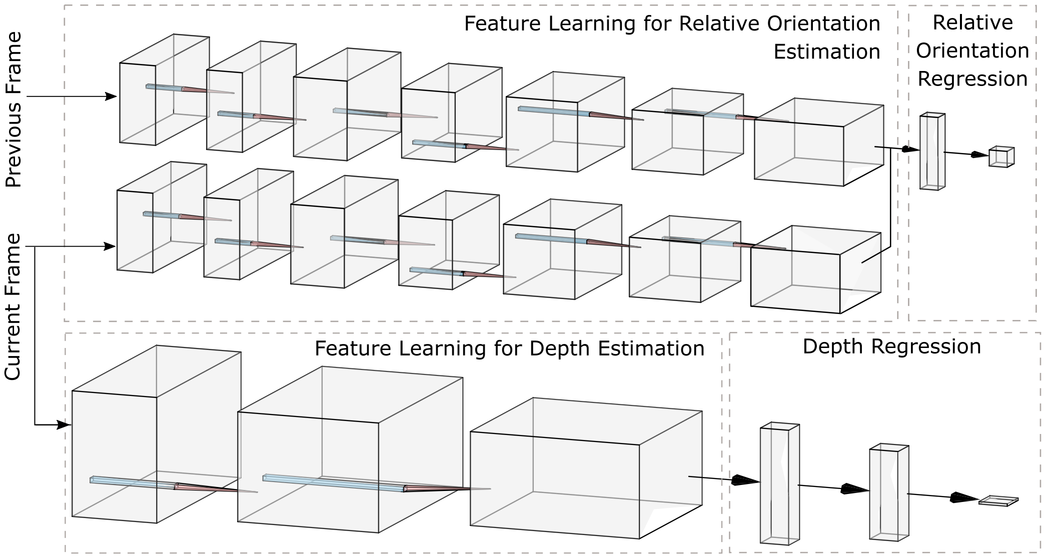
Previous Frame
Current Frame
Feature Learning for Relative Orientation Estimation
Relative Orientation Regression
Feature Learning for Depth Estimation
Depth Regression

Figure 4.16: The proposed network architecture. The model consists of a network for relative orientation estimation and one for depth estimation using as input two image frames.

4.6.2 Pose Estimation Network Architecture

The model comprises two networks: one for relative orientation estimation and one for depth estimation (Figure 4.16). The network for the relative orientation between the poses receives as input a pair of images, i.e the current and previous video frame $\mathrm{Im}_{\mathrm{curr}}$ and $\mathrm{Im}_{\mathrm{prev}}$, and a single image for depth estimation which is the current video frame $\mathrm{Im}_{\mathrm{curr}}$. The label used for training for each pair of images is their relative rotation angles about the axis x,y and z-axis:

$$\boldsymbol{\Delta}\phi_i = \boldsymbol{\phi}_{curr} - \boldsymbol{\phi}_{prev} = [\Delta\alpha_x \ \Delta\alpha_y \ \Delta\alpha_z]^T \in \mathbb{R}^3 \tag{4.11}$$

where $\Delta\alpha_i = \alpha_{icurr} - \alpha_{iprev}$ with $i = \{x, y, z\}$. The depth estimation component receives the image $\mathrm{Im}_{\mathrm{curr}}$ as input and the corresponding z co-ordinate. The model parameters are given in Table 4.3. The activation function for all

Depth Estimation Network Parameters

Layer		Parameters
Convolutional	1	Kernel: 2x2, Stride:1, Filters: 8
Max-pooling	1	Kernel: 2x2
Convolutional	2	Kernel: 2x2, Stride:1, Filters: 32
Max-pooling	2	Kernel: 2x2
Convolutional	3	Kernel: 2x2, Stride:1, Filters: 64
Max-pooling	3	Kernel: 2x2
Fully Connected	1	Neurons: 150
Fully Connected	2	Neurons: 50
Output		Neurons: 1

Relative Orientation Estimation Network Parameters

Layer		Parameters
Convolutional	1_0	Kernel: 2x2, Stride:1, Filters: 4
Convolutional	1_1	Kernel: 2x2, Stride:1, Filters: 4
Convolutional	1_2	Kernel: 2x2, Stride:1, Filters: 8
Max-pooling	1	Kernel: 2x2
Convolutional	2_0	Kernel: 2x2, Stride:1, Filters: 8
Convolutional	2_1	Kernel: 2x2, Stride:1, Filters: 16
Max-pooling	2	Kernel: 2x2
Convolutional	3_0	Kernel: 2x2, Stride:1, Filters: 16
Convolutional	3_1	Kernel: 2x2, Stride:1, Filters: 32
Max-pooling	3	Kernel: 2x2
Fully Connected	1	Neurons: 150
Output		Neurons: 3

Table 4.3: Pose estimation network parameters

the convolutional and dense layers is the rectified linear unit function, except for the last dense layer of each network which is a linear activation function.

The two networks are trained simultaneously using the Adam Optimizer and the following cost function:

$$c = \frac{1}{N}\left(\sum_{i=0}^{N} \|z_i - \hat{z}_i\|^2 + \sum_{i=0}^{N} \|\Delta\phi_i - \Delta\hat{\phi}_i\|^2 \right) \tag{4.12}$$

where z_i and $\hat{z}_i \in \mathbb{R}$ are the ground truth and estimated values of the z coordinate respectively, $\Delta\phi_i = [\Delta\alpha_x\ \Delta\alpha_y\ \Delta\alpha_z]^T$ and $\Delta\hat{\phi}_i = [\Delta\hat{\alpha}_x\ \Delta\hat{\alpha}_y\ \Delta\hat{\alpha}_z]^T$ $\in \mathbb{R}^3$ the ground truth and estimated relative rotation angles about the axis x, y and z respectively between the two poses that correspond to the input image frames and N the total number of samples with $i = \{0, .., N\}$. The estimated depth values are further filtered using a median filter.

4.6.3 Experimental Setup

The experimental setup is depicted in Figure 4.6. The setup consists of an Optical Tweezers system (Elliot Scientific, UK) with a mounted 3D piezo stage (Mad City Labs Inc). The microrobots are observed through a microscope-camera system of a CCD Camera (Basler AG, Germany) and an 100x magnification oil immersion objective lens (Nikon Ti) with 1.45 Numerical Aperture (NA) and 0.13 mm Working Distance (WD). For the pose estimation component, the model was implemented in Python using TensorFlow. The model was trained on a workstation with an Intel Core i9-7940X CPU (3.1 GHz), a GeForce GTX Titax Xp GPU (NVidia Corporation) and 64 GB of RAM.

4.6.4 Experimental Results

The network was trained for each geometry separately using 10500 for the gear-shaped microrobot, 11700 pairs of images for cylindrical and 11700 pairs of images for the helical microrobot. The depth estimation network uses only

		Mean	**Median**	**Mean**	**Median**	**Mean**	**Median**
α_x	[deg]	7.58	5.8	5.08	3.65	4.36	2.16
α_y	[deg]	10.53	6.77	5.48	3.53	3.57	2.3
α_z	[deg]	4.78	3.32	7.38	4.99	8.86	4.63
z	[μm]	1.73	1.14	0.81	0.63	0.78	0.6
z (filtered)	[μm]	1.53	0.95	0.61	0.504	0.599	0.47

Table 4.4: Metrics for gear-shaped (left), cylindrical (middle) and helical microrobot (right) datasets

the current image frame for training and hence 10500, 11700 and 11700 single images for each dataset respectively.

4.6.4.1 Test Set Validation

As mentioned, the dataset contains images of three different designs of microrobots. As mentioned in order to test the model on continuous trajectories, the images which are in similar depths but in different discrete orientations are given as input to the networks as a sequence. Figure 4.18, 4.19 and 4.20 depict the validation results for absolute orientation and depth for the gear-shaped, cylindrical and helical microrobot datasets respectively. Each peak of the orientation graphs corresponds to a separate trajectory with a new initial pose. The initial pose for each trajectory can be obtained by registering the geometrical model of the microrobot with the image frame as described in Section 4.1.3. The results for the absolute orientations are derived by adding the relative orientations estimated by the model to the initial pose as obtained after the registration procedure. The estimated relative orientations for the cylindrical microrobot dataset is shown in Figure 4.17.

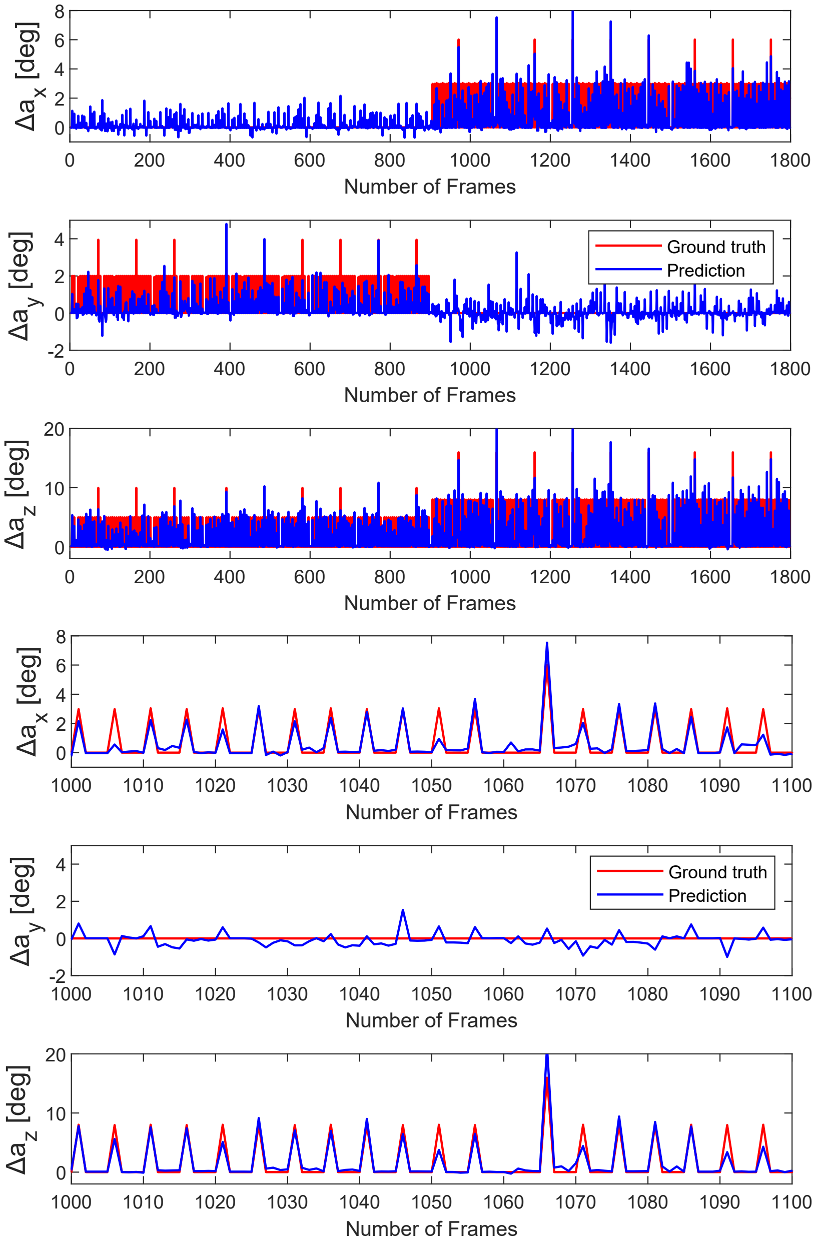

Figure 4.17: Estimated and ground truth of the relative orientations for the cylindrical microrobot dataset

4.6.4.2 Results and Discussion

The metrics that are used to describe the validation results are the mean and median error between the ground truth and estimated values of the

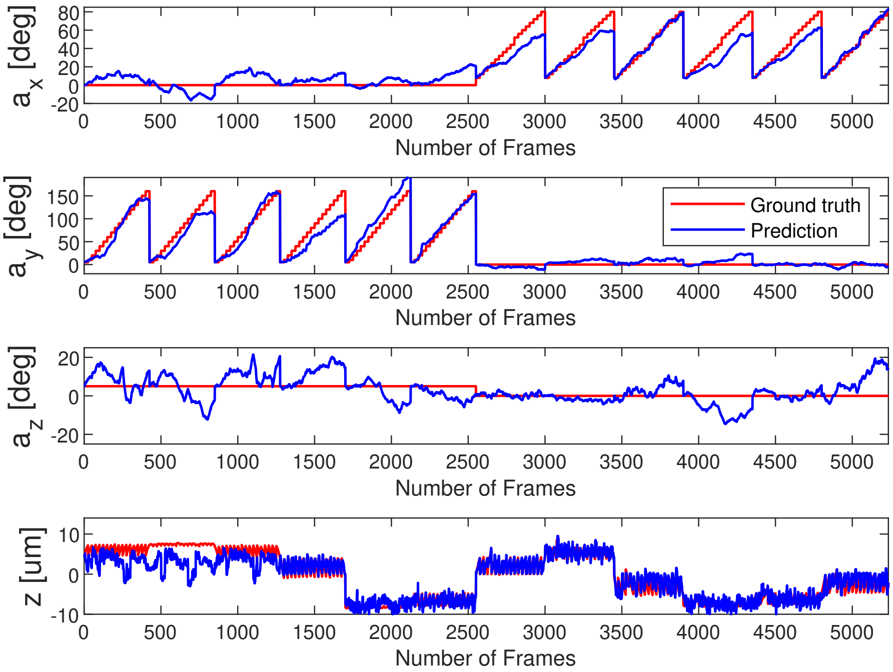

Figure 4.18: Estimated and ground truth values of the absolute orientations and depth for the gear-shaped microrobot

absolute orientation angles about the x,y and z-axis in degrees and depth and the corresponding ground truth values. The mean orientation error of the rotation angles about the x,y and z axis and depth values for the gear-shaped, cylindrical and helical microrobots are given in Table 4.4.

The estimated orientations for the gear-shaped microrobot dataset present larger errors in smaller relative orientations than for the cylindrical and helical microrobot dataset. This is visible by the estimated angles around the zero values (Figure 4.18- a_z and Figure 4.19-a_y and 4.20-a_y). This is partly because the cylindrical and helical microrobot datasets contain more pairs of image frames in which the relative rotation is smaller. This error could be potentially improved by extending the dataset to include more angle vari-

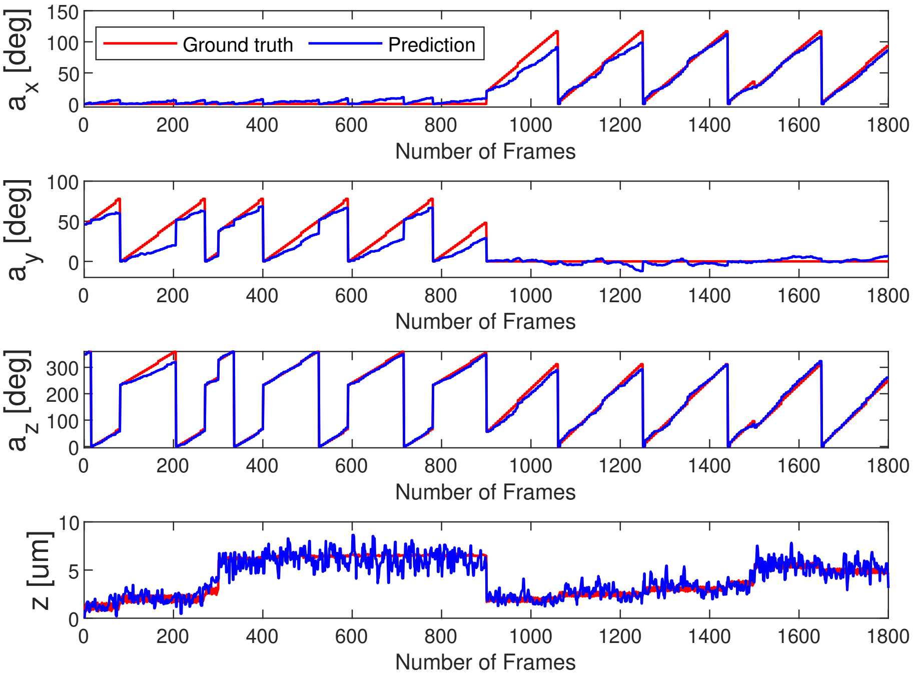

Figure 4.19: Estimated and ground truth values of the absolute orientations and depth for the cylindrical microrobot

ations. However, we present the results with the existing angle variations and dataset size for each set of images, in order to assess the impact of the range variation and dataset size on the estimation. In addition, the dataset is medium-sized and adding more images for each geometry would improve accuracy if the selected poses span the configuration space sufficiently. The reason for generating a medium-sized dataset is to find a size for the dataset that allows for the method to be applicable and implemented easily in case of different geometries since its applicability would be limited if it requires very large datasets. Moreover, the geometry has an influence on the accuracy, as the derived features from the training of the convolutional layers give geometry specific features maps. Another source of error is that, as this method

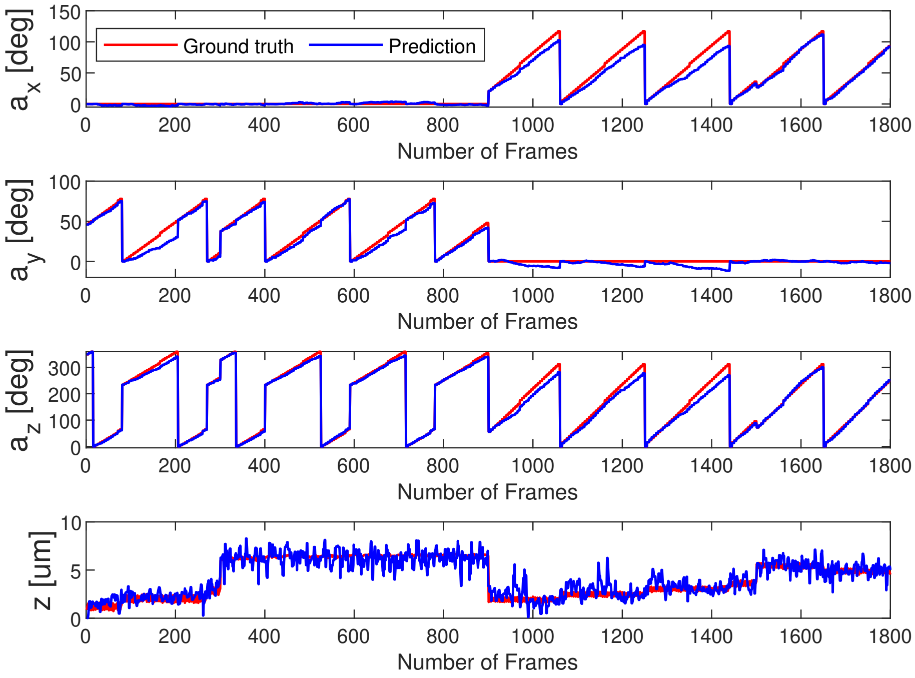

Figure 4.20: Estimated and ground truth values of the absolute orientations and depth for the helical microrobot

calculates relative orientations in order to obtain the absolute orientation of the microrobot, the absolute estimation drifts as the error is accumulated. This could be improved by updating the registration after a number of frames in order to get a new absolute orientation estimation, by using algorithms such as feature matching. The results present the errors of the filtered and unfiltered estimated depths. Filtering was preferred rather than training a more complex model as using a median filter is also fast and applicable in real-time detection. In addition, filtering refines the estimations without having to train the networks for the orientation and depth estimation separately with different numbers of data. As mentioned, the input to the overall network is the current and previous image frame. However, the model does not require two consecutive frames as input allowing missed frames during real-time image acquisition. It is also worth noting that the estimation is performed on image frames with a single geometry in the view. This could be extended to multiple geometries by adding a prior classification step to perform image segmentation around each geometry. As the geometries that need to be detected are known in advance, the image can be segmented and then give the respective segmented images as input to the respective trained model. Last, the depth estimation component could be improved to include the estimation of sequential data by replacing the fully connected layers with LSTM cells, similarly to Section 4.4.

4.6.4.3 Comparison with VGG16 Feature Extraction Model Pre-trained on ImageNet

The proposed model is compared to the VGG16 model [128] in order to further assess its performance using as test set the cylindrical microrobot dataset. As the VGG16 model is designed for image classification, we only keep the feature extraction part of the network as defined in [128] and we use the same architecture of fully connected layers for depth and relative orientation estimation as presented in Section 4.6.2 and specified in Table 4.3, on top of the pre-trained feature extraction component. The weights which are used for the feature extraction component of the VGG16 model are the ones obtained after training with the ImageNet dataset [129]. The motivation of using the VGG16 model is to use for the comparison a network which has a similar size to the proposed one. In addition, the weights of the pre-trained VGG16 model on ImageNet are used in order to compare the proposed feature extraction using our smaller task-specific dataset of grayscale images to a feature extraction component which was trained using

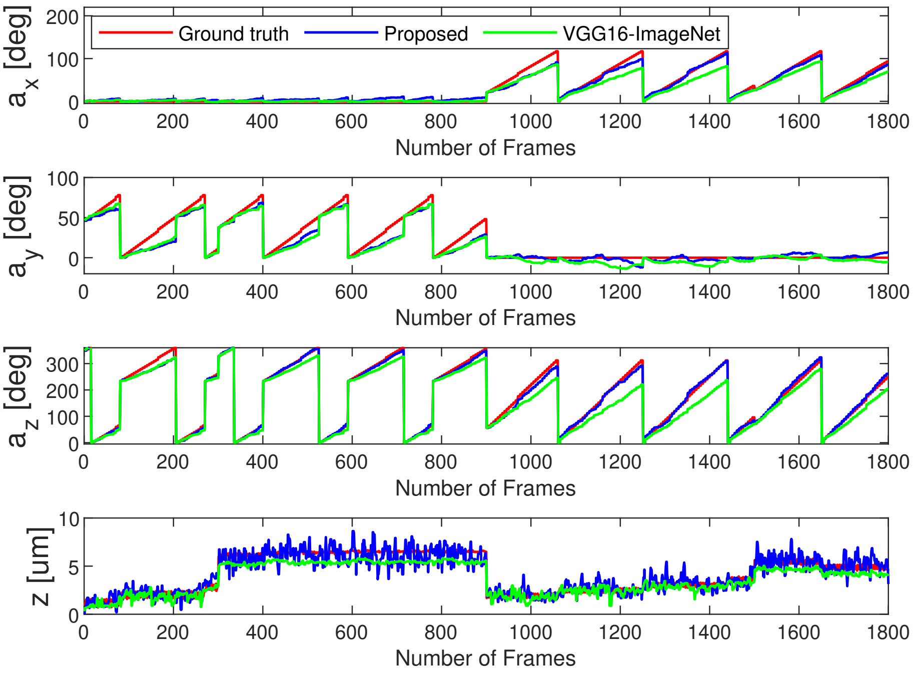

Figure 4.21: Estimated and ground truth values of the absolute orientations and depth for the cylindrical microrobot using the proposed and VGG16-ImageNet pre-trained networks

		Mean	**Median**	**Mean**	**Median**
α_x	[deg]	5.08	3.65	7.13	1.93
α_y	[deg]	5.48	3.53	6.53	4.89
α_z	[deg]	7.38	4.99	22.76	17.71
z	[μm]	0.81	0.63	0.62	0.65
z (filtered)	[μm]	0.61	0.504	0.62	0.65

Table 4.5: Metrics for proposed (left) and VGG16 pre-trained on ImageNet (right) models for the cylindrical microrobot dataset

a generic RGB very large dataset. The regression model is trained using the cylindrical microrobot dataser while the ImageNet weights for feature extraction are frozen.

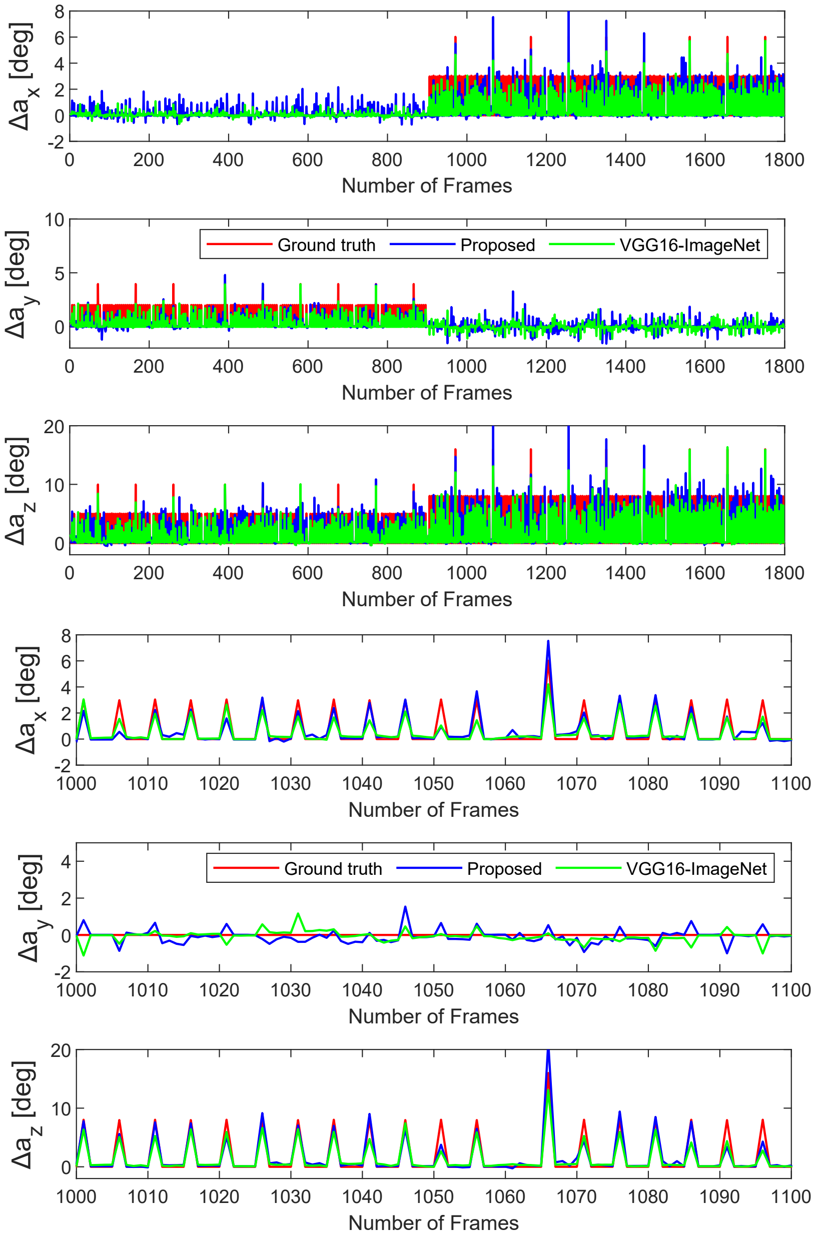

Figure 4.22: Estimated and ground truth values of the relative orientations for the cylindrical microrobot using the proposed and VGG16-ImageNet pretrained networks

4.6.4.4 Results and Discussion

The comparative results are given in Table 4.5. The mean and median errors for the estimated absolute orientations are overall slightly higher for the pre-

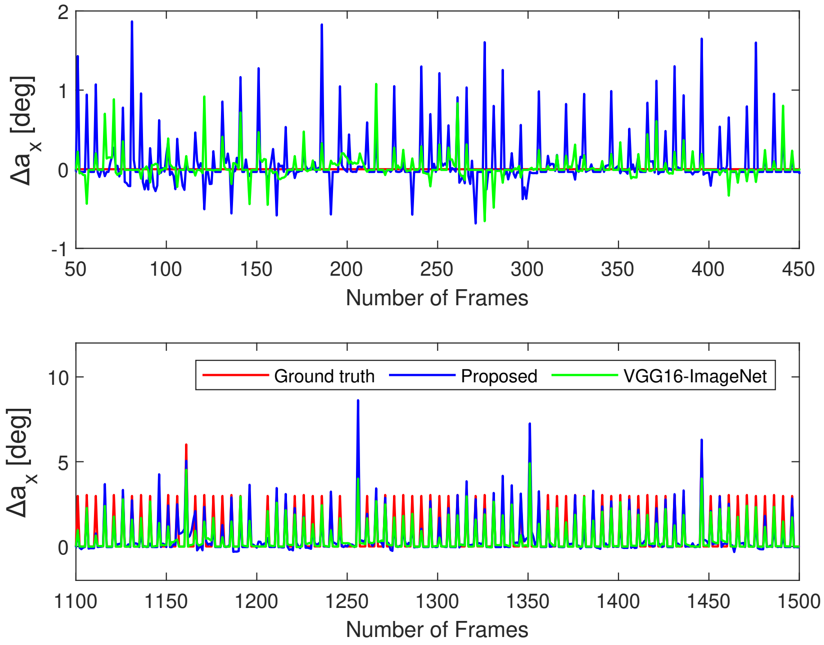

Figure 4.23: Estimated and ground truth values of the relative orientations about the x-axis for the cylindrical microrobot using the proposed and VGG16-ImageNet pre-trained networks

trained VGG16 model than for the proposed model, except for the median orientation error along the x-axis which is smaller. The relative orientation curves show that the proposed model gives larger errors in estimating small relative orientation differences than the VGG16 network (Figure 4.23-top) while on the other hand can estimate larger differences more accurately (Figure 4.23-bottom) compared to the VGG16 output. Due to this fact, as it can be seen in the absolute orientation curves, for some of the peaks of the trajectories, larger orientation errors are calculated for the VGG16 pre-trained network (Figure 4.21-green) in comparison to the estimations from the proposed model (Figure 4.21-blue). For the depth estimation component, the estimation values for the proposed depth estimation model are more noisy than the VGG16 pre-trained model, however the VGG16 pre-trained model has a bias towards lower values and does not estimated the higher values and gives a higher position error when estimating higher depth values (Figure 4.21).

4.7 Conclusions

This chapter investigated the issue of microrobot pose estimation using monocular microscope images in an Optical Tweezers setup. Two depth estimation methods for transparent, laser-driven microrobots were proposed using image sharpness measurements. A global and a local method of depth estimation of the transparent microstructure were described. These methods aim to derive an estimation for the sharpness model with respect to the overall z-translation of the object and depth changes of individual features of the microstructure. The calibration methods presented for both methodologies are object and lighting condition specific and need to be performed prior to the depth estimation routine. The combination of these two methods aims at distinguishing the cause of image sharpness variations. These variations can be attributed either to object translation along the microscope z-axis detected by the global approach or to 3D rotation detected by the local approach. Hence, the local method is capable of identifying which parts of the microstructure are in and out of focus in combination with the 3D estimated orientation. The global sharpness can be approximated by a sum of Gaussian curves for interfering features at different depths due to transparency. The local sharpness model is approximated by one Gaussian curve for distinct object features. The local method can reveal information about the object orientation and can be potentially combined with the model-based approach to estimate 3D orientation. By combining the two methods, the framework can account either for errors that occur from the template matching or the local depth estimation.

Section 4.4 presented a supervised learning approach for depth estimation of optically transparent microrobots using gray-scale monocular images generated in an Optical Tweezers setup. The motivation to use a state-of-the-art machine learning method is to learn a regression model for depth estimation using microrobot specific information from monocular image sequences that show simultaneous microrobot 3D translation and rotation. A neural network with five convolutional layers for data-specific feature extraction followed by an LSTM cell is used for depth regression. The model was trained and tested using experimentally acquired images with ground truth data trajectories acquired in an Optical Tweezers setup. The dataset was generated from microscope images of 3D-printed microrobots translated along the z-axis in discrete orientations drawn from a random uniform distribution and in orientations that correspond to discretized 360^o rotations in order to span the configuration space sufficiently. The validation results showed that the implemented trained model can estimate continuous trajectories with submicron accuracy for the specific test set. The trained model is specific to the design of the microrobot which is subject to tracking. However, the object-specific dataset needs to be generated once and can be used for developing a pre-trained model for Optical Tweezers setups with the same imaging system.

Section 4.6 presented a methodology for 6-DoF pose estimation of optically transparent microrobots in an Optical Tweezers setup. The method uses supervised learning with CNNs to estimate the relative 3D orientation between the current and previous image frame and the corresponding depth for the current frame using single images. The 2D position is obtained using an edge detection-based method which is also necessary for pre-processing the input images to the network. The absolute 3D orientation of the microrobot is obtained by registering the virtual geometrical model with the image frame prior to estimation. The model was trained simultaneously for relative orientation and depth estimation using microscope image data of 3D-printed microrobots generated in an Optical Tweezers setup. The datasets contain data of three geometrical models on which the networks were trained and validated. It is noted that the accuracy of the relative estimation component depends on the range of relative differences in the orientation that are contained in the training set, hence, the training data needs to contain both small and large variations in relative orientations in order to estimate both sequential and non-sequential data. Other sources of occurring inaccuracies are that the learned feature maps depend on the geometrical model and that the absolute orientations are obtained by relative measurements and therefore there is an accumulative error. Last, the dataset could be extended for improved accuracy but we choose a medium-sized dataset so that the applicability of the method is not limited. The proposed model was compared to a VGG16 feature extaction component pre-trained on ImageNet modified for pose estimation regression. The comparison demonstrated that the proposed model can give more noisy estimations on small orientation differences but also more accurate estimations towards higher relative orientation differences. The depth estimation component could be improved to include time-series estimation by replacing the fully connected layers with LSTMs as in Section 4.4. Future improvements would be to extend the method to simultaneous pose estimation of multiple geometrical designs and to cell manipulation and to consider occluded or overlapping microrobots.

Chapter 5

Optical Manipulation of Microrobots

This chapter presents how manipulation of 3D optical microrobots is achieved in an open-loop and shared control manner. In particular, Section 5.1 demonstrates how the microrobots presented in Section 3.2.2 are used for indirect optical manipulation of microobjects and potentially for cells. In Section 5.2, a control strategy that utilizes user's gaze information is developed for simultaneous multiple microrobot manipulation integrating haptic guidance. Hand-eye coordination can be facilitated by using the concept of perceptual docking [130]. This concept incorporates human sensory information, such as the eye gaze, to the human-machine interface to assist the operator in task execution. Such interfaces have been developed for macroscale surgical robotic systems. Microrobotic systems could benefit from similar implementations that assist hand-eye coordination in multiple microrobot or 3D microrobot manipulation, especially in platforms such as the Optical Tweezers which

---

Contents from this chapter have been published in: **Gaze contingent control for optical micromanipulation**, M. Grammatikopoulou and G-Z. Yang, In: 2017 IEEE International Conference on Robotics and Automation (ICRA) ©2017 IEEE allow multiple object manipulation by generating a pattern of optical traps. The incorporation of a haptic guidance interface in the microscale could also be beneficial since it enhances ergonomics for ease of manipulation. As eye gaze provides very fast saccadic movements, this information is be used for object targetting and optical trap placement that is performed seamlessly without interrupting the manipulation task by identifying regions of interest to the operator. The framework aims to assist the operator seamlessly in hand-eye coordination. The effectiveness of the developed control scheme is evaluated through two sets of experiments; in multiple object manipulation using 2D visual servoing and in 3D structure manipulation. The results of these experiments demonstrate that the execution time and the manipulation flexibility are improved when using the gaze controller.

5.1 Indirect Manipulation using Laser-driven Microrobots

Previous research has proposed methods on manipulating microobjects, such as microspheres, or cells using microrobots as grasping mechanisms [131]. In this section, indirect manipulation of a microsphere is demonstrated using two of the rotational joints of Section 3.3 for grasping. The performed experiment aims at demonstrating how indirect manipulation of microstructures, and potentially cells, with size up to a few tens of μm, can be achieved using mechanisms that are capable out-of-plane motion.

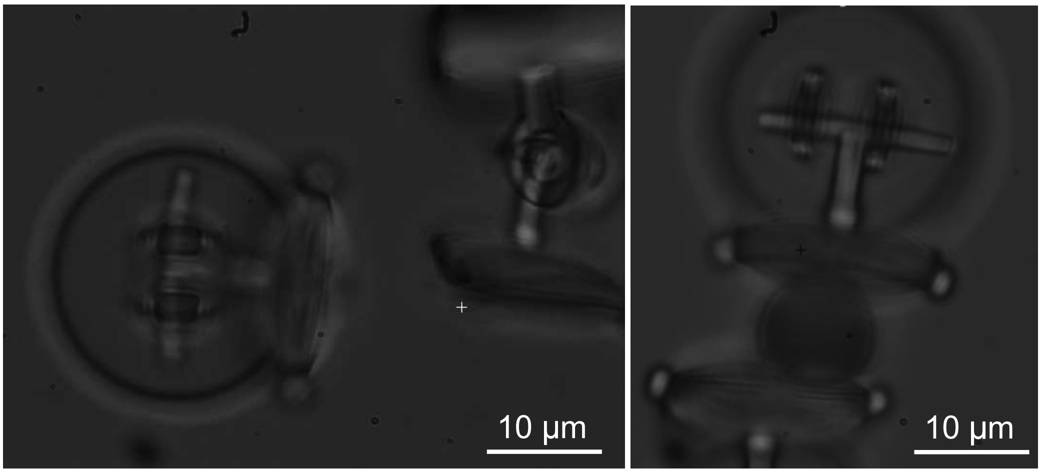

Figure 5.1: A view of two rotational joints used for indirect grasping inside an Optical Tweezers setup (left). The two microrobots grasping an 8 μm microsphere (right)

5.1.1 Experimental Setup and Discussion

An array of rotational joint microrobots and 8 μm microspheres is fabricated as described in Section 3.2. The microstructures are detached from the glass substrate using the sonication method as explained in Section 3.4. The glass slide containing the microrobots and the microspheres is placed inside the Optical Tweezers (Elliot Scientific, UK). The aim is use two rotational joint microrobots as grasping mechanisms to displace a microsphere along the z-axis. A fully and a partially detached rotational joint microrobot are used for manipulation in order to demonstrate out-of-plane motion of a microsphere (Figure 5.1). The laser power of the optical trap was set to 0.2 W. Figure 5.2 shows the displacement of the microsphere using two microrobots for grasping. A single laser trap is used to induce the optical force which is pushing the rotational part of the joint downwards. Due to the geometry of the rotational part, it is pushed downwards rather than trapped by the optical trap. A sequence of a microsphere grasped by the two microrobots and moved

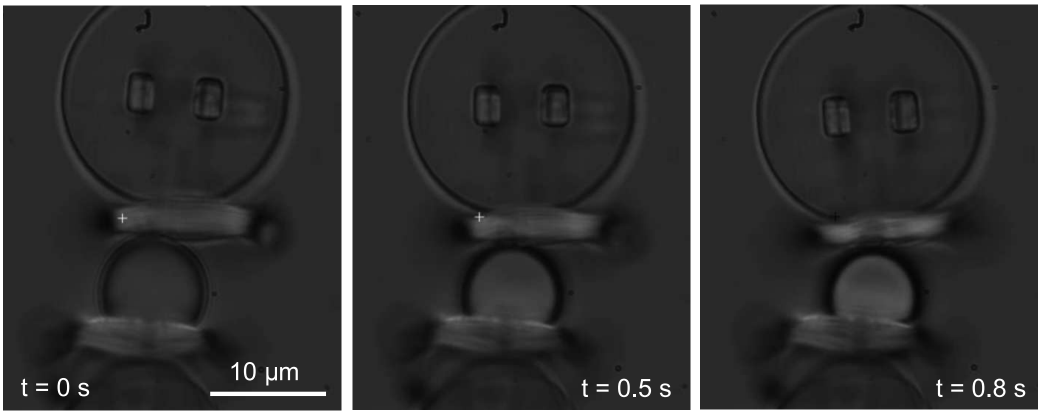

Figure 5.2: Downwards displacement of microsphere using single optical trap actuation of the fully detached rotational joint

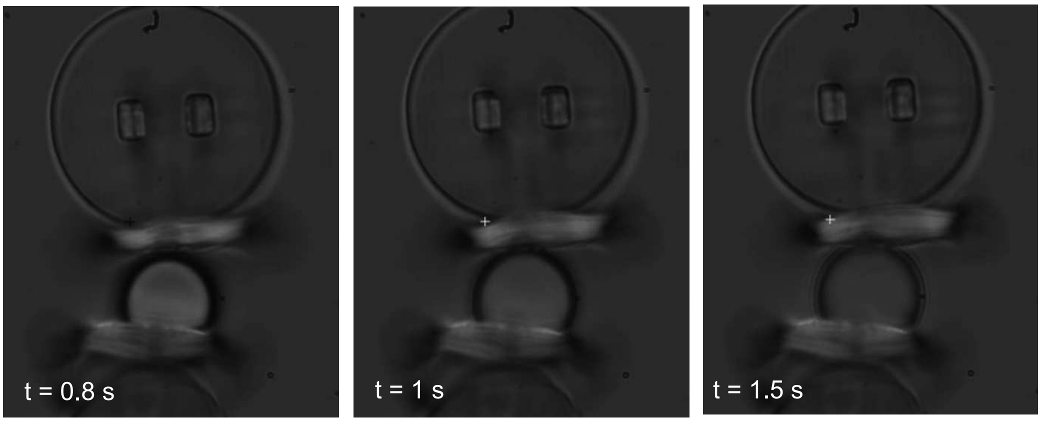

Figure 5.3: Upwards displacement of microsphere using single optical trap actuation of the fully detached rotational joint

downwards is shown in Figure 5.2. As the mobile part of the joint is pushed rather than grasped, the laser trap is switched on and off in order to move the microsphere downwards. When the optical trap is off, then the rotating part and the microsphere move upwards (Figure 5.3). It is worth noting that the microsphere appeared to be slipping at some instances while been grasped by the two microrobots. This could be because of insufficient grasping force applied by the two microrobots on the microsphere. A solution to this is to grasp the microrobots with multiple optical traps so that the normal grasping force on the microsphere is increased. By increasing the normal grasping force applied to the object, sliding of the object with respect to the grasping surfaces could be avoided. This however requires adding more handles to the microstructure to enhance the microrobot's manipulation capabilities. In addition, sliding could be avoiding if the rotating parts of the microrobots had deformable rather than rigid surfaces to grasp the microobject. This would also increase the tangential to the microobject grasping force, and hence, the overall grasping force.

5.2 Gaze Contingent Control for Optical Micromanipulation

The previous experiment highlighted the need of using multiple optical traps for manipulation, especially for manipulation of multiple microrobots and 3D microrobots. To this end, a human-robot interaction interface integrating the user's gaze information is developed to facilitate micromanipulation tasks. The work presented in this section describes: i) How object trapping and transportation are realized when taking into account the user's intentions during manipulation. This is performed transparently by processing the natural gaze of the user. In particular, the gaze information is combined with visual tracking to assist trapping and pattern reconfiguration without interrupting the executed task or compromising the number of objects to be manipulated and ii) how the operator can activate haptic guidance generated by the eye fixation point to position the assembled parts. The system aims to assist the operator seamlessly in hand-eye coordination. The effectiveness of the developed control scheme was evaluated through two sets of experiments; in multiple object manipulation using 2D visual tracking and in 3D structure manipulation. In the first set of experiments, the gaze controller is compared to the standard Optical Tweezers user interface. The results of these experiments demonstrate that the execution time and the manipulation flexibility are improved when using the gaze controller. The second experiment shows how 3D control can be performed using gaze assistance.

5.2.1 System Overview

The operator controls the laser traps via two haptic devices. The microscope-camera feed is displayed to the user with the optical trap positions overlaid on the image. The software controller operates in different states according to the phase of the task. Seamless state switching is realized based on the operator's intention and human sensory input. The user initially controls one laser point with each of the haptic devices and can add more laser traps on demand during the manipulation task. Hence, the operator can manipulate multiple spots with each one of the haptic devices. The laser positions are added according to the eye gaze input and the visual tracking either directly on the identified objects or on the eye fixation point on the respective frame. The positions of the added optical traps can be later adjusted using the eye tracking data. The user can selectively activate a guidance force that helps in microparts positioning.

5.2.2 Gaze Contingent Controller

The aim of the presented control scheme is to enhance the operator's dexterity in tasks that require handling of multiple microparts or complex structures in a dynamic environment.

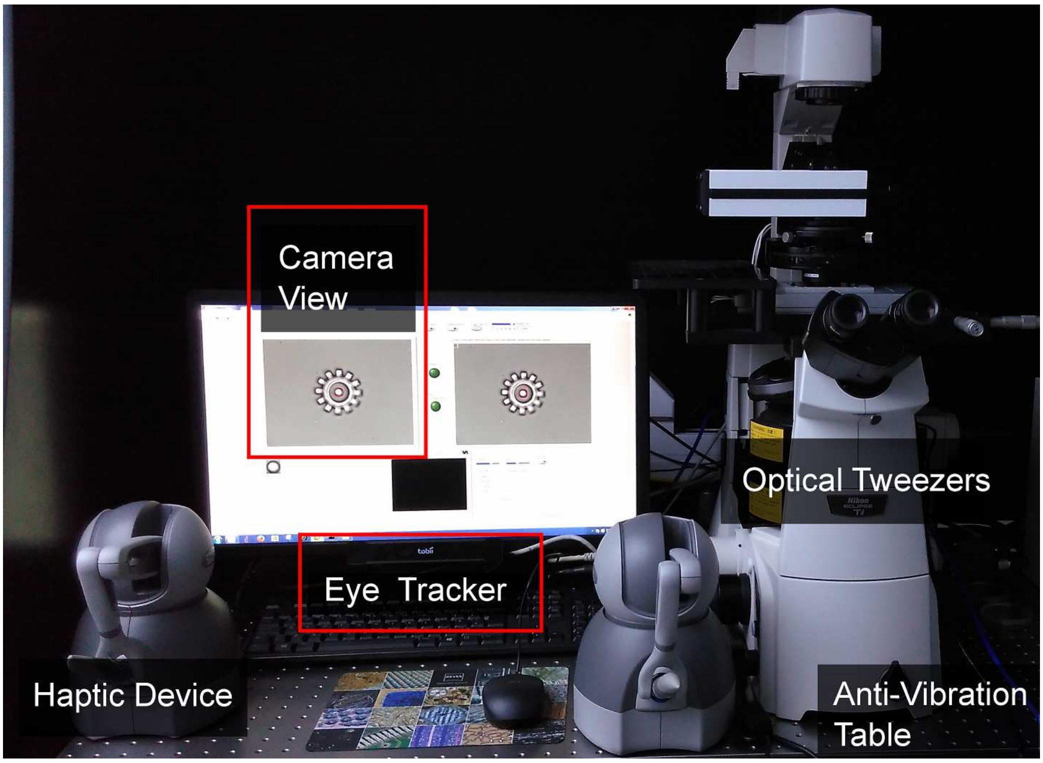

Figure 5.4: The system hardware components: The haptic devices, the eye tracking device, the computer screen displaying the live camera feed and the Optical Tweezers (from left to right).

5.2.2.1 Eye Gaze Data Processing

The operator's eye gaze is tracked by the device using infra-red video with a measurement rate of 60 Hz. Eye gaze processing is performed continuously in a separate thread regardless of gaze data utilization. A buffer of previous values is kept while the noisy values are discarded. Noisy values include measurements that correspond to the operator blinking or detection of only one eye. The 2D eye gaze is filtered with a low pass filter. The camera provides an 648 x 488 image with each pixel corresponding to 0.074 μm, therefore the visible workspace is 48 x 36 μm. The view covers partially the computer screen and the Graphical User Interface. Hence, only the filtered

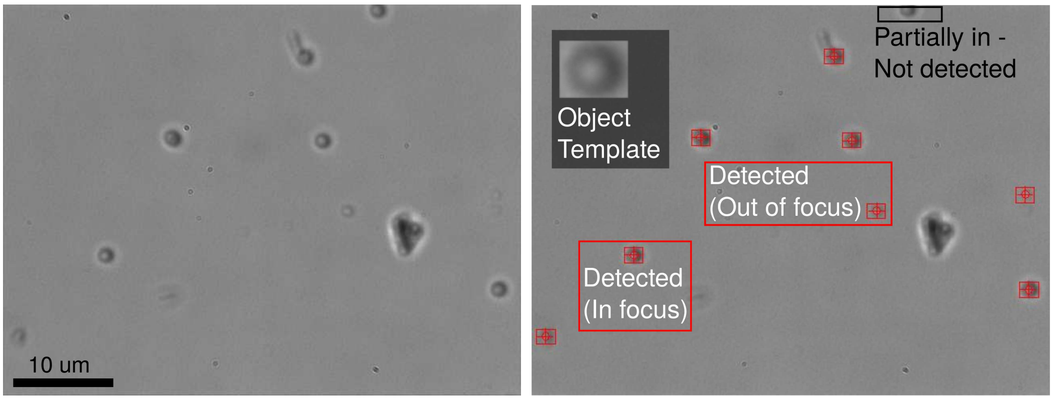

(a) The camera feed as viewed by the user (b) The detected objects (red) and object template

Figure 5.5: The original and processed camera feeds

data points which are within this region of the screen are used in the software controller. In case the user eye gaze is outside of this region, the latest position within the camera image which is kept in the buffer is used in the calculations. Consequently, the operator does not need to continuously look at the camera feed.

5.2.2.2 Intention Recognition and Gaze Control

The software controller has three different states: i) Trap pattern generation for object trapping; ii) optical trap repositioning and iii) haptic guidance for object placement. A new optical trap is added or re-positioned only after user request allowing the primary control to the operator at all times. The processed eye gaze information is used to determine the intentions of the operator and can be identified by addressing the following three questions.

If the user is exploring or has focused on a specific region of the workspace: This user activity is determined by calculating the Candidate Target Position (CTP) which gives an indication of the respective region of interest. To obtain the CTP, the standard deviation of the buffer filtered gaze positions is calculated. The mean value of the sample is set as the CTP if the standard deviation is sufficiently small. The threshold varies according to the desired precision. A threshold of 20 pixels that corresponds to eye gaze being focused at a region with radius of 1.48 μm of the actual workspace was used in the presented setup. This threshold was selected experimentally because it allows consistent targeting of the microspheres. Meanwhile, it is not obstructive to the natural gaze of the user since it does not require the gaze to be focused at a very restricted workspace. It is also worth noting that the standard deviation of the eye gaze data depends on the velocity of the object that the user is trying to follow. For instance, for small particles where the Brownian motion is considerable, the standard deviation will be larger than in the case of a more static object. Hence, the tolerance threshold is adjusted accordingly. The number of past fixation points also determines the update rate of the CTP. In this implementation, a buffer of 50 previous positions was used because it was compliant with the natural gaze in most experiments and was sufficient to identify the regions of interest. In particular, 50 previous positions with an update rate of 60 Hz corresponds to identifying the region of interest within a time period of 0.83 s. Hence, this update rate can provide a consistent position when the user has focused on a specific region for more than 0.83 s allowing to follow both the exploration phase and the target selection phase. However, for different users and desired precision, the parameter can be adjusted accordingly.

Where the new optical trap should be placed: The new optical traps are added on demand using the eye tracking data and the output of the visual tracking algorithm. The trap can be either placed directly on the detected object which is closest to the operator's fixation point or on the last identified CTP in case there is no object in the area around the CTP. In the first case, the user does not need to physically move the trap to the desired object. It also facilitates more consistent object handling when larger 3D structures are manipulated in terms of adjusting the object position and orientation. Generating a trap on a CTP aims to compensate for visual tracking inconsistencies when the objects are not detected and also add a trap at a different position on the object rather than its contour centroid. Once the laser trap is added, it maintains its relative position to the previously added laser traps.

In order to assist the user in translating the points simultaneously in a more intuitive manner, the centre of the convex hull of the generated laser trap pattern is translated by the haptic device. Let $\mathbf{p}_{ki}, i = 1, .., k$ and $k = L, R$ be a trap that belongs to the left $(k = L)$ and right $(k = R)$ group of points respectively where N_k the total number of traps of the k_{th} pattern. By the terms left and right group we refer to the number of points that are manipulated by the left and right haptic device respectively. Therefore, the centre $\mathbf{c_k}$ of the convex hull C_k of each pattern is given by:

$$\mathbf{c_k} = \frac{\sum \mathbf{x}_i}{N_{C_k}}, \quad \mathbf{x}_i \in C_k,\ i = 1, ..., N_{C_k} \tag{5.1}$$

$$C_k = \left\{ \sum_{j=1}^{N_k} \alpha_j \mathbf{p}_{k_j} \middle| (\forall i : \alpha_j \geq 0) \wedge \sum_{j=1}^{N_k} \alpha_j = 1 \right\} \tag{5.2}$$

with $\mathbf{p}_{ki}, \mathbf{c_k}, \mathbf{x}_i \in \mathbb{R}^2$.

How to rearrange the optical trap configuration while maintaining the grasp by the remaining traps: During object transportation, the relative position among the traps of a pattern remains fixed. However, the position of an individual trap may be adjusted in order to rearrange the trapped objects or to change the pose of a 3D object. The trap reconfiguration is realized as follows; The desired laser trap is selected as the closest trap to the CTP and cannot be deselected until the trap reconfiguration is terminated. This

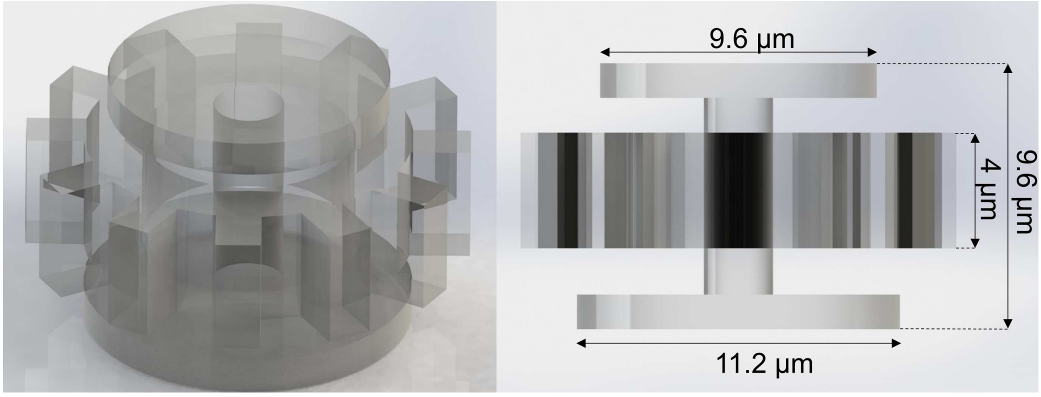

Figure 5.6: Geometrical model of the microstructure used in the second experiment

serves the purpose of allowing the user to explore the adjacent region and not requiring the gaze to continuously follow the selected trap. Since the operator is manipulating a set of traps with the haptic devices, the motion of one of the haptic devices has to be decoupled from this pattern and coupled to the trap to be repositioned. Hence, during the optical trap reconfiguration, the pattern that belongs to the respective haptic device maintains its position and the second haptic device controls the target trap. At the end of the reconfiguration state, the second haptic device is coupled again with the respective laser point pattern.

5.2.2.3 Gaze Contingent Guidance Constraints

In order to assist the user in placing the assembled microparts with respect to the pattern's centre, a guidance force is activated on demand to guide the operator to the desired position. The target position $\mathbf{p_d}$ is defined as the CTP and is not updated until this position is reached. This is to avoid instabilities in the force profile caused by rapid switching when target positions are close.

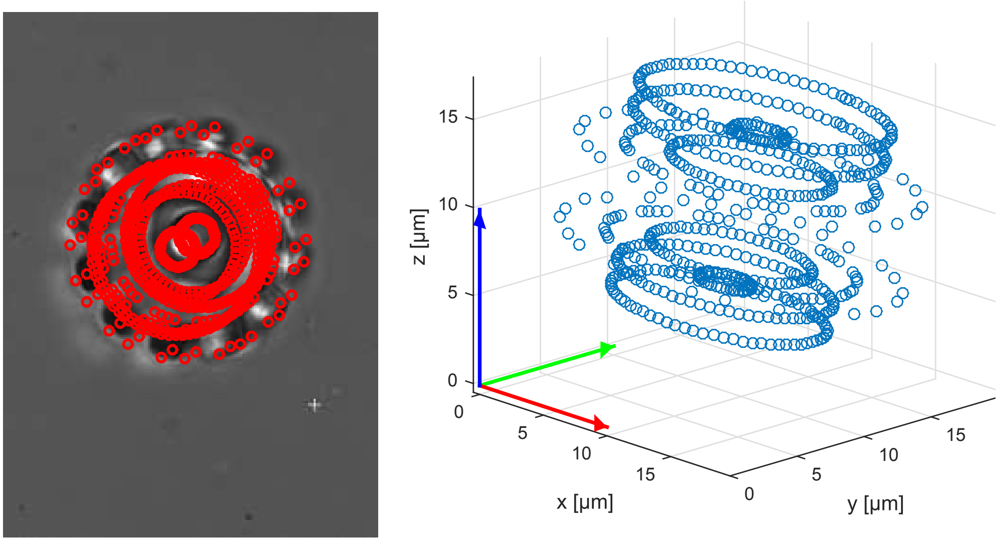

Figure 5.7: Registered projection of geometrical model (left) and initial pose with respect to global frame (right)

The guidance force, as defined in [132], is given by:

$$\mathbf{F_p} = \begin{cases} 0 & \text{if} \;\; d \geq d_{max} \\ f_A \;\mathbf{n} & \text{if} \;\; d_{max} > d > d_{high} \end{cases} \tag{5.3}$$

where

$$f_A = k_0 \;\|\mathbf{p_t}\|^2 \;(\|\mathbf{p_t}\| - d_{max})^2 \; e^{k_1 \;\|\mathbf{p_t}\|} \tag{5.4}$$

$$\mathbf{p_t} = \mathbf{p_d} - \mathbf{c_k} \tag{5.5}$$

$$\mathbf{n} = \frac{\mathbf{p_t}}{\|\mathbf{p_t}\|} \tag{5.6}$$

with k_0, k_1 two scalar values, $\mathbf{p_d}$ the target position, d_{max} the distance between $\mathbf{c_k}$ and the target $\mathbf{p_d}$ at which the guidance force starts to increase, d_{high} the distance between $\mathbf{c_k}$ and the target $\mathbf{p_d}$ at which the maximum force is rendered and $\mathbf{n}$ the direction towards the target.

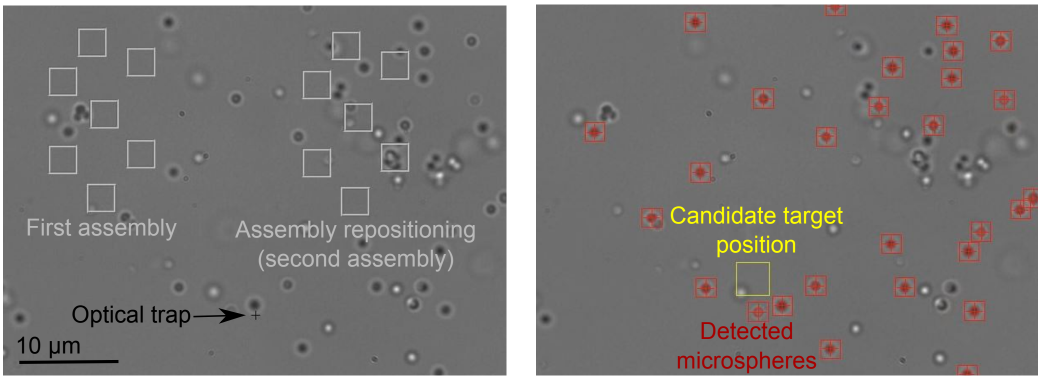

Figure 5.8: The operator view during the performed experiments (left). The processed image feed displaying the detected microspheres (red) and the candidate target position as calculated from the operator's gaze (right)

5.2.3 2D Position Detection

5.2.3.1 Template Matching for Spherical Object Tracking

Real-time image processing is performed in order to obtain the 2D position of the microstructures within the visible workspace. For spherical objects, a template matching algorithm is used for object detection since they maintain a relatively constant appearance in all orientations. The user can define the template according to the object that needs to be tracked. In the performed experiments the processing time varies from 1 to 3 ms. In Fig 5.5, the live camera feed is shown as displayed to user (Figure 5.5 (left)). The detected microspheres (size of 1 μm) are shown in Figure 5.5 (right). The minimum matching score is set accordingly in order to identify objects which are moving sufficiently close to the focus plane. However, these features can be adjusted by defining an alternative matching template and similarity score. This method of detection is more robust to noise in the case of small spherical objects where Brownian motion is evident, although it is not particularly effective for overlapping objects. An alternative tracking strategy is implemented for larger non-spherical objects which have different appearance depending on their orientation in the 3D space.

5.2.3.2 Non-spherical Object Tracking

The object boundary is obtained by the following sequence. First, canny edge detection is performed followed by discarding all objects with a small number of pixels in order to reject noise. Then, the boundary is thickened so that a closed boundary is obtained. For convex-shaped objects, the convex hull of the edges is considered as the boundary to ensure closed contours for increased detection robustness. This is sufficient for applications where a closed boundary is more important than an accurate contour around the object. Contour filling and image segmentation is performed to locate the object of interest. The filled contour is used for template matching in 3D orientation estimation, as described in the next section.

5.2.4 Experimental Setup

The system consists of a master and a slave component (Figure 5.4). The master component includes two haptic devices (Geomagic, USA) and an eye tracking device (Tobii Technologies AB, Sweden) that tracks the operator's eye gaze. The haptic devices control the position of the laser traps while the data from the eye tracker is used to determine the user's intentions and define the operating states of the software controller as described in Section 5.2.2.2. The slave part is the Optical Tweezers (Elliot Scientific, UK). The Optical Tweezers system consists of a 1070 nm fiber laser with variable output power (Ytterbium Fiber Laser, IPG Photonics, USA), an optical microscope with an oil immersion objective lens (Nikon Ti) and a high frame rate CCD camera (Basler AG, Germany). The laser traps are placed within the workspace by direct laser actuation while multiple traps are generated through time multiplexing.

5.2.4.1 Microrobot Fabrication

The object used in the conducted experiment is a gear-shaped microrobot with radius of 8 μm and height of 9.6 μm. The CAD model with the respective dimensions are shown in Figure 5.6. An array of microstructures were printed on the glass substrate using the Nanoscribe 3D-printer (Nanoscribe, Germany) and IP-L photoresist (Nanoscribe, Germany). A set of mechanical micromanipulators (Imina Technologies, Switzerland) was used to detach the printed microstructures from the glass surface. The detached objects were placed in a solution of deionized water.

5.2.5 Experimental Results

Two sets of experiments are presented demonstrating the functionality of the proposed framework. The first set of experiments compares the performance of the gaze contingent controller to the standard Optical Tweezers control interface. The second experiment demonstrates non-spherical object manipulation using the gaze contingent framework in conjunction with the template-based method for 3D orientation estimation of Section 4.5.1 to recover the orientation of the microstructure.

5.2.5.1 Gaze Contingent Controller Performance Assessment in Microassembly with 2D Visual Tracking

The effectiveness of the gaze control scheme was evaluated through a set of user experiments comparing the execution time, the manipulation flexibility and repeatability of the task when the gaze controller and the standard user

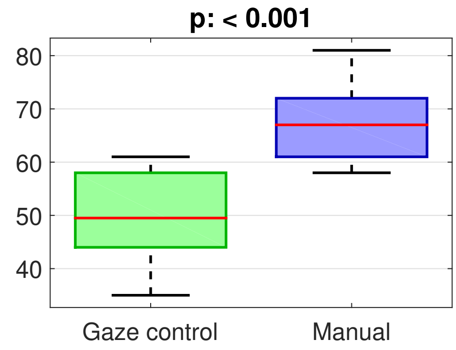

Figure 5.9: Duration for first assembly [s]

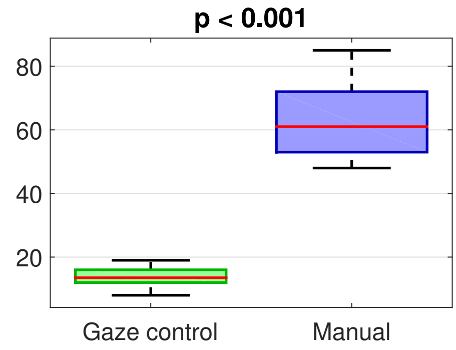

Figure 5.10: Duration for second assembly [s]

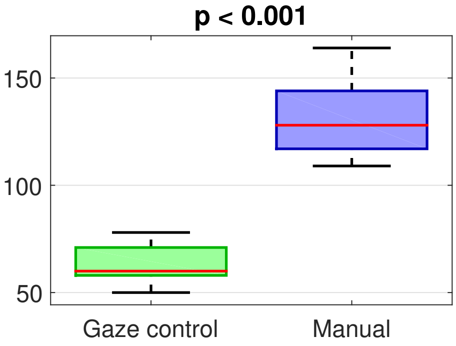

Figure 5.11: Total duration for task [s]

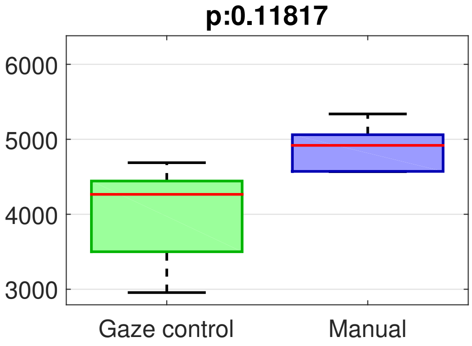

Figure 5.12: Distance over time [μm s]

interface for the Optical Tweezers are used. The standard user interface uses the mouse as an input device and does not allow the formation and transportation of an arbitrary object configuration. The task was to assemble 7 microspheres in a specific configuration and then move the assembly at a different position. The desired assembly positions were overlaid on the displayed image (Figure 5.8). The purpose of the task was to demonstrate how multiple small sized microstructures can be assembled in an arbitrary configuration using the gaze controller. The laser power was set to 0.2 W. The task was repeated 10 times with the gaze contingent control scheme and 10 times with the mouse interface. The user was familiar with both

Metric		**Gaze**	**Manual**	**p-value**
First assembly	[s]	49.8	67.7	< 0.001
Second assembly	[s]	13.8	63.3	< 0.001
Total time	[s]	63.6	131	< 0.001
Distance over time	[mm s]	4.19	4.75	0.118

Table 5.1: Mean values and p-values of metrics for microassembly user experiment

modes of operation prior to performing the experiment. The 20 experiments were performed interchangeably; once with the gaze controller and once with the mouse control so that the two consequent attempts are performed under comparable experimental conditions. The guidance force was activated at a distance $d_{max} = 6$ μm from the CTP with maximum force rendered at $d_{high} = 3$ μm. The distances were chosen so that guidance is activated sufficiently close to the CTP. The maximum guidance force was set to 0.8 N to provide soft haptic guidance. Guidance was only activated for the second stage of the experiment.

5.2.5.2 Results and Discussion

The aim of the repeated experiment is to demonstrate that the execution time of the individual assemblies and overall task as well as the total travelled distance of the laser traps are consistently reduced when using the eye tracking interface. Therefore, the metrics that are used for performance assessment are the time to perform the first assembly, the time for the second assembly (reposition the assembly or repeat the assembly at the desired position), the total execution time of the task and the cumulative distance over time, i.e. the sum of all integrals of the distance covered by each laser trap with respect to time. The means and p-values of the metrics are given in

Table 5.1. The p-values were calculated using the Two-sample *t*-test. The results demonstrate that the execution time is significantly reduced in both subtasks and overall task (Figure 5.9 - 5.11) while the distance over time metric also shows reduced travelled distance throughout the repeated experiments (Figure 5.12). The reduced travelled distance suggests that placing the trap directly on the desired object improves the manipulation efficiency compared to the manual case where the trap is placed arbitrarily and has to be physically moved towards the target object. In addition, the synergy of eye tracking and visual tracking compensates for inconsistent object tracking due to the Brownian motion since at that case the trap will be place on the CTP. Similarly, visual tracking allows the user to interact seamlessly since the optical trap is positioned on the tracked object which is closer to the CTP, disregarding the need of unnatural user interaction with the system.

5.2.5.3 Manipulation of a 3D Microrobot and Template-based Orientation Estimation

In the second experiment, a gear-shaped microrobot is manipulated using the gaze contingent controller. The laser power was set to 400 mW during the experiment. An increase of the laser power is required compared to the previous experiment due to the larger dimensions of the microstructure. The task was to demonstrate how 3D rotation can be performed using the gaze controller while the achieved pose is estimated for each trapping configuration. The proposed orientation estimation algorithm complements the gaze controller by assisting the user's perception in understanding the force dynamics and kinematic properties of the object. It can be seen that the relative trap positioning affects the object orientation due to its geometry. These orientation are not evident when manipulating spherical objects hence

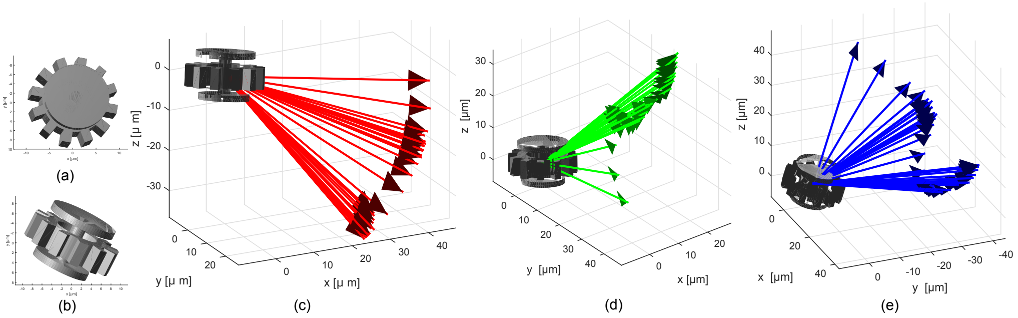

Figure 5.13: (a) Initial orientation of microrobot with respect to global frame as viewed from the XY plane (b) Final orientation of microrobot with respect to global frame as viewed from the XY plane (c) Trajectory of x-axis of object frame (d) Trajectory of y-axis of object frame (e) Trajectory of z-axis of object frame

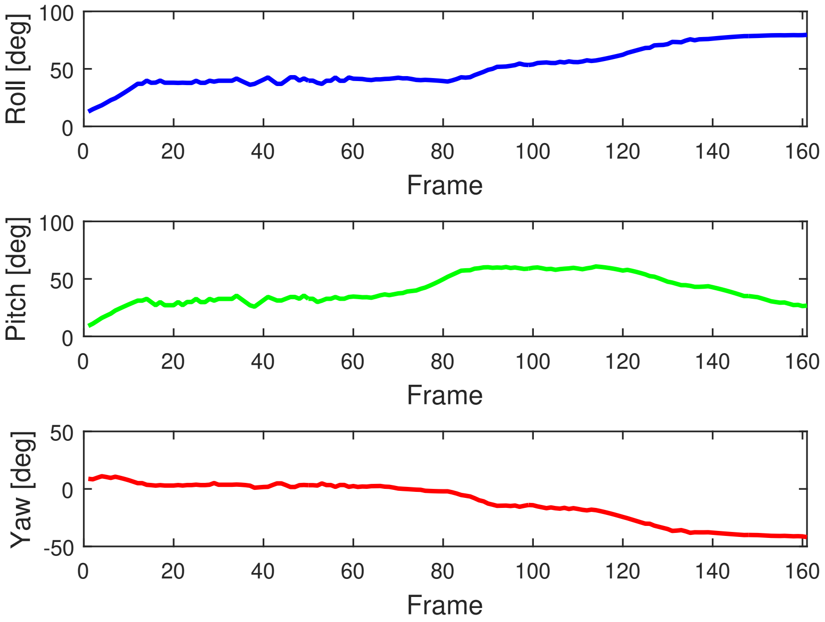

Figure 5.14: Rotation angles of the z,y and x axis of the object frame (θ_z, θ_y and θ_x) with respect to global frame

it is not necessary to recover the sphere's orientation.

5.2.5.4 Results and Discussion

The results show the estimated orientation when the microstructure is rotating simultaneously about all three axis. The total time that was required for the object to rotate was 16.6 s. The initial orientation $\hat{R}_o$ and translation $\hat{\mathbf{t}}_\mathbf{o}$ given by equation (4.2) are equal to:

$$\hat{R}_o = \begin{bmatrix} -0.9849 & -0.1377 & 0.1055 \\ 0.1554 & -0.9706 & 0.1838 \\ 0.0771 & 0.1975 & 0.9773 \end{bmatrix}, \ \hat{\mathbf{t}}_\mathbf{o} = \begin{bmatrix} 0.4183 \\ 0.4051 \\ 0 \end{bmatrix} \tag{5.7}$$

and the trajectory can be seen in Figure 5.14. The initial and final orientation of the microrobot as well as the recovered orientation trajectory are shown in Figure 5.13. Figure 5.13c-e depict the individual trajectories of the x,y and z axis of the object frame during the performed experiment. The object coordinate frame origin is attached to centre of mass of the object. The consequent orientations depicted in this figure are downsampled for illustration purposes. The proposed algorithm does not depend on feature tracking and the geometry of the structure. It also provides a good estimate in case the 3D-printed object is different from the CAD model (Figure 5.13).

5.3 Conclusions

This chapter discussed optical micromanipulation of microrobots for indirect and shared control manipulation. Section 5.1 demonstrated how indirect manipulation of microobjects can be performed using 3D multiple component microrobots as grasping mechanisms. It was demonstrated that the multiple component mechanism could induce out-of-plane motion to the grasped object. Sliding of the microobject while been grasped was observed. Sliding could potentially be avoided by increasing the grasping force applied to the object. This could be achieved by adding more grasping handles to the multiple component mechanism allowing for it to be grasped by multiple optical traps more stably and transfer that force to the object, or making the grasping surfaces more deformable rather than rigid. This experiment highlighted the fact that multiple optical traps are needed in order to manipulate 3D geometries stably. Section 5.2 proposed a gaze contingent control framework for optical micromanipulation of multiple and 3D microrobots. The developed controller allows the operator to add and reposition the optical traps interactively using the eye gaze combined with real time 2D visual tracking. The synergy of the eye gaze and visual tracking aims to identify the objects of interest, to compensate for object tracking inconsistencies and to provide seamless in micromanipulation without interrupting task execution. Haptic guidance is provided to the user to achieve more consistent object transportation. The capabilities of the proposed design are assessed through two sets of experiments; one in multiple microsphere 2D manipulation and a second one in 3D object manipulation. The user experiments for the first task shows that task execution is faster and hand-eye coordination is improved in comparison to the standard control Optical Tweezers mode.

Chapter 6

Hybrid Optical and Magnetic Microrobots for Reconfigurable Microassembly

This chapter presents a system of hybrid optical and magnetic microrobots for reconfigurable microassembly. It describes the assembly of microrobots in a kinematic chain of spherical joints using the magnetic field inside an Optical Tweezers setup with a customized integrated magnetic coil setup. This setup allows simultaneous microrobot actuation using the Optical Tweezers and the magnetic field. The aim of the proposed methodology is to exploit the fine resolution and precision of Optical Tweezers in position regulation while using the attractive magnetic force between the components to form the assembly. This approach allows *in situ* and reconfigurable microassembly of three-dimensional mechanisms instead of fabricating and delivering specific microrobot designs prior to manipulation. The magnetic field is used to magnetize the components and generate the attractive force that maintains the assembly of the components. It is demonstrated that the forces applied by the Optical Tweezers are sufficient to disassemble the components without decreasing or disabling the magnetic field, hence while the individual components maintain their magnetization. It is also shown that the attachment and detachment of the components can be reversible. An estimation for the range of the assembly displacement force and the component detachment force, derived from the performed experiments are also discussed.

The structure of this chapter is the following: Section 6.1 states the motivation for the proposed approach followed by the description of the design of the basic structural components in Section 6.2. The stages that comprise the microassembly and disassembly strategy using hybrid optical and magnetic actuation are described in Section 6.3. A model describing the system dynamics is presented in Section 6.4 while the system identification methods used to estimate the system's parameters are presented in Section 6.5. The experimental setup of the Optical Tweezers with the integrated magnetic coils is presented in Section 6.6. An experimental demonstration of the microassembly and disassembly strategy with force measurements using the derived system dynamics is presented in 6.7 while the results are discussed in Section 6.8.

6.1 Reconfigurable Microassembly

The concept is to assemble a kinematic chain using the magnetic field from fabricated components of basic geometries that represent the links of the chain. The motivation is that the magnetic force would be sufficient to hold the assembly together and that the adhesion contact force is sufficiently small so that 3D rotation of the link would not be obstructed by adhesion. Ideally, the contact force should generate rolling motion between the component so

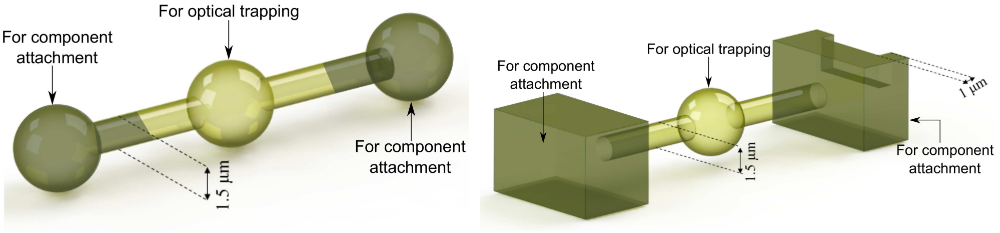

(a) Cylinder with spherical handles and tips (b) Cylinder with spherical handles and rectangular tips

Figure 6.1: Rendering of the CAD models of assembly components

that the assembly is stable and representing a kinematic chain of rigid bodies. In addition, using the magnetic force as the assembly force would allow for disassembly and reconfigurable kinematic chains. The individual components which are used for the assembly are described in the following section.

6.2 Component Design and Fabrication

Each assembly consists of two fundamental structural components. The first one is a cylindrical microstructure with a spherical handle and spherical tips while the second is a cylindrical microstructure with a spherical handle and two rectangles at each tip of the cylinder. The designs and their corresponding dimensions are given in Figure 6.1a and 6.1b. For both geometries, the middle sphere is used as a handle for the optical trap (Figure 6.1). The metal deposited tips are used for other components to be attached on. For the first or last link of the assembly, as only one tip is used as part of the spherical joint, the second tip could be used for actuation by the optical trap to induce a vertical force along the z-axis by pushing the metal-coated tip downwards. For the second geometry (Figure 6.1b), the rectangular tips are used only as part of the spherical joint using the flat surfaces of the rectangles as attachment surfaces. As mentioned, the trapping force is used to grasp and position the components while the magnetic field is used to magnetize the nickel layer and induce the magnetic force which assembles the two components in a spherical revolute joint. The components are fabricated following the procedure presented in Section 3.3. Both geometries of microstructures are printed in an array with the masks to achieve selective metal deposition. The sputtering method is used to deposit a 100 nm layer of nickel on the microstructure array. The microstructures and the masks are detached from the glass substrate using sonication for batch detachment.

6.3 Microassembly Stages and Strategy

This section describes the steps of reconfigurable microassembly using hybrid optical and magnetic microrobots. The stages are: i) assembling two components together by bringing them close using the Optical Tweezers and activating the magnetic field to magnetize the ferromagnetic surfaces and ii) disassembling two components while the magnetic field is still active. The main functions of the assembly, which are translation of the kinematic chain and joint rotation, are also described. The sequence of all the above stages is described as follows: i) Assembly of the kinematic chain, ii) displacement of the assembly and joint rotation in 2D and 3D and iii) joint disassembly under active magnetic field.

6.3.1 Assembly of Spherical Joint using the Magnetic Field

The ferromagnetic surface on the microrobot needs to be magnetized in order to align the components and induce the attractive force between them. The magnetization is induced by an homogenous magnetic field created by an

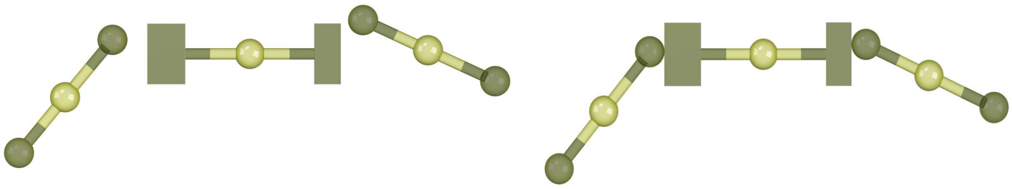

(a) (b)

Figure 6.2: Components before and after they are assembled under the magnetic field

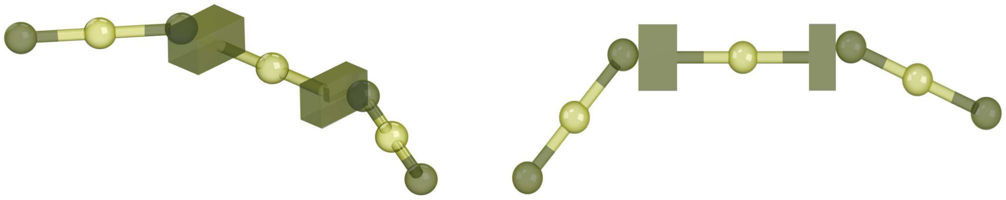

(a) (b)

Figure 6.3: 3D and 2D views of assembled kinematic chain under the magnetic field

Helmholtz coils configuration with an intensity of 10 mT. During assembly, the magnetic field is on and the optical trap is disabled. This is because the trapping force can be larger than the magnetic force depending on the laser power, hence obstructing component assembly. Figure 6.2 depicts a schematic of an example configuration of an assembly consisting of two cylindrical links with spherical tips and a link with rectangular tips. Figures 6.2a and 6.2b show a component configuration before and after the assembly under the magnetic field. The components need to be at a maximum distance of approximately 1 μm so that the two components can be attracted to each other. This distance was visually measured in the performed experiments.

6.3.2 Displacement of Assembly and Joint Rotation under the Magnetic Field using the Optical Tweezers

After the assembly has been formed, both the Optical Tweezers and the magnetic field are active. In the following analysis, it is assumed that the assembly is grasped by one optical trap, but more optical traps could be considered. The assembly of the components is maintained due to the magnetic forces between the components. For the links that act as the end-effectors of the assembly, the surface of the nickel-coated spherical tip can be used to induce a vertical force caused by the laser for out-of-plane displacement.

6.3.3 Disassembly of Spherical Joint under the Magnetic Field using the Optical Tweezers

The main feature of the proposed strategy is the possibility of reversible and reconfigurable assembly. In order to reconfigure the assembly and disassemble the components, the trapping force must overcome the contact force. This is performed while the magnetic field is on and the magnetization of the components is maintained. This is necessary so that partial reconfiguration of the assembly is possible and also to assess that the disassembly is reversible under the influence of the magnetic field and after the components come into contact. The kinematic chain can be completely disassembled by deactivating the magnetic field.

6.4 System Dynamics

This section presents the force modelling for different stages of the assembly. The main force components that describe the system dynamics are the trapping force, the fluid drag force, the thermal random force and the contact force which consists of the magnetic, adhesion and frictional force. This model is later used to measure the contact force between components for disassembly and for the displacement of a kinematic chain. The following section discuss each of the force components.

6.4.1 Optical Trapping Force

As mentioned in Section 2.5.1, the force model that describes the trapping force can be derived either by the ray-optics model or the electromagnetic model depending on the size of the trapped object and the wavelength of the laser. In the current model based on the geometry of the microstructures and the amplitude of the used laser power, it is assumed that the trapping radius R of the laser beam is small enough so that the laser beam interacts only with the spherical handle and not with the cylindrical part of the microstructure. Hence, the trapping force can be described by the spring model as the microrobots are grasped by the spherical handles. The spring model for the trapping force is given as follows:

$$\mathbf{F_{trap}} = \begin{cases} \mathbf{k}\ (\mathbf{u} - \mathbf{q}), & \text{if } \|\mathbf{u} - \mathbf{q}\| < R. \\ 0, & \text{otherwise.} \end{cases} \tag{6.1}$$

where $\mathbf{k} = [k_x\ k_y]^T$ the trapping stiffness along the x and y axis, $\mathbf{u} \in \mathbb{R}^2$ the position of the laser trap and $\mathbf{q} \in \mathbb{R}^2$ the position of the spherical handle which is also assumed to be the centre of mass of the microstructure.

6.4.2 Viscous Drag

The force balance of a body moving in a fluid is given by the Navier-Stokes equation:

$$-\nabla \mathbf{P_f} + \mu \nabla^2 \mathbf{v} + \rho \, g = \rho \frac{D\mathbf{v}}{Dt} \tag{6.2}$$

where $\mathbf{P_f}$ is the pressure of the fluid, μ the fluid viscosity, $\mathbf{v}$ the fluid velocity, g the gravitational acceleration and $\frac{D\mathbf{v}}{Dt}$ the material derivative of the fluid velocity. The above equation assumes that the fluid is continuous, incompressible, a Newtonian medium and does not account for Brownian motion. Equation (6.2) can be equivalently expressed as:

$$-\nabla \mathbf{P^*}_\mathbf{f} + \nabla^2 \mathbf{v} = Re \, \frac{D\mathbf{v}}{Dt} \tag{6.3}$$

$$Re = \frac{\rho v_\infty L_c}{\mu} \tag{6.4}$$

where v_∞ the characteristic fluid velocity and L_c the characteristic length, which describes the dimension of the object in the fluid. The fraction Re given in equation (6.4) is the Reynolds number and can be interpreted as the ratio of inertial to viscous forces. Therefore, it represents the relative significance of inertial and viscous forces. Low Reynolds number ($Re << 1$) indicate that viscous forces dominate over gravity and inertial forces. For low Reynolds numbers, equation (6.3) can be written as:

$$\nabla \mathbf{P_f} = \nabla^2 \mathbf{v} \tag{6.5}$$

which is also known as Stokes or creeping flow. This motion is equivalent to very slow motion in a high viscosity medium in the microscale.

As stated in [133], the viscous drag on any non-spherical shape in the microscale can be approximated by the drag force exerted on sphere of an equivalent radius. Using the Khan-Richardson approximation of the drag force on a sphere [134], the drag force and Reynolds number can be expressed as follows:

$$\mathbf{F_{drag}} = \frac{1}{2}\pi R^2 \|\mathbf{v}\|^2 C_D \frac{\mathbf{v}}{\|\mathbf{v}\|} \tag{6.6}$$

$$C_D = (1.84Re^{-0.31} + 0.293Re^{0.006})^{3.45} \tag{6.7}$$

$$Re = \frac{\rho \|\mathbf{v}\| R}{\mu} \tag{6.8}$$

for low to medium Reynolds numbers, $Re \in (0, 10^5)$, where C_D the drag coefficient of the sphere. The expression for the drag force can be further simplified for the case of low Reynolds numbers as in [135]:

$$\mathbf{F_{drag}} = -6\pi\mu R\mathbf{v} \tag{6.9}$$

$$C_D = 6\pi\mu R \tag{6.10}$$

with C_D the drag coefficient of a sphere. In the general case, the drag force in low Reynolds numbers is given by:

$$\mathbf{F_{drag}} = -\mathbf{C_D}\,\dot{\mathbf{q}} \tag{6.11}$$

where $\mathbf{C_D} = [C_{Dx}\ C_{Dy}]$ the drag coefficient along the x and y-axis, and $\dot{\mathbf{q}} = \mathbf{v} = \frac{d\mathbf{q}}{dt}$. In this work, the viscous drag force is modelled as in (6.11) with $\mathbf{C_D}$ treated as a vector in the general case of a non-spherical microobject rather than assigning an equivalent radius to get the drag coefficient and is estimated experimentally as described in Section 6.5.2.

6.4.3 Thermal Force

For micron-sized particles moving in a fluid with similar density as the particle, there is an additional component of motion due to collisions of the atoms of the fluid with the particle. This motion is called Brownian motion and is a combination of frictional and random forces. The size of the particles immersed in the fluid are usually between 1 nm to less than 10 μm. For a freely moving particle in the fluid, its motion is described by the Langevin equation [136]:

$$m\,\ddot{\mathbf{q}} = -\mathbf{C_D}\dot{\mathbf{q}} + \mathbf{F_L} \tag{6.12}$$

where m the mass of the particle, $\ddot{\mathbf{q}}$ the particle's acceleration, $\mathbf{C_D}$ the drag coefficient as described in Section 6.4.2, $\dot{\mathbf{q}}$ the particle's velocity and $\mathbf{F_L}$ the random thermal force. The random force $\mathbf{F_L}$ is a stochastic variable which is described by a Gaussian distribution. The general solution of equation (6.12) is given by:

$$\dot{\mathbf{q}} = \dot{\mathbf{q}}_\mathbf{0}\, e^{-t/\tau_B} + \frac{1}{m}\int_0^t e^{-(t-s)\tau_B}\mathbf{F_L}(s) \tag{6.13}$$

where $\dot{\mathbf{q}}_\mathbf{0}$ the initial velocity of the particle at $t = 0$ and $\tau_B = \frac{m}{C_D}$ the relaxation time. Using the general solution, the average kinetic energy of the particle, in this case the microstructure, can be obtained from:

$$< K >=< \frac{1}{2}m\dot{\mathbf{q}}^2 > \tag{6.14}$$

The average kinetic energy of the microstructure in thermal equilibrium due to the Brownian motion is used further in Section 6.5.1 for the calibration routine to obtain the stiffness of the optical trap.

6.4.4 Magnetic Force

The magnetic field can be generated by permanent magnets or magnetic coils. Permanent magnets can create large fields without the need of electric current but they require motion of the magnets around the microrobot workspace. In addition, the magnetic field can only be turned off by moving the magnet far from the microrobot workspace [137]. Alternatively, electromagnetic coils can be used in order to generate a magnetic field which can produce a varying magnetic field, which is either static or rotating. The strength of the magnetic field is assumed to be proportional to the electric current which is generating it. The magnetic force $\mathbf{f_m}$ and torque $\boldsymbol{\tau_m}$ with a magnetic moment $\mathbf{m_b}$ are given by:

$$\mathbf{f_m} = \mathbf{m_b}\ (\nabla\ \mathbf{B}) \tag{6.15}$$

$$\boldsymbol{\tau_m} = \mathbf{m_b}\ \times\ \mathbf{B} \tag{6.16}$$

where $\mathbf{B}$ the magnetic flux density. The magnetization $|\mathbf{M}|$ induced to the microrobots depends on the amplitude of the magnetic field strength $\mathbf{H}$:

$$|\mathbf{M}| = \chi|\mathbf{H}| \tag{6.17}$$

where χ the magnetic susceptibility of the material. The relation between the magnetic flux density, the magnetic field strength and the magnetization is given by:

$$\mathbf{B} = \mu_0\ (\mathbf{H} + \mathbf{M}) \tag{6.18}$$

In the proposed methodology, a static homogenous magnetic field is used to magnetize the ferromagnetic layer of the microrobot and create an attractive force between the components sufficiently close to facilitate the assembly of the kinematic chain. It is worth noting that the gradient created by the magnetic setup is used only for assembly and not for displacement of the microrobots. The magnetic field is generated by a setup of magnetic coils paired in Helmholtz configuration as presented in [37] and is further described in the presentation of the experimental setup.

6.4.5 Contact Force

As mentioned, once the static magnetic field is on and the two components are sufficiently close, then the two components come to contact. Therefore, an additional force which is the contact force arises between two surfaces. In the macroscale, there are several models to describe contact, such as a rigid and frictionless point contact, rigid point contact with friction or soft and deformable contact [138]. In an assembled kinematic chain, there is a sphere to plane contact which can be modelled as a rigid point contact with friction [138]:

$$\mathbf{F_C} = \begin{bmatrix} 1 & 0 & 0 \\ 0 & 1 & 0 \\ 0 & 0 & 1 \\ 0 & 0 & 0 \\ 0 & 0 & 0 \\ 0 & 0 & 0 \end{bmatrix} f_c, \quad f_c \ \in \ FC_c \tag{6.19}$$

$$FC_c = \{f \ \in \ \mathbb{R}^3 : \sqrt{{f_1}^2 + {f_2}^2} \leq \mu_f, f_3 \geq 0\} \tag{6.20}$$

where μ_f the friction coefficient which depends on the materials of the surfaces in contact.

In the presented system, the contact force between the two components is the result of the attractive magnetic force and the adhesion force. Hence, the contact force $\mathbf{F_c}$ exerted by one component to the other is equal to:

$$\mathbf{F_c} = \mathbf{F_m} + \mathbf{F_a} \tag{6.21}$$

where $\mathbf{F_m}$ the magnetic force for each component and $\mathbf{F_a}$ the adhesion force. These force components are briefly described in the following.

6.4.5.1 Magnetic Force

The magnetic force that each of the component experiences within the generated magnetic field is equal to:

$$\mathbf{F_m} = \int^{V} \mathbf{f_m} \, dV \tag{6.22}$$

where $\mathbf{f_m}$ as defined in equation (6.15) and V the volume of the magnetic dipole.

6.4.5.2 Adhesion Force

Surface forces, which are electrostatic, Van der Waals forces and capillary forces, have a significant effect when two surfaces are in contact in the microscale. These forces result to microrobots getting attached on the contact surface. The force $\mathbf{F_a}$ needed to separate the two components and overcome the combined effect of these forces is called adhesion force. It depends on the material of the surfaces in contact and on the medium in which the microrobots are in. Electrostatic forces can be either attractive or repulsive [2]. The Van der Waals forces also have a significant effect when dimensions scale down. In particular, the Van der Waals force $\mathbf{F_{VDW}}$, which are intermolecular forces, between a sphere and a half-space can be modelled as [2]:

$$\mathbf{F_{VDW}} = \frac{H\ r}{8\pi \mathbf{d}^2} \tag{6.23}$$

where H the Hamaker constant, r the radius of the sphere and $\mathbf{d}$ the distance between the sphere and the half-space.

6.4.6 Dynamic Model Assumptions

The following assumptions are taken into account for the derivation of the dynamic model.

1. The fluid medium in which the microrobots are moving is water, and therefore is continuous, incompressible and a Newtonian medium. Hence, the Navier-Stokes equation, given in (6.2), holds for the described experimental environment.

2. The Reynolds number, given by equation (6.4), for a microstructure moving in water is equal to:

   $$Re = 4.49\ 10^{-4} \tag{6.24}$$

   for $\rho = 997\ kg/m^3$ which is the water density, $\mu = 8.9\ 10^{-4}\ Pas$ which is the water viscosity at $25\ ^oC$, $u_\infty = 20\ \mu/s$ the maximum velocity of a microstructure moving in water and $L = 20\ \mu m$ the maximum dimension of the microrobot. Therefore, the assumption of Stokes flow of equations (6.5) and (6.11) hold for the presented system.

3. For low Reynolds numbers, the inertial forces are negligible, and consequently it is assumed that $m\ \ddot{\mathbf{q}} \approx 0$, where m the mass of the microstructure and $\ddot{\mathbf{q}}\ \in \mathbb{R}^2$ the microstructure acceleration.

4. It is assumed for simplification that equation (6.11) gives the drag force for an individual component of the assembly. In the force model derived for the kinematic chain, it is assumed that the total drag force can be obtained as a sum of the drag force experience by each individual link. This implies that the drag force is considered to be linear, which is generally not the case. In particular, the flow distribution of one component affects the flow distribution that is experienced by a second component that is attached to the first one and could alternatively be estimated as in [139].

5. The Brownian motion is only observable by the CCD camera when the microstructures are static, i.e. not moved by the optical trap. Therefore, $\mathbf{F_L} \approx 0$, except for the cases where the microstructures are trapped by an optical trap but are kept fixed at a specific position. This case stands for the trapping stiffness calibration procedure described in Section 6.5.1.

6. It is assumed that the assembly is grasped by one optical trap but the modelling can be extended to multiple traps.

7. It is considered that the trapping radius of the laser is sufficiently small so that the trapping force is exerted only on the spherical handle and not on the cylinder. This implies that the trapping force can be modelled by the spring model.

The above assumptions are taken into account in order to derive a mathematical expression for the dynamics of an individual structural component or a kinematic chain moving in the water under the influence of an optical trap and the magnetic force.

6.4.7 Dynamics of Individual Components before Assembly

Consider a microstructure grasped by an optical trap from the spherical handle. Prior to contact and under the influence of the optical trap, the dynamic equation of a trapped component is as follows:

$$m\ \ddot{\mathbf{q}} = \mathbf{F_{trap}} + \mathbf{F_{drag}} + \mathbf{F_L} \tag{6.25}$$

where m the mass of the microstructure, $\ddot{\mathbf{q}}\ \in \mathbb{R}^2$ the microstructure acceleration, $\mathbf{F_{trap}}\ \in \mathbb{R}^2$ the trapping force as in equation (6.1), $\mathbf{F_{drag}}\ \in \mathbb{R}^2$ the drag force as in equation (6.11) and $\mathbf{F_L}\ \in \mathbb{R}^2$ the random thermal force. Using assumptions 3 ($m\ \ddot{\mathbf{q}} \approx 0$) and 5 ($\mathbf{F_L} \approx 0$) of Section 6.4.6 into equation (6.25), it can be written as:

$$\mathbf{F_{trap}} + \mathbf{F_{drag}} = 0 \tag{6.26}$$

6.4.8 Dynamics of Assembled Kinematic Chain

Consider the assembly of N microstructures as described in Section 6.2 as a kinematic chain of rigid bodies where each microstructure represents one link. The dynamic equation of the i_{th} microstructure grasped by an optical trap in a fluid medium in contact with other magnetically assembled microstructures is modelled as follows:

$$m_i\ \ddot{\mathbf{q}}_\mathbf{i} = \mathbf{F_{trap_i}} + \mathbf{F_{drag_i}} + \mathbf{F_{L_i}} + \sum_{j=1}^{k} \mathbf{F_{C_j}} \tag{6.27}$$

where m_i the mass of the i_{th} microstructure, $\ddot{\mathbf{q}}_\mathbf{i}\ \in \mathbb{R}^2$ the microstructure acceleration, $\mathbf{F_{trap_i}}\ \in \mathbb{R}^2$ the trapping force induced by a single trap,

$\mathbf{F_{drag_i}} \in \mathbb{R}^2$ the resulting drag force, $\mathbf{F_{L_i}} \in \mathbb{R}^2$ the random thermal force and $\mathbf{F_{C_i}} \in \mathbb{R}^2$ the contact force on the j_{th} contact point of the microstructure with $k = 1, 2$ as each microstructure has two tips which are available for attachment, and therefore maximum two contact points. Using assumptions 3 ($m_i\, \mathbf{\ddot{q}_i} \approx 0$) and 5 ($\mathbf{F_{L_i}} \approx 0$) of Section 6.4.6 into equation (6.27), it yields:

$$\mathbf{F_{trap_i}} + \mathbf{F_{drag_i}} + \sum_{j=1}^{k} \mathbf{F_{C_j}} = 0 \tag{6.28}$$

Similarly, the dynamic equation of a microstructure which is not trapped by an trapping force ($\mathbf{F_{trap_i}} = 0$) and is in contact with other microstructures under the assumptions 3 and 5, is given by:

$$\mathbf{F_{drag_i}} + \sum_{j=1}^{k} \mathbf{F_{C_i}} = 0 \tag{6.29}$$

6.4.8.1 Displacement Force

Consider the system of N assembled microstructures in a kinematic chain as modelled in Section 6.4.8. As mentioned in assumption 6 of Section 6.4.6, it is considered that the assembly is grasped by a single optical trap from one of the spherical handles. Under assumption 4 (that the drag force is linear), the displacement force that is required to move the kinematic chain is equal to:

$$\mathbf{F_{dp}} = \mathbf{F_{trap}} + \sum_{i=1}^{N} \mathbf{F_{drag}}_i \tag{6.30}$$

where $\mathbf{F_{trap}}$ the trapping force exerted on the grasped microstructure and $\mathbf{F_{drag}}_i$ the drag force exerted on the i_{th} component of the assembly with $i = 1, .., N$. The above equation assumes that there is no sliding or relative motion between the contact surfaces. In case of sliding, equation (6.30) can be extended by an additional term describing the sliding friction force between each contact as follows:

$$\mathbf{F} = \mathbf{F_{trap}} + \sum_{i=1}^{N} \mathbf{F_{drag}}_i + \sum_{i=1}^{N-1} \mathbf{F_{sf}}_i \tag{6.31}$$

where $\mathbf{F_{sf}}_i$ the sliding friction force of the i_{th} contact between two components. From equation (6.30) for an assembly of two components, the displacement force is equal to:

$$\mathbf{F_{dp}} = \mathbf{F_{trap_1}} + \mathbf{F_{drag_1}} + \mathbf{F_{drag_2}} \tag{6.32}$$

6.4.8.2 Disassembly Force

The disassembly force refers to the force that is needed to separate two microstructures which are in contact under the influence of the magnetic field. The disassembly is performed by grasping and moving away one of the microstructures while the second microstructure moves freely in the medium, i.e. it is not grasped by an optical trap. From equation (6.28), for a kinematic chain of two microstructures, where there is only one contact point, the disassembly force $\mathbf{F_d}$ between two components is equal to the contact force:

$$\mathbf{F_d} = \mathbf{F_c} = \mathbf{F_{trap}} + \mathbf{F_{drag}} \tag{6.33}$$

where $\mathbf{F_{trap}}$ and $\mathbf{F_{drag}}$ the optical and the drag force exerted on the disassembled microstructure. Some additional assumptions are made for the disassembly force model:

- It is assumed that the disassembled microstructure does not have a second microstructure attached to it on its second tip. Therefore, it is assumed that there is only one contact point. However, the model can be extended to two contact points.

- As the contact force is difficult to be accurately calculated from its individual force components $\mathbf{F_m}$ and $\mathbf{F_a}$, as described from the analysis in Section 6.4.5, it is calculated indirectly from equation 6.33.

6.5 System Identification

In order to calculate the forces as presented, the system's parameters, the trapping stiffness $\mathbf{k}$ and the drag coefficient $\mathbf{C_D}$ need to be identified. The calibration methods that were used in the experiments to estimate the trapping stiffness and the drag coefficient along the x and y-axis are described in the following section.

6.5.1 Trapping Stiffness Estimation

There are several methods that allow the estimation of the stiffness of a laser trap using position measurements [140]. The position measurements can be obtained either by using a CCD camera or a Quadrant Photodetector. Active calibration methods require translating the microstructure using the piezo stage while the microstructure is trapped. This method calculates the trapping stiffness from the dynamic equation of a trapped microsphere using the measured positions of the microsphere. This method assumes that the particle is spherical and therefore the viscous drag coefficient can be calculated using equation (6.10). Passive calibration methods do not require translation of the stage, but instead they rely on observing the Brownian motion of a trapped microstructure and estimate the trapping stiffness using either the power spectral density, the equipartition theorem or the Boltzmann

Statistics Method. The power spectral density method requires high position samplings with frequencies from 10 up to 50 kHz, hence it is not suitable for position sampling using the CCD camera. Compared to this method, the equipartition theorem method and the Boltzmann statistics method can also be performed when the positions are sampled by a CCD camera. These two methods do not require prior knowledge of the trap coefficient and do not assume that the trapped microobject is a sphere. For these reasons, and also because the Boltzmann statistics method is more robust to noise than the equipartition theorem method, the estimation of the trapping stiffness is performed using that method which is described in the following section.

6.5.1.1 Boltzmann Statistics Calibration Method

The trapping stiffness is estimated using the Boltzmann Statistics Method which estimates the trapping stiffness using the microrobot position measurements as sampled by a CCD camera. This method uses observations from the Brownian motion of a trapped microrobot. According to the Boltzmann statistics approach, the probability distribution of the positions of a microrobot due to Brownian motion is a Gaussian distribution. The probability density of the positions of a microrobot as a function of the potential energy of the optical trap in thermal equilibrium is given by [141]:

$$p(q_i)dx = p_m \; e^{-E(q_i)/k_B T} \tag{6.34}$$

where p_m the probability of the mean position of the microrobots, $E(x)$ the potential energy of the optical trap, k_B the Boltzmann constant and T the temperature of the medium in which the microrobot is suspended in and q_i the 1-D position of the microrobot with $i = x, y$. Solving equation (6.34) for

$E(q_i)$, it yields:

$$E(q_i) = -k_B T \, \ln(p(q_i)) + k_B T \, \ln(p_m) \tag{6.35}$$

The energy is also equal to the kinetic energy of the trapped particle which is equal to:

$$E(q_i) = \frac{1}{2} k_i {q_i}^2 \tag{6.36}$$

where k_i the trapping stiffness along the i_{th} axis with $i = x, y$. Therefore, the trapping stiffness can be obtained by fitting a parabolic function as in equation (6.36) to the values as calculated from (6.35).

6.5.2 Drag Coefficient Estimation

The drag coefficient C_D is estimated using an active displacement method that takes into account the estimated trapping stiffness as calculated from the method described in Section 6.5.1.1. In this case, the microrobot is trapped by the laser beam which is kept fixed while the piezo stage is moved. The drag coefficient is calculated using the relative displacement of the microrobot and the laser trap within the fluid medium for the estimated trapping stiffness of the previous section. From the equations (6.1), (6.11) and (6.25), and under the assumptions 3 and 5 of Section 6.4.6, it is obtained:

$$\mathbf{C_D} \, \dot{\mathbf{q}} = \mathbf{k}(\mathbf{q} - \mathbf{u}) \tag{6.37}$$

Assuming that the trapping stiffness and the relative position of the microrobot and the laser beam are known, the drag coefficient can be estimated using linear regression on the above equation.

6.6 Experimental Setup

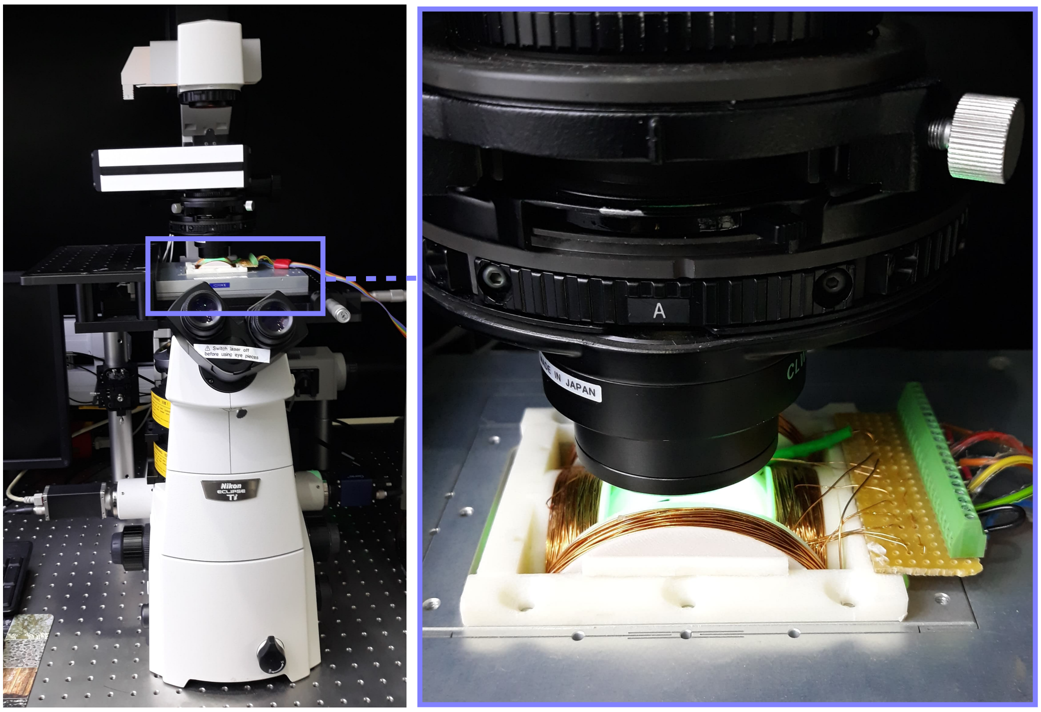

Figure 6.4: The experimental setup comprises an Optical Tweezers with an integrated set of magnetic coils placed fitted on the sample holder on the piezo stage.

The setup consists of an Optical Tweezers (Elliot Scientific, UK) and a 3D-printed device that integrates the magnetic coils with the Optical Tweezers fitted on the piezo stage as shown in Figure 6.4. The device integrates three magnetic coils for 3D magnetic actuation. The dimensions and the design of the magnetic coils are as presented in [37] and given in Table 6.1. The coils are paired in an Helmholtz configuration and are used to create a static homogenous magnetic field. The microstructures are fabricated as described in Section 3.3. The glass slide with the nickel-coated microrobots, that are covered with the 3D-printed mask, is placed on a coverslip on top of an imaging spacer containing DI water between the two glasses (Figure

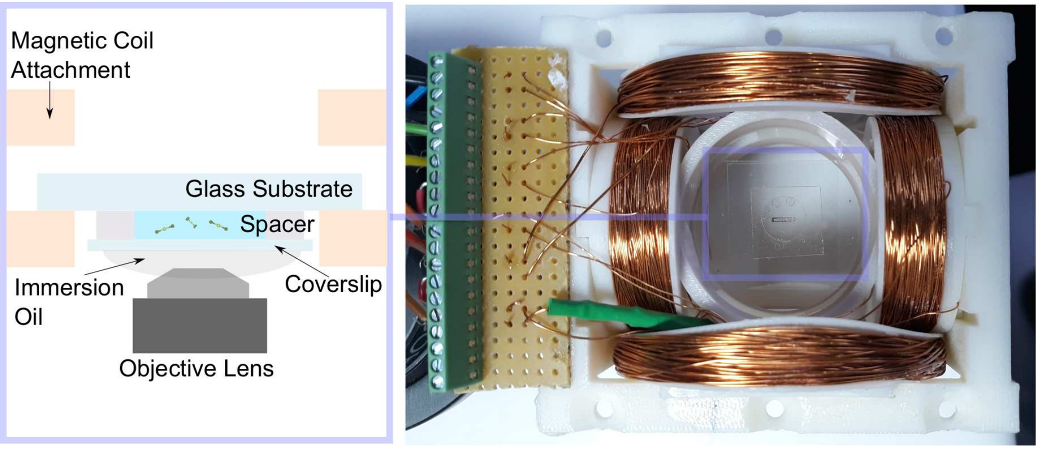
Magnetic Coil Attachment
Glass Substrate
Spacer
Immersion Oil
Coverslip
Objective Lens

Figure 6.5: Schematic of the side view of the experimental configuration of the samples placed inside the coils and on the Optical Tweezers (left). Top view of the coils placed on the piezo stage with a glass slide containing microrobots (right).

Coil		1_{st}	2_{nd}	3_{rd}
Coil radius	[mm]	50	37	38
Number of turns per coil		260	100	110
Maximum magnetic power at the centre	[mT]	10	10	10

Table 6.1: Magnetic coil setup parameters

6.5-left). The sample is placed inside a sonicator bath in order to remove the masks and also detach the microrobots from the glass slide. This procedure avoids transferring the detached microrobots between workspaces as the sample can be placed directly inside the sample holder as shown in Figure 6.5.

6.7 Experimental Results

6.7.1 Reconfigurable Microassembly

The assembly process was performed experimentally in order to assess the repeatability and reversibility of the proposed method. Distributions for the estimated forces for the displacement of the microassembly and the disassembly are also calculated. In the following, an indicative experiment is presented which demonstrates the assembly and disassembly of a three-link kinematic chain consisting of a link with rectangular tips and two links with spherical tips. It is also essential to have an estimation of the range of the forces that are required to manipulate and reconfigure the assembly. As there the only feedback is the visual feedback from the camera, the forces are estimated visually from the 2D position measurements of the CCD camera. The forces that are characterized are the force required to move the assembly and the force needed to disassemble the spherical joint, which quantifies the contact force between the contact surfaces to reconfigure the assembly. As mentioned, it is a combination of magnetic, adhesion and frictional forces between the contact surfaces. A number of experiments were performed for a two-link assembly to experimentally calculate the distribution of the force required to move an assembly as well as the distribution for the disassembly force for the spherical joint.

6.7.1.1 Assembly of Spherical Joint using the Magnetic Field

The microstructures to be assembled were placed close to each other using the optical trap before the magnetic field is activated. Once the components were brought to close proximity, the Optical Tweezers were deactivated. A static homogenous magnetic field is used in order to magnetize the microstructures

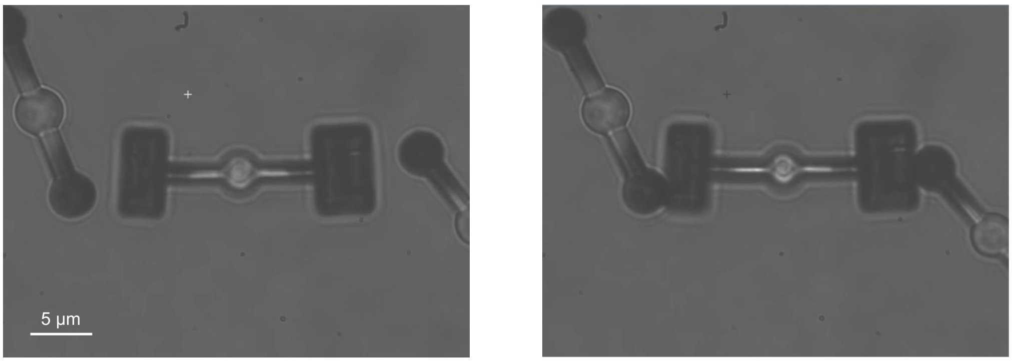

(a) t=0 s (Magnet on, laser off) (b) t=3 s (Magnet on, laser off)

Figure 6.6: Assembly of spherical joint

and induce the attractive force between them. The distance between the components, as it can also be seen from Figure 6.6a, is approximately 1 μm. During this stage, the optical trap is switched off, so that the trapping force does not overcome the magnetic force and obstruct the assembly. An indicative set of images shown three microstructures before and after assembly is shown in Figure 6.6.

6.7.1.2 Displacement of Assembly and Joint Rotation under the Magnetic Field using the Optical Tweezers

At this stage, the magnetic field remains on to maintain the attraction between the microstructure, while the assembly is grasped by one optical trap. A kinematic chain translated along the xy-plane using a single optical trap is shown in Figure 6.7. The tip of the microstructure which is attached at the end of the kinematic chain can be used as an end-effector tip for 3D manipulation. This link can be grasped by the spherical handle for planar displacement and rotation. It can also be displaced vertical by inducing a vertical force from the optical trap on the metal layer. This can be achieved by applying an instantaneous laser pulse to the spherical tip. The vertical

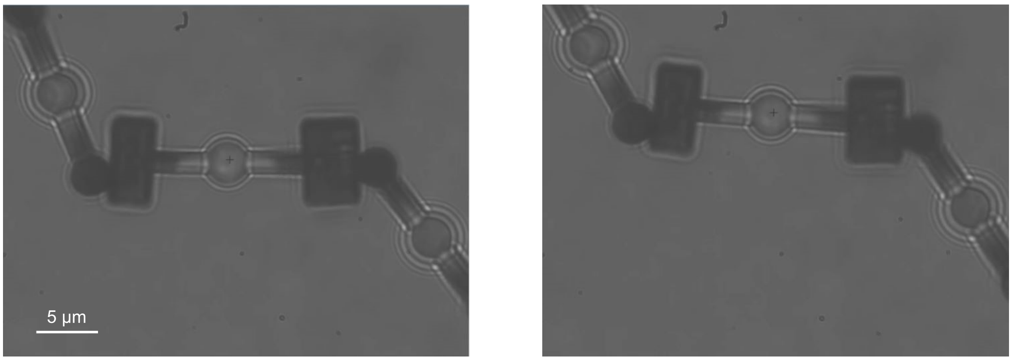

(a) t=0 s (Magnet on, laser on)

(b) t=2 s (Magnet on, laser on)

Figure 6.7: Displacement of assembly along the y-axis

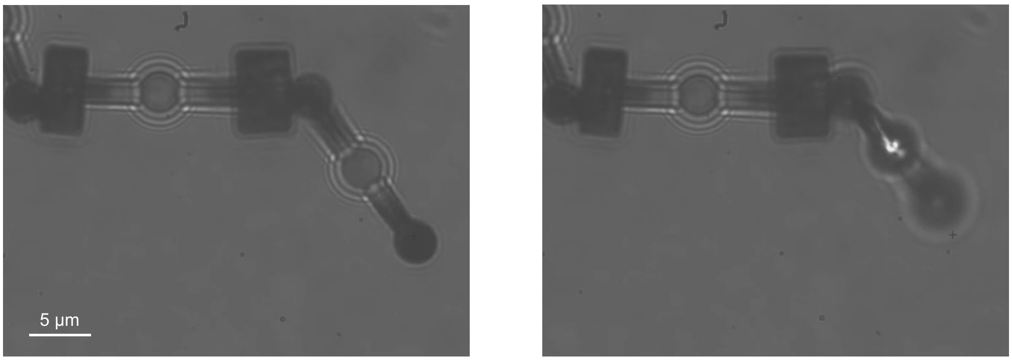

(a) t=0 s (Magnet on, laser on)

(b) t=1 s (Magnet on, laser on)

Figure 6.8: Out-of-plane displacement of end-effector from vertical force induced but the laser

motion of the attached microstructure is shown in Figure 6.8.

6.7.1.3 Disassembly of Spherical Joint under the Magnetic Field using the Optical Tweezers

In order to reconfigure the assembly, it is important that the trapping force is sufficient to disassemble two microstructures without switching off the magnetic field. By maintaining the magnetic field, partial reconfiguration and disassembly of specific microstructures can be achieved. It is also essential that this motion is repeatable and that the disassembly of the same

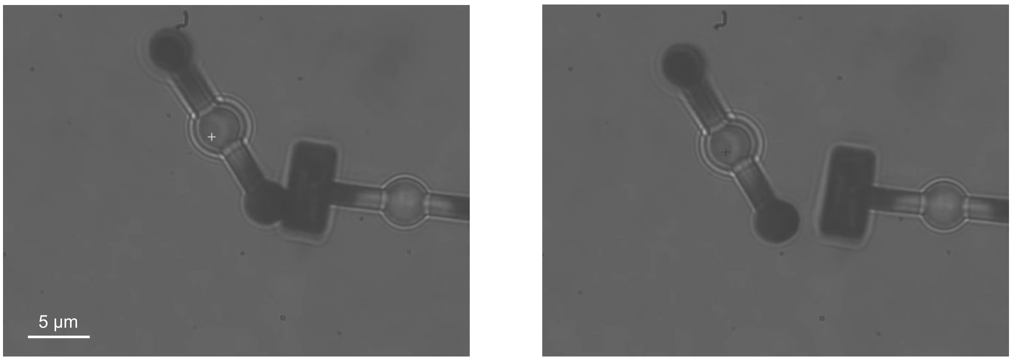

(a) t=0 s (Magnet on, laser on) (b) t=1 s (Magnet on, laser on)

Figure 6.9: Disassembly of spherical joint using the Optical Tweezers under the magnetic field

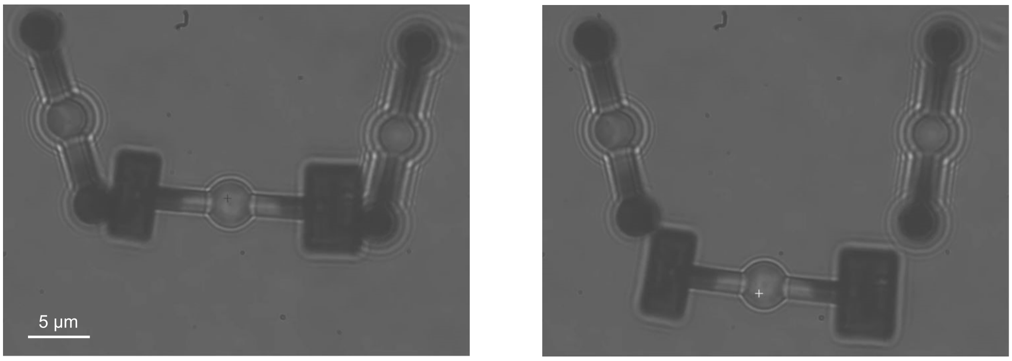

(a) t=0 s (Magnet off, laser on) (b) t=1 s (Magnet off, laser on)

Figure 6.10: Disassembly of the kinematic chain after deactivation of the magnetic field

two microstructures can be performed multiple times. In Figure 6.9, it is demonstrated how a microstructure with spherical tips is removed from the kinematic chain using one optical trap and under static magnetic field. The components are all released from the assembly after the magnetic field is switched off. It is shown in Figure 6.10 that the middle component is removed from the other two microstructures as the magnetic attractive force between the microstructures is off.

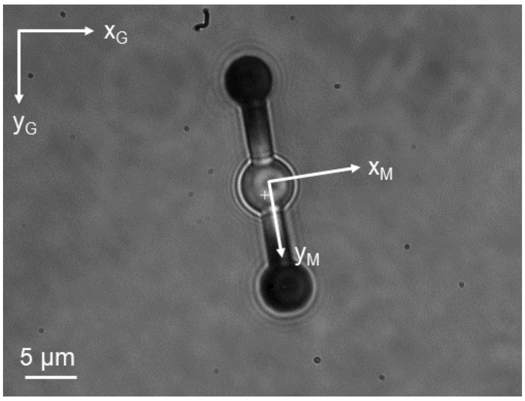

Figure 6.11: Global frame of reference {G} and microrobot co-ordinate frame {M}

6.7.2 System Identification

In order to estimate the displacement and disassembly forces, an estimation of the values for the trapping stiffness and drag coefficients needs to be obtained. These values are estimated using the methods and modelling described in Sections 6.5.1 and 6.5.2.

6.7.2.1 Trapping Stiffness Estimation

To perform the trapping stiffness calibration using the Boltzmann statistics method as described, five sets of experiments were recorded in which the cylindrical microrobot with spherical handles was trapped using five different values of laser powers ranging from 0.1 W to 0.5 W. This range was chosen as most of the experiments were performed using laser powers in this range. The configuration of the co-ordinate frames is shown in Figure 6.11. In each experiment, the CCD camera was used to record the Brownian motion of the microrobot while trapped by the spherical handle. Each video was processed to obtain the 2D position of the spherical handle while the duration of each recording was from 8 to 13 seconds. The calculated positions were normalized

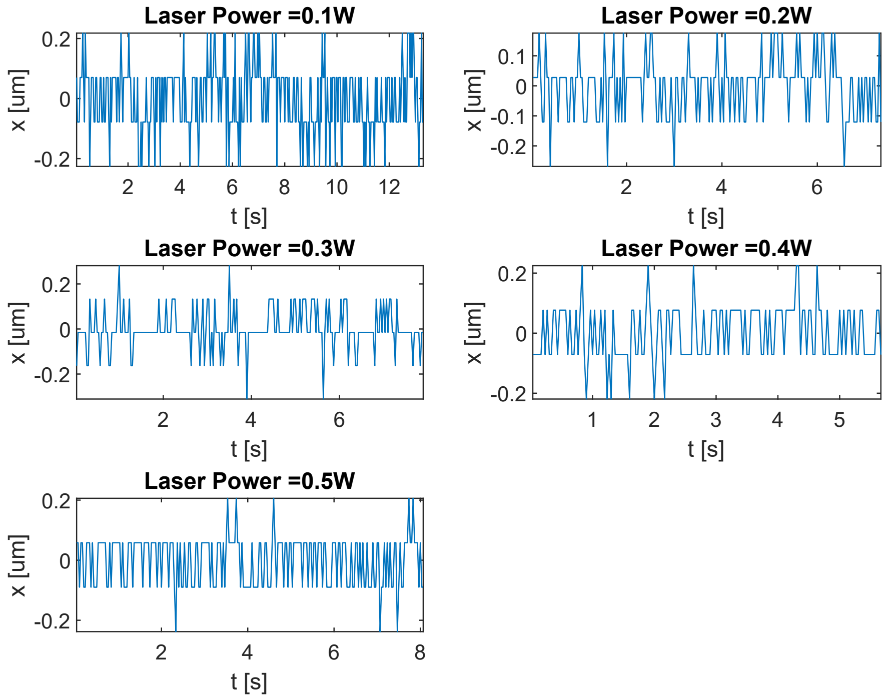

Figure 6.12: Relative displacement of the microrobot with respect to the mean displacement along the x-axis from Brownian motion for different laser powers

around the mean displacement value. The normalized positions are shown in Figures 6.12 and 6.13. A Gaussian distribution for set of positions was calculated as shown in Figures 6.14 and 6.15. Given these distributions, the values:

$$y(q_i) = -\ \ln(p(q_i)) +\ \ln(p_m) \tag{6.38}$$

are calculated for each distribution. The above equation stems from (6.35) in which the term $k_B T$ is omitted due to scaling issues. A parabolic function $y(q_i) = \alpha\ {q_i}^2$ is then fitted to each set of calculated values as depicted in Figures 6.16 and 6.17. The trapping stiffness k_i is obtained from the estimated

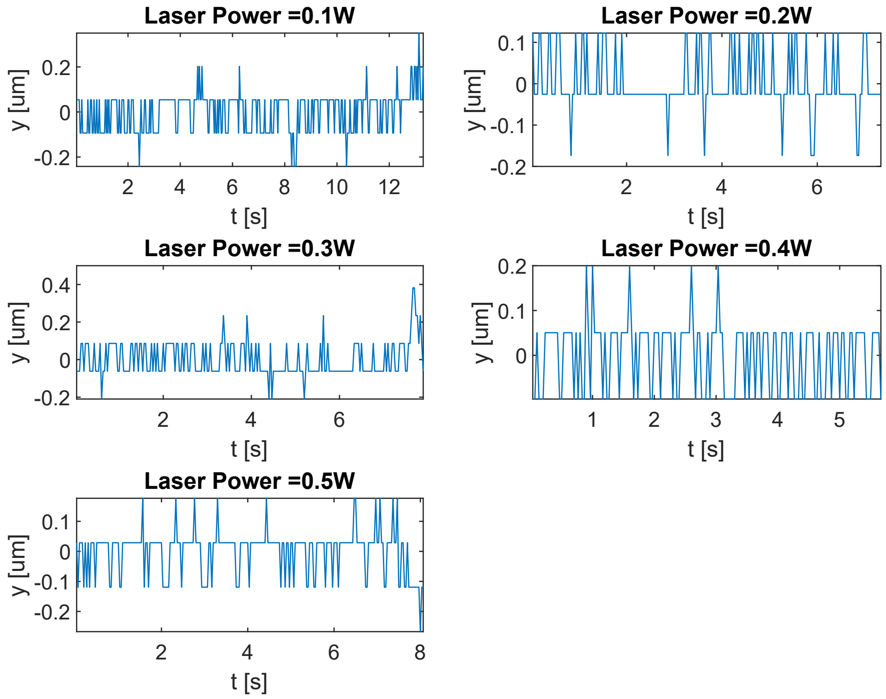

Figure 6.13: Relative displacement of the microrobot with respect to the mean displacement along the y-axis from Brownian motion for different laser powers

parameter α as follows:

$$k_i = \frac{a}{2k_B T}, \; i = x, y \tag{6.39}$$

The temperature is considered to be $T = 298.15\ K$ at 0.1 W. It is considered that the temperature increases by 0.8 K for every laser power increase of 0.1 W. For Figures 6.18-right and 6.19-right, it is observed that the displacements have a decreasing standard deviation as the laser power is increasing, although some noise can be observed disturbing the descending slope of the curve. It can be seen that the estimated stiffness values along the y-axis (Figure 6.19-left) are more noisy than the corresponding values

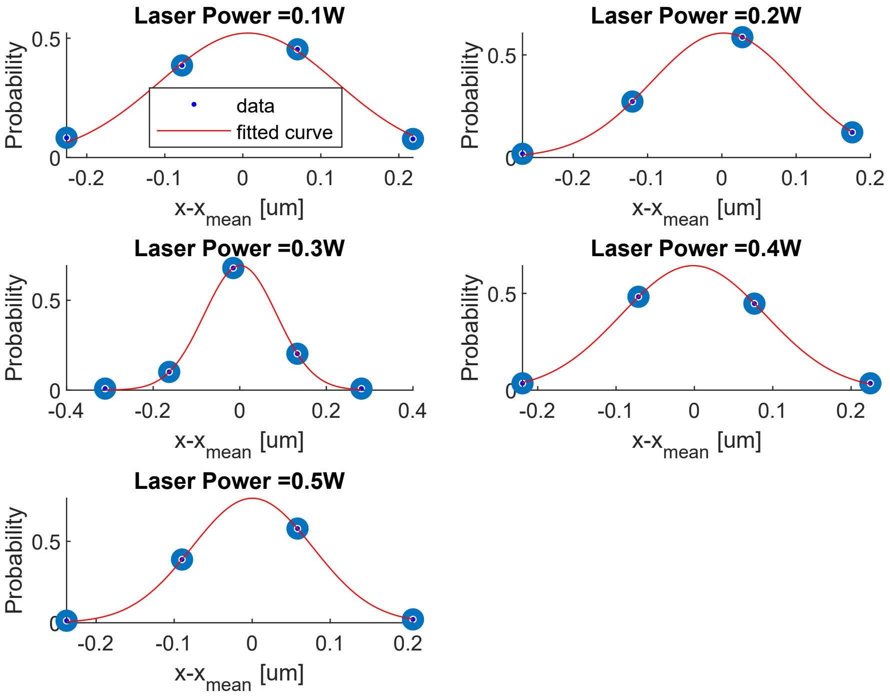

Figure 6.14: Probability distribution for Brownian motion displacements for different laser powers (x-axis)

for the x-axis (Figure 6.18-left). This because the y direction corresponds to the longest dimension of the cylinder. This error is likely to be introduced because the y-axis of the cylinder is not perfectly aligned with the horizontal direction of the global frame of reference {G} (Figure 6.11), hence there is a larger deviation. This is in contrast to the x dimension of the cylinder, which is smaller and there is no misalignment to the x-axis of the co-ordinate frame. The overall estimation could be improved by obtaining position data using the Quadrant Photodetector sensor rather than the CCD camera which has a lower sampling rate.

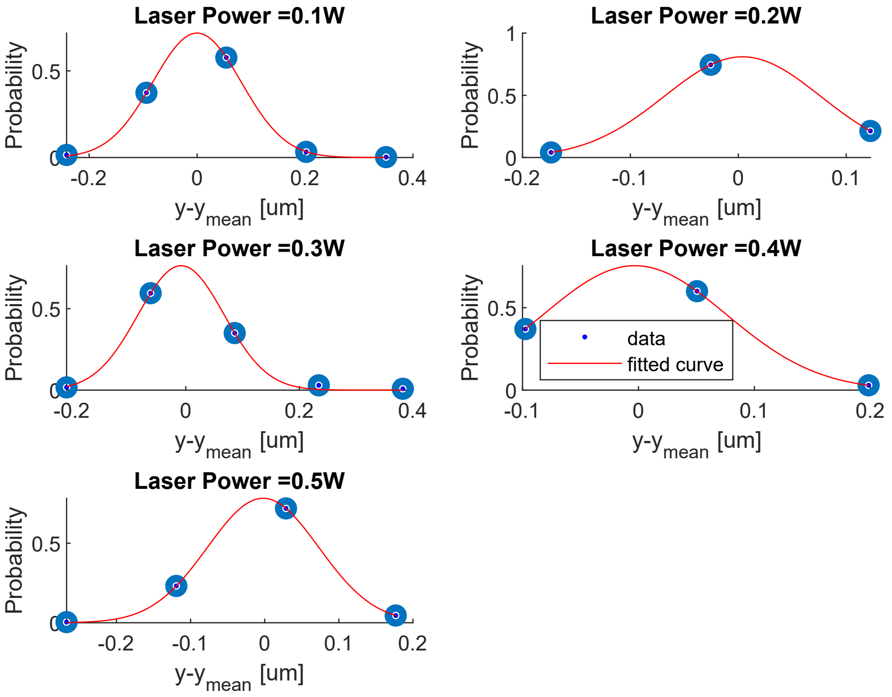

Figure 6.15: Probability distribution for Brownian motion displacements for different laser powers (y-axis)

6.7.2.2 Drag Coefficient Estimation

Two sets of experiments were recorded in order to perform the calibration procedure for the drag coefficient. The stiffness value as obtained from the previous calibration procedure is used in order to estimate the drag coefficient. In this experiment, a microrobot was trapped by the laser and was translated by moving the piezo stage while the laser beam was kept at a fixed position, as shown in Figure 6.20. The laser power was set to 0.2 W. The microrobot displacements and the laser position are shown in Figure 6.21. For known trapping stiffness, microrobot velocity and relative laser and microrobot displacements, the drag coefficient is obtained using equation (6.37).

The estimated drag coefficients C_{Dx} and C_{Dy} for the x and y-axis re-

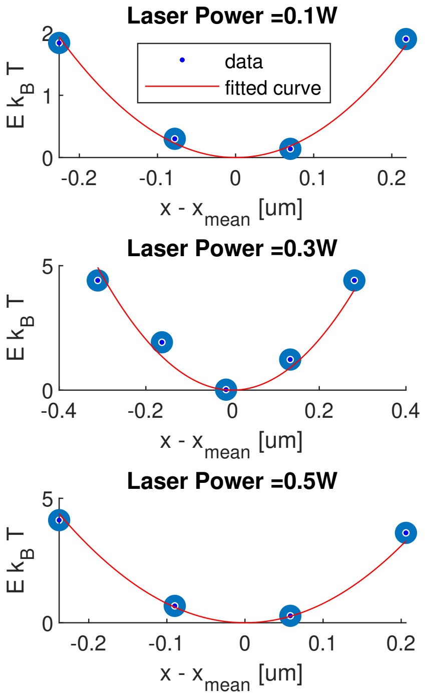

Figure 6.16: Parabolic function fitting for different laser powers (x-axis)

	Drag Coefficient
C_{Dx} $[\frac{pN\ s}{\mu m}]$	0.0253
C_{Dy} $[\frac{pN\ s}{\mu m}]$	0.0073

Table 6.2: Drag force calibration parameters

spectively are given in Table 6.2. From Table 6.2, it can be seen that the drag coefficient along the y-dimension of the microrobot, which is the long dimension of the microrobot (along the cylinder) and that corresponds to the x direction of the global frame is larger that along it's x dimension. This is because the cross-sectional area of along the ly-dimension is smaller than on the x-dimension. From Table 6.2, it can be seen that the drag coefficient C_{Dx} with respect to the x-direction of the global frame, which corresponds to the

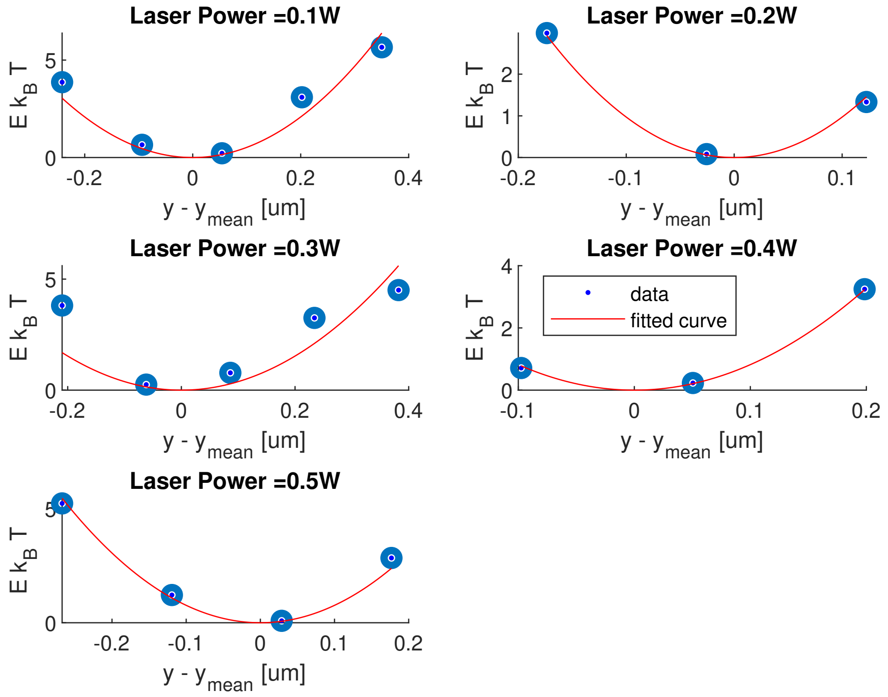

Figure 6.17: Parabolic function fitting for different laser powers (y-axis)

long dimension of the microrobot (along the cylinder and y-dimension with respect of the microrobot frame of reference - Figure 6.20) is larger than C_{Dy}. This is because the cross-sectional area of the cylinder (the y-dimension is smaller) than of the x-dimension.

6.7.3 Force Estimation

After obtaining the estimated values for the trapping stiffness and drag coefficients, an estimation can be obtained for the displacement force required to displace the assembly and the force required to separate two assembled components. A number of experimental sets were performed in which assemblies of two components were attempted to be separated. The dataset includes

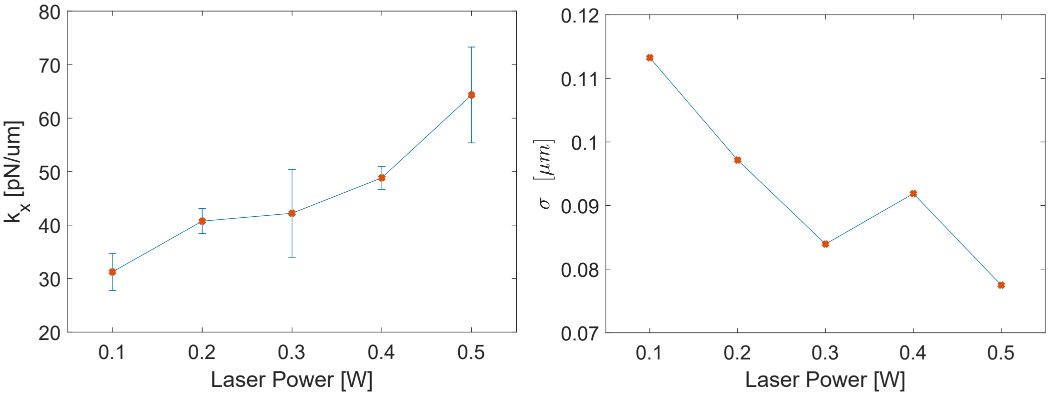

(a) Trapping stiffness (b) Position standard deviation

Figure 6.18: Trapping stiffness and position standard deviation as function of laser power (x-axis)

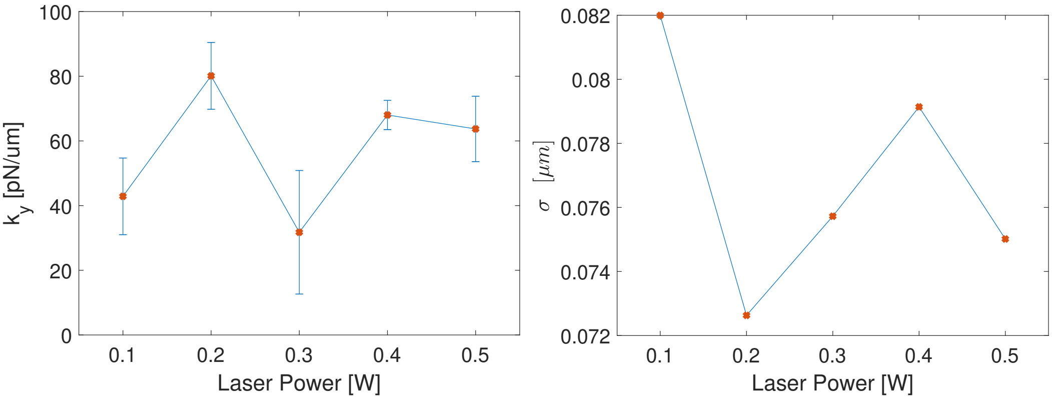

(a) Trapping stiffness (b) Position standard deviation

Figure 6.19: Trapping stiffness and position standard deviation as function of laser power (y-axis)

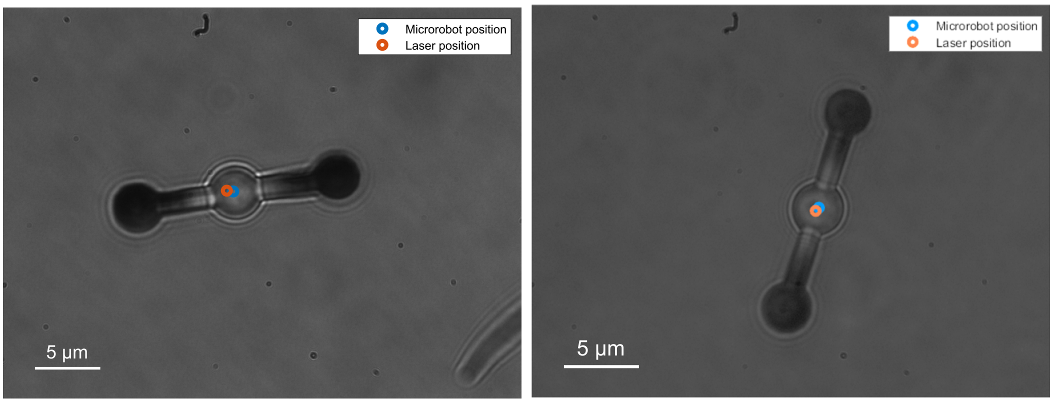
Microrobot position
Laser position
5 μm
Microrobot position
Laser position
5 μm

(a) x-axis calibration (b) y-axis calibration

Figure 6.20: Indicative image frames from the drag coefficient calibration experiments

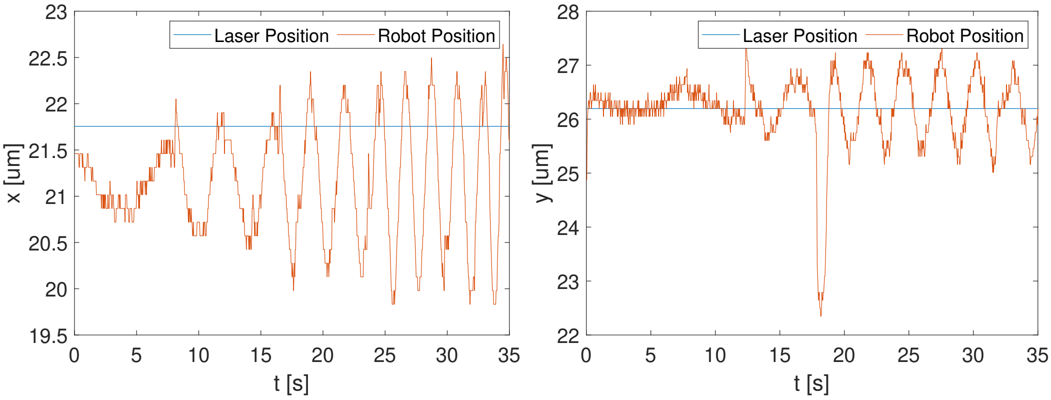

(a) x (b) y

Figure 6.21: Optical trap and microrobot positions along the x and y-axis

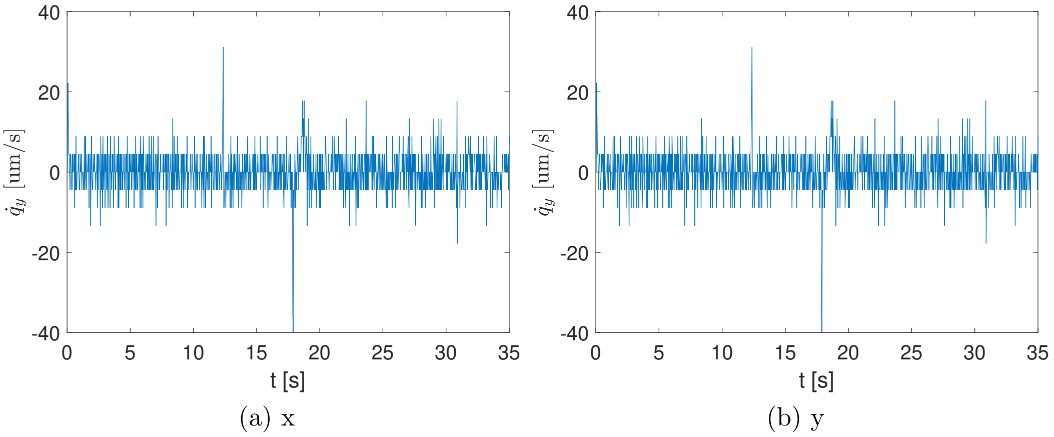

(a) x (b) y

Figure 6.22: Microrobot velocity along the x and y-axis for the drag coefficient calibration experiments

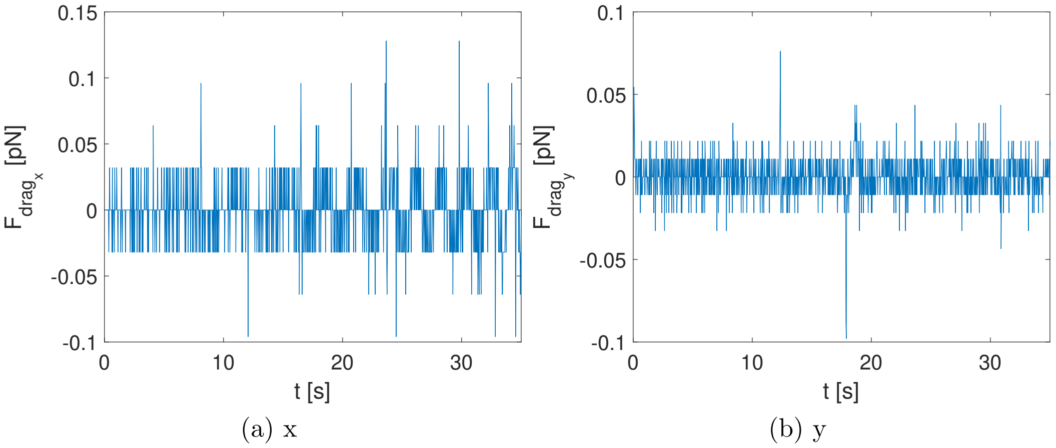

(a) x (b) y

Figure 6.23: Drag force exerted on the microrobot along the x and y-axis for the drag coefficient calibration experiments

12 performed disassembly motion sequences and 7 displacement motion sequences. In order to assess the repeatability of the disassembly motion, the same motion was performed 4 times in order to compare the estimated force values. The metrics that are calculated for each experiment are the mean, standard deviation and median of the trapping force, drag force and the total force.

6.7.3.1 Displacement Force

As mentioned, 7 sets of experiments were performed in which the assembly is transported from one point to another. The assemblies consist of two components, one cylindrical microrobot with spherical and handles and one with rectangular handles. The displacement force is estimated according to the modelling presented in Section 6.4.8.1. From equation (6.32):

$$\mathbf{F_{dp}} = \mathbf{F_{trap_1}} + \mathbf{F_{drag_1}} + \mathbf{F_{drag_2}} \tag{6.40}$$

for $i = 1$ corresponding to the component that is trapped by the laser and $i = 2$ the second attached link to the first one. The mean values, standard deviation and median of the norm of trapping force, drag force and total force needed for displacement, for each experiment are shown in Figures 6.24, 6.25 and 6.26 respectively. The median values for each experimental set for the trapping force, drag force and total force for displacement are given in Table 6.3. The laser power was set to 0.3 W for all experiments.

6.7.3.2 Disassembly Force

It is also essential to estimate the force which is needed to detach two components under the magnetic field, as this is crucial in order to be able to

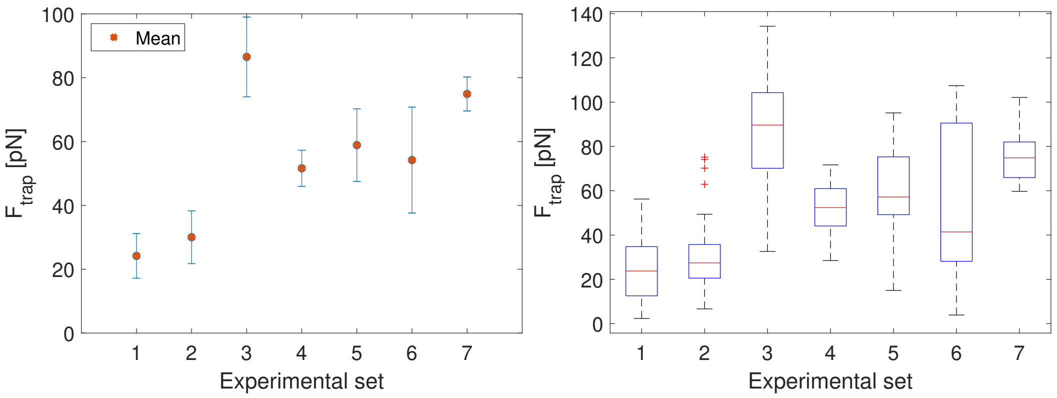

(a) Mean and standard deviation (b) Boxplot and Median (red line)

Figure 6.24: Trapping force for assembly displacement for each experiment

Experiment	**Trapping Force** [pN]	**Drag Force** [pN]	**Total Force** [pN]	**Laser Power** [W]	**Velocity** [$\mu m/s$]
1	23.7884	0.4958	23.2859	0.3	0.148
2	27.4518	0.3412	27.5811	0.3	0.44
3	89.6610	0.5659	89.5659	0.3	0.209
4	52.3875	0.4635	52.6136	0.3	0.2
5	57.2077	0.5188	57.1157	0.3	0.21
6	41.4242	0.3412	41.1623	0.3	0.34
7	74.8630	0.2557	74.9533	0.3	0.22

Table 6.3: Median of force and velocity norms for and corresponding laser power displacement force

reconfigure the assembled microstructures. In the following, we present the estimated force values for 12 different experiments during which disassembly is performed. In order to assess the repeatability and reversibility of this motion, we repeat the same motion 4 times on the same experiment and estimate the force in order to get a distribution of the estimated force needed to detach the same two components. The disassembly force is estimated as

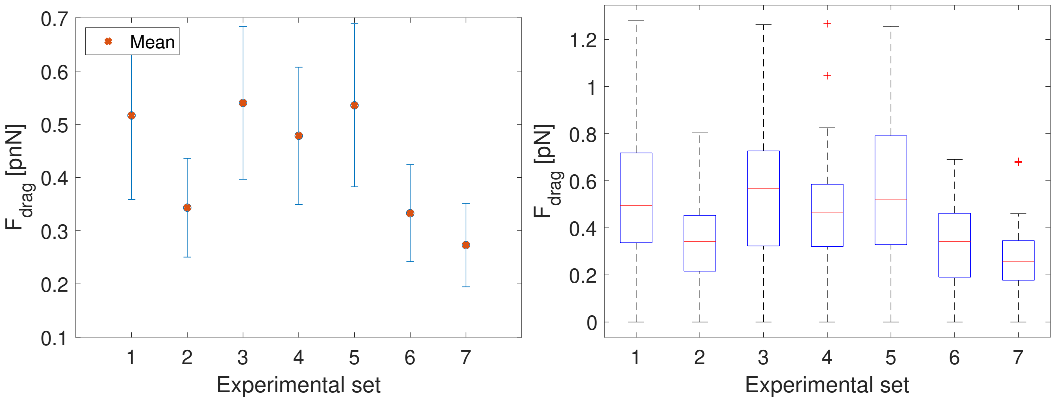

(a) Mean and standard deviation (b) Boxplot and Median (red line)

Figure 6.25: Drag force for assembly displacement for each experiment

given by equation 6.33:

$$\mathbf{F_d} = \mathbf{F_{trap}} + \mathbf{F_{drag}} \tag{6.41}$$

The mean, standard deviation and median of the trapping force, drag force and disassembly force for each of the 12 experiments are given in Figures 6.27, 6.28 and 6.29 respectively. Similarly, the metric for the repeated motion in a single experiment are depicted in Figures 6.30, 6.31 and 6.32 for the trapping force, the drag force and the total disassembly force respectively. The median values for the experimental set of the repeated motion and for all experiments are given in Tables 6.4 and 6.5 respectively.

6.8 Results and Discussion

From Table 6.3, it can be seen that the total displacement force ranges from 23.2 to 89.5 pN. The deviation could be attributed to the different microstructures used for assembly in every experimental set as they were created from different fabrication processes. In addition, the distance of the

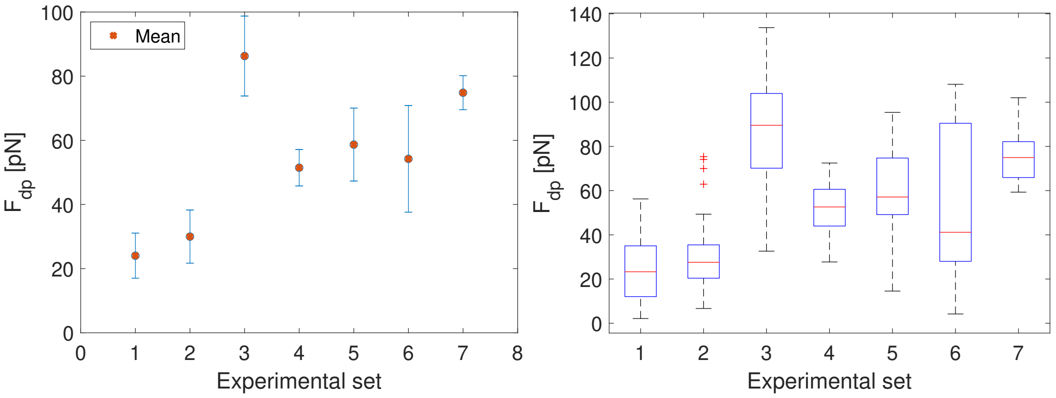

(a) Mean and standard deviation (b) Boxplot and Median (red line)

Figure 6.26: Total displacement force for each experiment

Experiment	**Trapping Force** $[pN]$	**Drag Force** $[pN]$	**Total Force** $[pN]$	**Laser Power** [W]
1	106.5254	0.2331	106.4799	0.4
2	87.9737	0.1460	87.6310	0.4
3	93.7203	0.1166	93.7203	0.4
4	101.0024	0.4662	100.6640	0.4
5	34.4308	0.2247	34.3230	0.3
6	32.5960	0.0622	32.6104	0.4
7	44.5317	0.1123	44.5317	0.4
8	135.6516	0.2247	135.4279	0.4
9	70.6367	0.1166	70.4255	0.3
10	58.6491	0.1123	58.5331	0.4
11	74.9763	0.1166	74.6601	0.4
12	68.0466	0.1765	67.8857	0.4

Table 6.4: Median of force norms and corresponding laser power for joint disassembly (all experiments)

assembly to the glass slide also affects the resistance that could be experienced to move the assembly. An error could also have been introduced to the position calculations as it is visually-based and the acquisition and im-

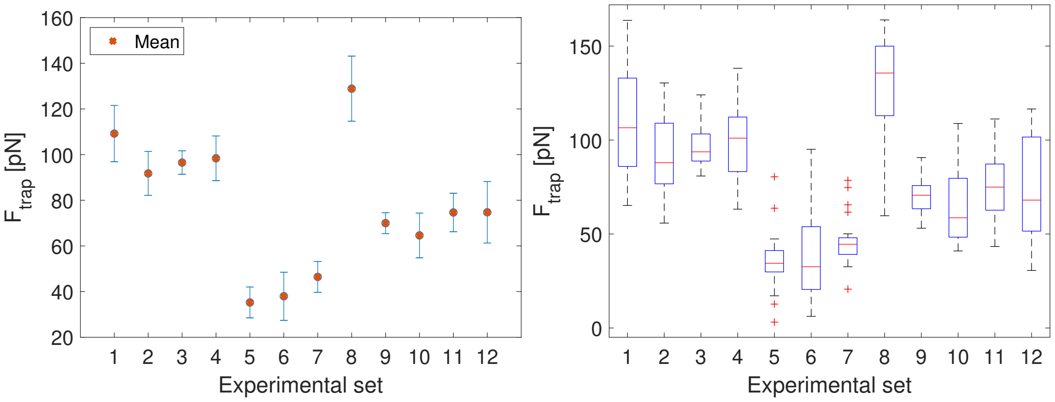

(a) Mean and standard deviation (b) Boxplot and median (red line)

Figure 6.27: Trapping force for disassembly for each experiment

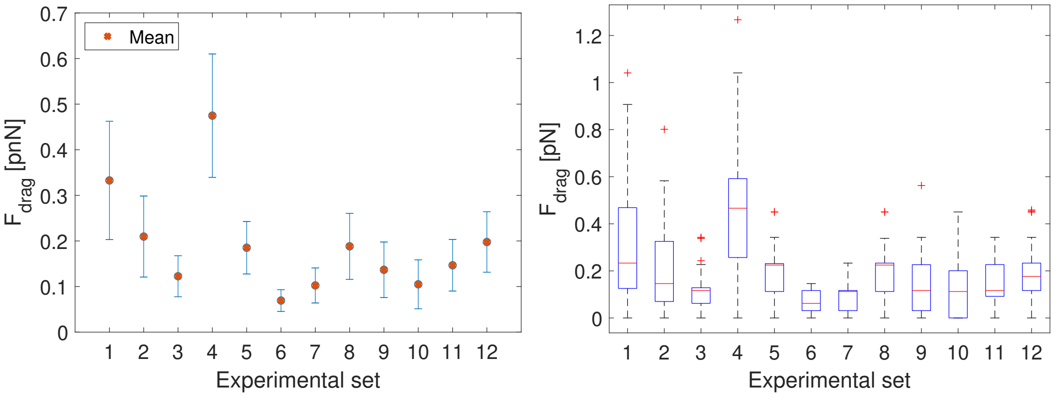

(a) Mean and standard deviation (b) Boxplot and median (red line)

Figure 6.28: Drag force for disassembly for each experiment

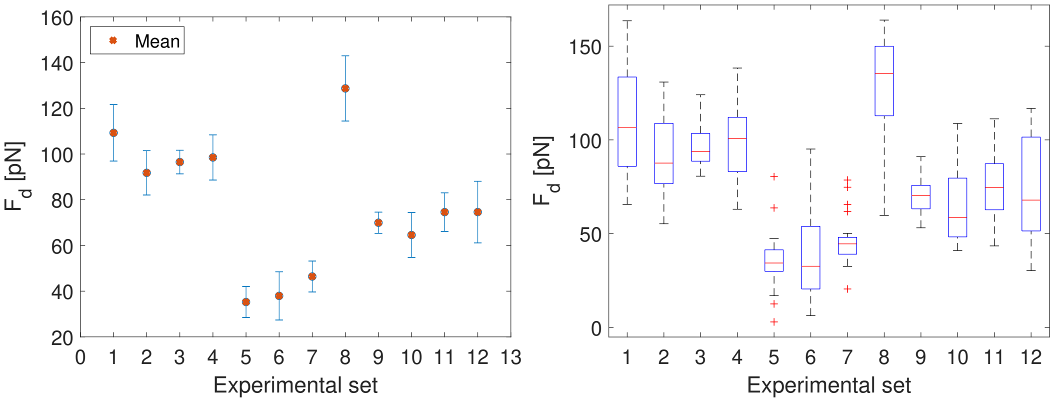

(a) Mean and standard deviation (b) Boxplot and median (red line)

Figure 6.29: Total force for disassembly for each experiment

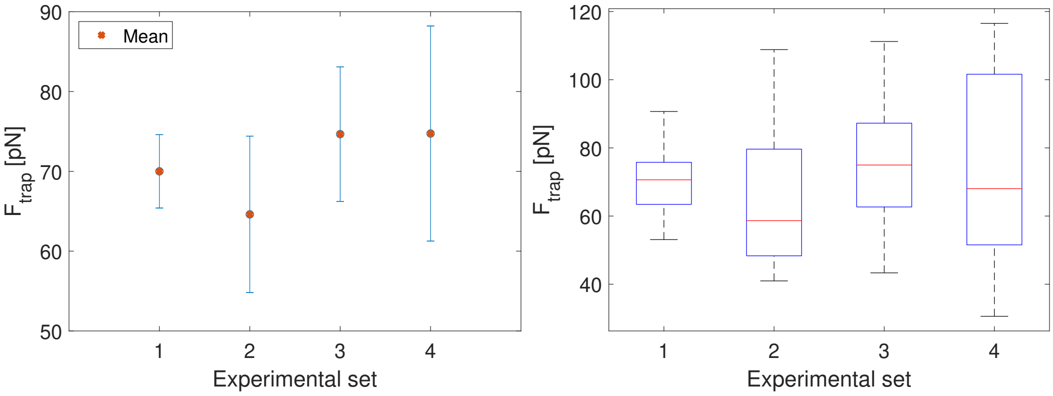

(a) Mean and standard deviation (b) Boxplot and median (red line)

Figure 6.30: Trapping force for disassembly for repeated disassembly on same experiment

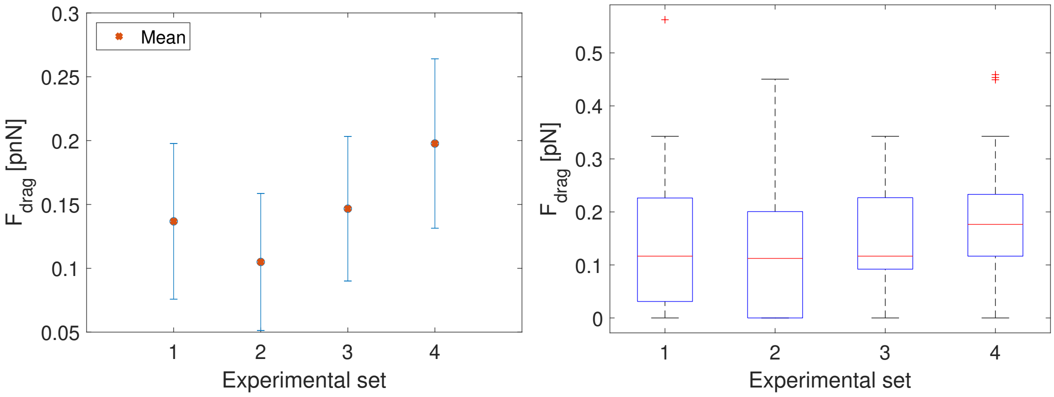

(a) Mean and standard deviation (b) Boxplot and median (red line)

Figure 6.31: Drag force for disassembly for repeated disassembly on same experiment

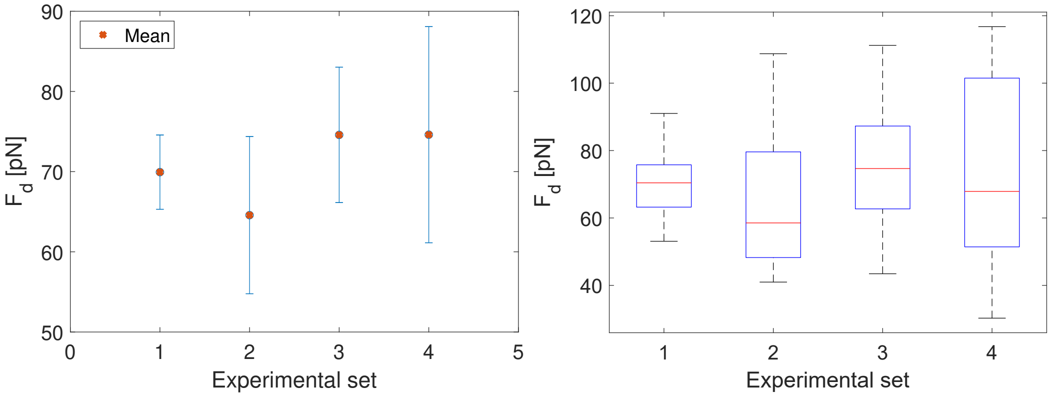

(a) Mean and standard deviation (b) Boxplot and median (red line)

Figure 6.32: Total force for disassembly for repeated disassembly on same experiment

Experiment	**Trapping force** [pN]	**Drag Force** [pN]	**Total Force** [pN]	**Laser Power** [W]
1	70.6367	0.1166	70.4255	0.3
2	58.6491	0.1123	58.5331	0.4
3	74.9763	0.1166	74.6601	0.4
4	68.0466	0.1765	67.8857	0.4

Table 6.5: Median of force norms and corresponding laser power for repeated joint disassembly motion

age processing can introduce noise. The laser positions that are used in the calculations are also obtained through image processing as the laser source and the camera have different sampling rates.

For the disassembly force, the median values of all recorded experiments range from 32.6 to 135.4 pN (Table 6.4). The same error in the position processing could have been introduced in the calculation of the disassembly force as for the displacement force. It is worth noting that, as the disassembly occurs at a brief time instant, it is difficult to accurately segment this part of the experiment from the video without including image frames from slightly before and after the assembly. Therefore, the median values include force values from time instances before and after the assembly. The segmented videos which are processed have durations from 1 to 1.5 seconds. From Table 6.4, it can also be seen that the drag force values are low as there is very little motion of the microrobot compared to the fluid. This shows that the drag force could be neglected in force model of eq. (6.41). Moreover, as the drag force is very low, the assumption for linearity does not introduce large errors for the specific experiment. Another source of value deviation is that the disassembly is performed on different pairs of microstructures. This implies that the material properties might vary and consequently result to different adhesion and magnetization between the microstructures. The variation in magnetization can result to differences to the attractive force between the components. The impact of the variance in magnetization and adhesion, which in turn define the amplitude of the contact force, can be seen more clearly from the results of the repeated motion on the same pair of microstructures (Table 6.5). In this case, the magnetization and adhesion is the same for every reported value as the experimental environment and microrobots are the same. The median disassembly force values for the 4 experimental sets given in Table 6.5 present a smaller deviation.

The nickel layer deposited on the microstructures for all sets of experiments is approximately 100 nm. It is worth noting that the reported value from the software of the deposition system for the layer thickness presents a deviation from the real value (experimentally observed to be up to 20 nm), and that could also attribute to the deviation in the magnetization and contact force. Increasing the thickness of the nickel layer would result to increased attractive forces between the components and, therefore, more stable assemblies. However, a thicker layer would interfere with the optical trap at the interface of the metal layer and the polymer part where the spherical handle is. In case of interference, grasping of the microstructure is compromised as the microstructure is pushed rather than grasped. Inadvertent heating can also be caused inducing flows and moving the assemblies. An increase on the layer thickness, while avoiding interference with the optical trap, could be compensated by increasing the length of the cylinder. However, this would lead to the assembly of heavier kinematic chain with less DoF as this would limit the number of microstructures that can be linked in a kinematic chain.

Last, as mentioned in assumption 3 of Section 6.4.6, the total drag force experienced by the assembly is calculated as the sum of the drag force exerted on each of the components. A more accurate approximation of the drag force and the drag coefficient could be obtained through a fluid dynamics simulation.

6.9 Conclusions

This chapter presented a methodology for reconfigurable microassembly using hybrid optical and magnetic microrobots. The proposed method uses Optical Tweezers to position the assembled microrobots while utilizes the magnetic field to magnetize the microrobots and induce a magnetic attractive force between the microstructures. An experimental setup is proposed integrating a set of three magnetic coils with the Optical Tweezers for simultaneous optical and magnetic actuation. The microrobots are 3D-printed with a mask for selective metal deposition which is later removed during the microrobot detachment process. The dynamics of the systems along with two system identification algorithms for trapping stiffness and drag force calibration were also presented. An experimental demonstration of the assembly and disassembly process is described. Tthe displacement and disassembly forces were experimentally estimated based on an set of microassembly experiments providing a range for the force values. Sources of error in estimation are: the different experimental conditions and set of microrobots used every experiment, the variance in magnetization of the microrobots and the assumption made in the force modelling. Future improvements would be to add more degrees of freedom to the individual microassembly components. For example, more optical handles could be added for improved manipulation or their geometry could be extended to 3D designs with surfaces for component attachment to more 3D planes.

Chapter 7

Conclusions

Micromanipulation systems are an emerging technology that could transform biology and medicine. Due to their fine resolution and size, their applications span from diagnosis to therapy and surgical interventions. Currently, cell manipulation is performed using primitive tools, such as micropipettes. However, recent advances in microfabrication have sparked the development of 3D microtools and microrobots. Meanwhile, data-driven decision making algorithms became prominent, something that was triggered by an increase in hardware computing power and large-scale data analysis. Therefore, such innovations can now allow the development of externally powered 3D microrobots for cell biopsies and cell manipulation used in enclosed environments, such as microfluidic chips, enhanced with state-of-the-art software solutions for microrobot 3D detection and manipulation using the direct line of sight for the camera. This thesis focused on the development of a micromanipulation system based on Optical Tweezers manipulation using 3D-printed microrobots, either purely optical or hybrid optical and magnetic, for micromanipulation and microassembly. Several methods for 3D microrobot pose estimation were presented. Optical Tweezers and magnetic actuation were also combined in a unified setup integrated with the Optical Tweezers to introduce a reversible microassembly method of microrobot assemblies.

Chapter 2 presented an overview of the current state-of-the-art on micromanipulation systems on the aspects of microrobot design and fabrication techniques, pose estimation and manipulation. From this review, it could be identified multiple component articulated microrobots could be proposed as a manipulation mechanism in the microscale. Moreover, pose estimation techniques in the microscale have been primarily based on traditional computer vision techniques mostly for 2D position and orientation estimation. Micromanipulation interfaces could also benefit from facilitating bimanual control of multiple microrobots which is challenging to do so using a video game controller or a mouse.

Chapter 3 introduced the fabrication method of multiple component optical microrobots and hybrid optically and magnetically actuated microrobots to be used for reconfigurable microassembly. Optical multiple component microrobots are fabricated through one-step printing. It was demonstrated that low printing powers results to higher feature resolution. Hybrid optical and magnetic microrobots are fabricated through a two-step procedure consisting of printing and metal deposition. In order to achieve selective metal deposition for simultaneous optical and magnetic actuation, a mask which is later removed is printed in order to cover specific microrobot surfaces that serve as grasping handles for the Optical Tweezers. The single step method allows fabrication of more complex geometries, however they are purely actuated by the Optical Tweezers and the design should take into account the minimum spacing between the components resulting to backlash. Hybrid optical and magnetic microrobots can be created from basic geometries and can allow simultaneous optical and magnetic actuation through selective metal deposition. The assembly procedure was described later on in Chapter 6.

Chapter 4 investigated the problem of three-dimensional microrobot pose estimation in an Optical Tweezers setup. Taking advantage of the camera in the setup, that the geometrical model of the microrobot is known and that the selected fabrication method allows batch microrobot printing in known configurations, a large dataset was generated to be used as ground truth for network training and validation. The first approach utilized sharpness information to relate the blurriness of the image, either as a whole or in specific regions of it, to the corresponding depth. However, this method is not robust to simultaneous microrobot translation and rotation as it cannot decouple these two motions using sharpness as a single feature. The CNN-LSTM method for depth estimation that was presented could estimate the corresponding depth for a microrobot independently of their orientation. The pose of the microrobot was estimated using CNNs for depth and relative orientation estimation of the microrobot using as input the current and previous frame. The validation results showed that there is a drift in the absolute orientation value as the estimations are relative and, therefore, that could be solved by updating the registration using a feature matching method. The main motivation of estimating microrobot pose is to provide a 3D position and orientation feedback of a 3D-printed microrobot in an enclosed environment such as the Optical Tweezers that could be potentially used as pose feedback for closed-loop control.

Having investigated some aspects on fabrication and microrobot 3D detection, the next step is microrobot manipulation. Chapter 5 demonstrated how indirect manipulation could be performed using 3D multiple component microrobots as grasping mechanisms. This approach addresses the problem of causing photodamage to cells by avoiding direct grasping with the laser while simultaneously allows out-of-plane object rotation. Optical manipulation of the utilized mechanisms could be improved by including geometrical figures that allow more stable grasping of the mechanism by the laser. The performed experiment also highlighted the fact that multiple optical traps are necessary for more dexterous microrobot manipulation. To this end, the next investigation focused on the development of a manipulation interface that integrates human sensory information to facilitate multiple microrobot manipulation. The comparative user results showed that object targeting was performed in a faster manner due to the seamless processing of the information from the gaze of the operator. The proposed manipulation interface could facilitate multiple microrobot manipulation in microassembly.

As mentioned, Optical Tweezers have many advantages that would benefit procedures such as microassembly. Microassembly methods proposed for the Optical Tweezers are mainly permanent as the components are chemically bonded. Alternatively, they can be assembled using 3D-printed components based on geometries that clamp together mechanically. Taking advantage of their fine spatial resolution that is significant for microassembly, a novel microassembly method was proposed integrating magnetic actuation with the Optical Tweezers. The motivation is to allow reversible and reconfigurable *in situ* microassembly using the magnetic force as the connecting force between the components. It was demonstrated that when the components are placed at a distance of approximately 1 μm, then they can be assembled when the magnetic field is activated and that they can be disassembled using the Optical Tweezers without deactivating the magnetic field. The force estimations for translation and disassembly appeared to be ranging from approximately 30 to 130 pN. The discrepancies could be attributed to the fact that the measurements were performed on different components hence the adhesion force differs. It was shown that when the assembly is performed on the same pair of components then the variations are smaller and the standard deviation of the force values was approximately 10 pN.

The aspiration is to include all of the developed components into one unified framework that would serve as a robotic master-slave system, similarly to macroscale surgical robot platforms, for *ex vivo* and *in vitro* cell manipulation.

Permissions

IEEE Permissions:

Does IEEE require individuals working on a thesis or dissertation to obtain formal permission for reuse?

The IEEE does not require individuals working on a thesis to obtain a formal reuse license, however, you must follow the requirements listed below:
Textual Material:
Using short quotes or referring to the work within these papers) users must give full credit to the original source (author, paper, publication) followed by the IEEE copyright line © IEEE.

Wiley Permissions:

Material Previously Published by One of the Named Authors - Where published in a Wiley journal or book

If you are the author of an article published in a Wiley journal and you wish to reuse a portion of your own article (or an amended version of it) in a new publication of which you are the author, editor or co-editor, the copyright or exclusive licence terms of the journal you published in will usually state that prior permission for re-use is not required (with the usual acknowledgements and subject to ethical guidelines around duplicate publication (see Section 3.5 of Wiley's Publication Ethics Best Practice Guidelines on Publishing Ethics). A formal grant of permission is not required, however if you wish to obtain one you can do so free of charge using the industry clearing house for permissions, RightsLink®.

Bibliography

[1] A. Darzi and Y. Munz, "The impact of minimally invasive surgical techniques," *Annu. Rev. Med.*, vol. 55, pp. 223–237, 2004.

[2] J. J. Abbott, Z. Nagy, F. Beyeler, and B. J. Nelson, "Robotics in the small: Part I Microrobotics," *IEEE Robotics and Automation Magazine*, vol. 14, no. 2, pp. 92–103, 2007.

[3] M. Power, A. J. Thompson, S. Anastasova, and G.-Z. Yang, "A monolithic force-sensitive 3d microgripper fabricated on the tip of an optical fiber using 2-photon polymerization," *Small*, vol. 14, no. 16, p. 1703964, 2018.

[4] J. Li, B. E.-F. de Ávila, W. Gao, L. Zhang, and J. Wang, "Micro/-nanorobots for biomedicine: Delivery, surgery, sensing, and detoxification," *Sci. Robot*, vol. 2, no. 4, pp. 1–9, 2017.

[5] A. Vikram Singh and M. Sitti, "Targeted drug delivery and imaging using mobile milli/microrobots: A promising future towards theranostic pharmaceutical design," *Current pharmaceutical design*, vol. 22, no. 11, pp. 1418–1428, 2016.

[6] F. Ullrich, S. Fusco, G. Chatzipirpiridis, S. Pané, and B. J. Nelson, "Recent progress in magnetically actuated microrobotics for ophthalmic therapies," *Eur. Ophthalmic Rev.*, vol. 8, pp. 120–126, 2014.

[7] T. L. Min, P. J. Mears, L. M. Chubiz, C. V. Rao, I. Golding, and Y. R. Chemla, "High-resolution, long-term characterization of bacterial motility using optical tweezers," *Nature methods*, vol. 6, no. 11, p. 831, 2009.

[8] M. H. Shabestari, A. Meijering, W. Roos, G. Wuite, and E. Peterman, "Recent advances in biological single-molecule applications of optical tweezers and fluorescence microscopy," in *Methods in enzymology.* Elsevier, 2017, vol. 582, pp. 85–119.

[9] P. Zorlutuna, N. Annabi, G. Camci-Unal, M. Nikkhah, J. M. Cha, J. W. Nichol, A. Manbachi, H. Bae, S. Chen, and A. Khademhosseini, "Microfabricated biomaterials for engineering 3d tissues," *Advanced materials*, vol. 24, no. 14, pp. 1782–1804, 2012.

[10] W. Hu, K. S. Ishii, Q. Fan, and A. T. Ohta, "Hydrogel microrobots actuated by optically generated vapour bubbles," *Lab on a Chip*, vol. 12, no. 19, pp. 3821–3826, 2012.

[11] K. C. Neuman, E. H. Chadd, G. F. Liou, K. Bergman, and S. M. Block, "Characterization of photodamage to escherichia coli in optical traps," *Biophysical journal*, vol. 77, no. 5, pp. 2856–2863, 1999.

[12] K. C. Neuman and A. Nagy, "Single-molecule force spectroscopy: optical tweezers, magnetic tweezers and atomic force microscopy," *Nature methods*, vol. 5, no. 6, p. 491, 2008.

[13] Y. Shen and T. Fukuda, "State of the art: micro-nanorobotic manipulation in single cell analysis," *Robotics and Biomimetics*, vol. 1, pp. 1–13, 2014.

[14] A. G. Banerjee, S. Chowdhury, and S. K. Gupta, "Optical Tweezers: Autonomous Robots for the Manipulation of Biological Cells," *IEEE Robotics and Automation Magazine*, 2014.

[15] G. Y. H. Lee and C. T. Lim, "Biomechanics approaches to studying human diseases," *Trends in Biotechnology*, vol. 25, no. 3, pp. 111–118, 2007.

[16] M. Dao, C. T. Lim, and S. Suresh, "Mechanics of the human red blood cell deformed by optical tweezers," *Journal of the Mechanics and Physics of Solids*, vol. 51, no. 11-12, pp. 2259–2280, 2003.

[17] Y. Tan, D. Sun, J. Wang, and W. Huang, "Mechanical characterization of human red blood cells under different osmotic conditions by robotic manipulation with optical tweezers," *IEEE Transactions on Biomedical Engineering*, vol. 57, no. 7, pp. 1816–1825, 2010.

[18] S. N. Bhatia and D. E. Ingber, "Microfluidic organs-on-chips," *Nature Biotechnology*, vol. 32, no. 8, pp. 760–772, 2014.

[19] H. Clevers, "Modeling development and disease with organoids," *Cell*, vol. 165, no. 7, pp. 1586–1597, 2016.

[20] J. Tenenbaum-Katan, A. Artzy-Schnirman, R. Fishler, N. Korin, and J. Sznitman, "Biomimetics of the pulmonary environment in vitro: A microfluidics perspective," *Biomicrofluidics*, vol. 12, no. 4, p. 042209, 2018.

[21] C. Probst, A. Grünberger, W. Wiechert, and D. Kohlheyer, "Microfluidic growth chambers with optical tweezers for full spatial single-cell control and analysis of evolving microbes," *Journal of Microbiological Methods*, vol. 95, no. 3, pp. 470–476, 2013.

[22] S. Chowdhury, P. Svec, C. Wang, K. T. Seale, J. P. Wikswo, W. Losert, and S. K. Gupta, "Automated cell transport in optical tweezers-assisted microfluidic chambers," *IEEE Transactions on Automation Science and Engineering*, vol. 10, no. 4, pp. 980–989, 2013.

[23] X. Wang, S. Chen, and D. Sun, "Robot-assisted automatic cell sorting with combined optical tweezer and microfluidic chip technologies," *Proceedings - IEEE International Conference on Robotics and Automation*, pp. 6003–6008, 2011.

[24] M. M. Wang, E. Tu, D. E. Raymond, J. M. Yang, H. Zhang, N. Hagen, B. Dees, E. M. Mercer, A. H. Forster, I. Kariv, P. J. Marchand, and W. F. Butler, "Microfluidic sorting of mammalian cells by optical force switching." *Nature biotechnology*, vol. 23, no. 1, pp. 83–87, 2005.

[25] J. Leach, H. Mushfique, R. di Leonardo, M. Padgett, and J. Cooper, "An optically driven pump for microfluidics," *Lab on a chip*, vol. 6, no. 6, pp. 735–739, 2006.

[26] T. Hasegawa, S. Sakuma, K. Nanatani, N. Uozumi, and F. Arai, "Mechanical Characterization System of Cyanobacteria Based on a Robot Integrated Microdluidic Chip," in *Intelligent Robots and Systems (IROS), 2015 IEEE/RSJ International Conference on*, 2015.

[27] H. Maruyama, R. Iitsuka, K. Onda, and F. Arai, "Massive parallel assembly of microbeads for fabrication of microtools having spheri-

cal structure and powerful laser manipulation," in *2010 IEEE International Conference on Robotics and Automation.* IEEE, 2010, pp. 482–487.

[28] H.-W. Huang, M. S. Sakar, K. Riederer, N. Shamsudhin, A. Petruska, S. Pané, and B. J. Nelson, "Magnetic microrobots with addressable shape control," in *2016 IEEE International Conference on Robotics and Automation (ICRA).* IEEE, 2016, pp. 1719–1724.

[29] E. Avci and G.-Z. Yang, "Development of a microhand using direct laser writing for indirect optical manipulation," in *2016 IEEE/RSJ International Conference on Intelligent Robots and Systems (IROS).* IEEE, 2016, pp. 5125–5130.

[30] S. Maruo, O. Nakamura, and S. Kawata, "Three-dimensional microfabrication with two-photon-absorbed photopolymerization," *Optics letters*, vol. 22, no. 2, pp. 132–134, 1997.

[31] S. Palagi, A. G. Mark, S. Y. Reigh, K. Melde, T. Qiu, H. Zeng, C. Parmeggiani, D. Martella, A. Sanchez-Castillo, N. Kapernaum, *et al.*, "Structured light enables biomimetic swimming and versatile locomotion of photoresponsive soft microrobots," *Nature materials*, vol. 15, no. 6, p. 647, 2016.

[32] M. Malinauskas, A. Žukauskas, V. Purlys, K. Belazaras, A. Momot, D. Paipulas, R. Gadonas, A. Piskarskas, H. Gilbergs, A. Gaidukevičiūtė, *et al.*, "Femtosecond laser polymerization of hybrid/integrated micro-optical elements and their characterization," *Journal of Optics*, vol. 12, no. 12, p. 124010, 2010.

[33] Y. Lin and J. Xu, "Microstructures fabricated by two-photon polymerization and their remote manipulation techniques: Toward 3d printing of micromachines," *Advanced Optical Materials*, vol. 6, no. 8, p. 1701359, 2018.

[34] S. Hu, H. Xie, T. Wei, S. Chen, and D. Sun, "Automated indirect transportation of biological cells with optical tweezers and a 3d printed microtool," *Applied Sciences*, vol. 9, no. 14, p. 2883, 2019.

[35] H. Zeng, P. Wasylczyk, D. S. Wiersma, and A. Priimagi, "Light robots: bridging the gap between microrobotics and photomechanics in soft materials," *Advanced Materials*, vol. 30, no. 24, p. 1703554, 2018.

[36] A. Ostendorf, R. Ghadiri, and S. Ksouri, "Optical tweezers in microassembly," in *Laser Applications in Microelectronic and Optoelectronic Manufacturing (LAMOM) XVIII*, vol. 8607. International Society for Optics and Photonics, 2013, p. 86070U.

[37] A. Barbot, "On-chip unthethered helical microrobot for force sensing applications," Ph.D. dissertation, Université Paris-Saclay, 2016.

[38] S. Kim, S. Lee, J. Lee, B. J. Nelson, L. Zhang, and H. Choi, "Fabrication and manipulation of ciliary microrobots with non-reciprocal magnetic actuation," *Scientific reports*, vol. 6, p. 30713, 2016.

[39] P. Liao, L. Xing, S. Zhang, and D. Sun, "Magnetically driven undulatory microswimmers integrating multiple rigid segments," *Small*, p. 1901197, 2019.

[40] S. Kim, F. Qiu, S. Kim, A. Ghanbari, C. Moon, L. Zhang, B. J. Nelson, and H. Choi, "Fabrication and characterization of magnetic micro-

robots for three-dimensional cell culture and targeted transportation," *Advanced Materials*, vol. 25, no. 41, pp. 5863–5868, 2013.

[41] H. Xia, J. Wang, Y. Tian, Q.-D. Chen, X.-B. Du, Y.-L. Zhang, Y. He, and H.-B. Sun, "Ferrofluids for fabrication of remotely controllable micro-nanomachines by two-photon polymerization," *Advanced Materials*, vol. 22, no. 29, pp. 3204–3207, 2010.

[42] M. S. Sakar, E. B. Steager, D. H. Kim, A. Agung Julius, M. Kim, V. Kumar, and G. J. Pappas, "Modeling, control and experimental characterization of microbiorobots," *The International Journal of Robotics Research*, vol. 30, no. 6, pp. 647–658, 2011.

[43] M. J. Villangca, D. Palima, A. R. Banas, and J. Glückstad, "Light-driven micro-tool equipped with a syringe function," *Light: Science & Applications*, vol. 5, no. 9, p. e16148, 2016.

[44] A. Zeng, K.-T. Yu, S. Song, D. Suo, E. Walker, A. Rodriguez, and J. Xiao, "Multi-view self-supervised deep learning for 6d pose estimation in the amazon picking challenge," in *2017 IEEE International Conference on Robotics and Automation (ICRA).* IEEE, 2017, pp. 1386–1383.

[45] M. Ye, L. Zhang, S. Giannarou, and G.-Z. Yang, "Real-time 3d tracking of articulated tools for robotic surgery," in *International Conference on Medical Image Computing and Computer-Assisted Intervention.* Springer, 2016, pp. 386–394.

[46] L. Zhang, M. Ye, P.-L. Chan, and G.-Z. Yang, "Real-time surgical tool tracking and pose estimation using a hybrid cylindrical marker," *In-*

ternational journal of computer assisted radiology and surgery, vol. 12, no. 6, pp. 921–930, 2017.

[47] M. A. Fischler and R. C. Bolles, “Random sample consensus: a paradigm for model fitting with applications to image analysis and automated cartography,” *Communications of the ACM*, vol. 24, no. 6, pp. 381–395, 1981.

[48] D. Chetverikov, D. Svirko, D. Stepanov, and P. Krsek, “The trimmed iterative closest point algorithm,” in *Object recognition supported by user interaction for service robots*, vol. 3. IEEE, 2002, pp. 545–548.

[49] S. Hinterstoisser, V. Lepetit, S. Ilic, S. Holzer, G. Bradski, K. Konolige, and N. Navab, “Model based training, detection and pose estimation of texture-less 3d objects in heavily cluttered scenes,” in *Asian conference on computer vision.* Springer, 2012, pp. 548–562.

[50] G. Pavlakos, X. Zhou, A. Chan, K. G. Derpanis, and K. Daniilidis, “6-dof object pose from semantic keypoints,” in *2017 IEEE International Conference on Robotics and Automation (ICRA).* IEEE, 2017, pp. 2011–2018.

[51] S. M. Seitz, B. Curless, J. Diebel, D. Scharstein, and R. Szeliski, “A comparison and evaluation of multi-view stereo reconstruction algorithms,” in *2006 IEEE Computer Society Conference on Computer Vision and Pattern Recognition (CVPR’06)*, vol. 1, June 2006, pp. 519–528.

[52] M. W. Tao, S. Hadap, J. Malik, and R. Ramamoorthi, “Depth from combining defocus and correspondence using light-field cameras,” in

Proceedings of the IEEE International Conference on Computer Vision, 2013, pp. 673–680.

[53] H. Tang, S. Cohen, B. Price, S. Schiller, and K. N. Kutulakos, "Depth from defocus in the wild," in *Proceedings of the IEEE Conference on Computer Vision and Pattern Recognition*, 2017, pp. 2740–2748.

[54] E. Kee, S. Paris, S. Chen, and J. Wang, "Modeling and removing spatially-varying optical blur," *2011 IEEE International Conference on Computational Photography, ICCP 2011*, 2011.

[55] S. Yazdanfar, K. B. Kenny, K. Tasimi, A. D. Corwin, E. L. Dixon, and R. J. Filkins, "Simple and robust image-based autofocusing for digital microscopy," *Optics express*, vol. 16, no. 12, pp. 8670–8677, 2008.

[56] A. Saxena, S. H. Chung, and A. Y. Ng, "Learning depth from single monocular images," in *Advances in neural information processing systems*, 2006, pp. 1161–1168.

[57] R. Ranftl, V. Vineet, Q. Chen, and V. Koltun, "Dense monocular depth estimation in complex dynamic scenes," in *2016 IEEE Conference on Computer Vision and Pattern Recognition (CVPR)*, June 2016, pp. 4058–4066.

[58] D. Xu, E. Ricci, W. Ouyang, X. Wang, and N. Sebe, "Multi-scale continuous crfs as sequential deep networks for monocular depth estimation," in *Proceedings of the IEEE Conference on Computer Vision and Pattern Recognition*, 2017, pp. 5354–5362.

[59] S. Gur and L. Wolf, "Single Image Depth Estimation Trained via Depth from Defocus Cues," *Computer Vision and Pattern Recognition (CVPR)*, pp. 7683–7692, 2019.

[60] J. L. Marins, X. Yun, E. R. Bachmann, R. B. McGhee, and M. J. Zyda, "An extended kalman filter for quaternion-based orientation estimation using marg sensors," in *Proceedings 2001 IEEE/RSJ International Conference on Intelligent Robots and Systems. Expanding the Societal Role of Robotics in the the Next Millennium (Cat. No. 01CH37180)*, vol. 4. IEEE, 2001, pp. 2003–2011.

[61] S. Hinterstoisser, V. Lepetit, S. Ilic, P. Fua, and N. Navab, "Dominant orientation templates for real-time detection of texture-less objects," in *2010 IEEE Computer Society Conference on Computer Vision and Pattern Recognition.* IEEE, 2010, pp. 2257–2264.

[62] I. Melekhov, J. Ylioinas, J. Kannala, and E. Rahtu, "Relative camera pose estimation using convolutional neural networks," in *International Conference on Advanced Concepts for Intelligent Vision Systems.* Springer, 2017, pp. 675–687.

[63] B. Hou, N. Miolane, B. Khanal, M. C. Lee, A. Alansary, S. McDonagh, J. V. Hajnal, D. Rueckert, B. Glocker, and B. Kainz, "Computing cnn loss and gradients for pose estimation with riemannian geometry," in *International Conference on Medical Image Computing and Computer-Assisted Intervention.* Springer, 2018, pp. 756–764.

[64] K. Berk Yesin and B. Nelson, "Robust CAD model-based visual tracking for 3D microassembly using image space potentials," *2004 IEEE International Conference on Robotics and Automation (ICRA)*, no. April, pp. 1868–1873, 2004.

[65] B. Tamadazte, E. Marchand, S. Dembele, and N. Le Fort-Piat, "CAD Model-based Tracking and 3D Visual-based Control for MEMS Mi-

croassembly," *The International Journal of Robotics Research*, vol. 29, no. 11, pp. 1416–1434, 2010.

[66] Z. Ni, A. Bolopion, J. Agnus, R. Benosman, and S. Régnier, "Asynchronous event-based visual shape tracking for stable haptic feedback in microrobotics," *IEEE Transactions on Robotics*, vol. 28, no. 5, pp. 1081–1089, 2012.

[67] C. Bergeles, B. E. Kratochvil, and B. J. Nelson, "Visually servoing magnetic intraocular microdevices," *IEEE Transactions on Robotics*, vol. 28, no. 4, pp. 798–809, 2012.

[68] A. Barbot, D. Decanini, and G. Hwang, "On-chip Microfluidic Multimodal Swimmer toward 3D Navigation," *Scientific Reports*, vol. 6, no. January, p. 19041, 2016.

[69] B. E. Kratochvil, L. Dong, and B. J. Nelson, "Real time Rigid-body Visual tracking in a Scanning Electron Microscope," *Int. J. Robotics Research*, vol. 28, no. 4, pp. 488–511, 2009.

[70] L. Cui, E. Marchand, S. Haliyo, and S. Regnier, "Three-Dimensional visual tracking and pose estimation in Scanning Electron Microscopes," *2016 IEEE/RSJ International Conference on Intelligent Robots and Systems (IROS)*, pp. 5210–5215, 2016.

[71] N. Marturi, B. Tamadazte, S. Dembélé, and N. Piat, "Visual servoing-based depth-estimation technique for manipulation inside sem," *IEEE Transactions on Instrumentation and Measurement*, vol. 65, no. 8, pp. 1847–1855, Aug 2016.

[72] S. Fatikow, V. Eichhorn, T. Wich, C. Dahmen, T. Sievers, K. N. Andersen, K. Carlson, and P. Bøggild, "Depth-detection methods for micro-

gripper based CNT manipulation in a scanning electron microscope," *Journal of Micro-Nano Mechatronics*, vol. 4, no. 1-2, pp. 27–36, 2008.

[73] M. Boissenin, J. Wedekind, A. N. Selvan, B. P. Amavasai, F. Caparrelli, and J. R. Travis, "Computer vision methods for optical microscopes," *Image and Vision Computing*, vol. 25, no. 7, pp. 1107–1116, 2007.

[74] A. V. Kudryavtsev, S. Dembélé, and N. Piat, "Full 3d rotation estimation in scanning electron microscope," in *2017 IEEE/RSJ International Conference on Intelligent Robots and Systems (IROS)*. IEEE, 2017, pp. 1134–1139.

[75] A. G. Banerjee and S. K. Gupta, "Research in automated planning and control for micromanipulation," *IEEE Transactions on Automation Science and Engineering*, vol. 10, no. 3, pp. 485–495, 2013.

[76] A. Ashkin, "Acceleration and trapping of particles by radiation pressure," *Physical review letters*, vol. 24, no. 4, p. 156, 1970.

[77] ——, "Forces of a single-beam gradient laser trap on a dielectric sphere in the ray optics regime," *Biophysical journal*, vol. 61, no. 2, pp. 569–582, 1992.

[78] R. Gauthier and S. Wallace, "Optical levitation of spheres: analytical development and numerical computations of the force equations," *JOSA B*, vol. 12, no. 9, pp. 1680–1686, 1995.

[79] R. Gauthier, "Theoretical investigation of the optical trapping force and torque on cylindrical micro-objects," *JOSA B*, vol. 14, no. 12, pp. 3323–3333, 1997.

[80] D. Phillips, M. Padgett, S. Hanna, Y.-L. Ho, D. Carberry, M. Miles, and S. Simpson, “Shape-induced force fields in optical trapping,” *Nature Photonics*, vol. 8, no. 5, p. 400, 2014.

[81] T. Nieminen, H. Rubinsztein-Dunlop, and N. Heckenberg, “Calculation and optical measurement of laser trapping forces on non-spherical particles,” *Journal of Quantitative Spectroscopy and Radiative Transfer*, vol. 70, no. 4-6, pp. 627–637, 2001.

[82] C. Aguilar-Ibañez and L. I. S. Suarez-Castanon, Miguel and Rosas-Soriano, “A simple control scheme for the manipulation of a particle by means of optical tweezers,” *International Journal of Robust and Nonlinear Control*, vol. 18, no. May 2010, pp. 557–569, 2010.

[83] A. Ranaweera and B. Bamieh, “Modelling, identification, and control of a spherical particle trapped in an optical tweezer,” *International Journal of Robust and Nonlinear Control*, vol. 15, no. 16, pp. 747–768, 2005.

[84] H. Chen, C. Wang, and D. Sun, “Dynamics calibration of optically trapped cells with adaptive control technology,” *2013 IEEE International Conference on Robotics and Automation (ICRA)*, pp. 2801–2806, 2013.

[85] C. C. Cheah, X. Li, X. Yan, and D. Sun, “Observer-based optical manipulation of biological cells with robotic tweezers,” *IEEE Transactions on Robotics*, vol. 30, no. 1, pp. 68–80, 2014.

[86] X. Li, C. C. Cheah, S. Hu, and D. Sun, “Dynamic trapping and manipulation of biological cells with optical tweezers,” *Automatica*, vol. 49, no. 6, pp. 1614–1625, 2013.

[87] M. Xie, J. K. Mills, Y. Wang, M. Mahmoodi, and D. Sun, "Automated Translational and Rotational Control of Biological Cells with a Robot-Aided Optical Tweezers Manipulation System," *IEEE Transactions on Automation Science and Engineering*, vol. 13, no. 2, pp. 543–551, 2016.

[88] N. Amari, D. Folio, and A. Ferreira, "Motion of a Micro/Nanomanipulator using a Laser Beam Tracking System," *International Journal of Optomechatronics*, vol. 9612, no. August, pp. 1–18, 2014.

[89] X. Yan, C. C. Cheah, Q. M. Ta, and Q.-c. Pham, "Stochastic Dynamic Trapping in Robotic Manipulation of Micro-Objects Using," *IEEE Transaction on Robotics*, vol. 32, no. 3, pp. 499–512, 2016.

[90] A. G. Banerjee, A. Pomerance, W. Losert, and S. K. Gupta, "Developing a Stochastic Dynamic Programming Framework for Optical Tweezer-Based Automated Particle Transport Operations," *IEEE Transactions on Automation Science and Engineering*, vol. 7, no. 2, pp. 218–227, 2010.

[91] X. Li, H. Yang, H. Huang, and D. Sun, "A Switching Controller for High Speed Cell Transfer with A Robot-aided Optical Tweezers Manipulation System," *2015 IEEE/RSJ International Conference on Intelligent Robots and Systems (IROS)*, pp. 766–771, 2015.

[92] Y. Wu, D. Sun, W. Huang, and N. Xi, "Dynamics Analysis and Motion Planning for Automated Cell Transportation," *IEEE/ASME Transactions on mechatronics*, vol. 18, no. 2, pp. 706–713, 2013.

[93] F. Arai, T. Endo, R. Yamuchi, and T. Fukuda, "3D 6DOF Manipulation of Micro-object Using Laser Trapped Microtool," in *Robotics and*

Automation, 2006. ICRA 2006. Proceedings 2006 IEEE International Conference on. IEEE, 2006, pp. 1390–1395.

[94] F. Arai, T. Endo, H. Maruyama, T. Fukuda, T. Shimizu, and S. Kamiya, "3D Manipulation of lipid nanotubes using laser trapped functional gel microbeads," *2007 IEEE/RSJ International Conference on Intelligent Robots and Systems*, pp. 3125–3130, 2007.

[95] F. Arai, K. Onda, R. Iitsuka, and H. Maruyama, "Multi-beam laser micromanipulation of microtool by integrated optical tweezers," *Proceedings - IEEE International Conference on Robotics and Automation*, pp. 1832–1837, 2009.

[96] S. Chowdhury, P. Svec, C. Wang, W. Losert, and S. K. Gupta, "Gripper synthesis for indirect manipulation of cells using holographic optical tweezers," *Proceedings - IEEE International Conference on Robotics and Automation*, pp. 2749–2754, 2012.

[97] C. C. Cheah, Q. M. Ta, and R. Haghighi, "Grasping and manipulation of a micro-particle using multiple optical traps," *Automatica*, vol. 68, pp. 216–227, 2016.

[98] A. Thakur, S. Chowdhury, P. Vec, C. Wang, W. Losert, and S. K. Gupta, "Indirect pushing based automated micromanipulation of biological cells using optical tweezers," *The International Journal of Robotics Research*, vol. 33, no. 8, pp. 1098–1111, 2014.

[99] R. Haghighi and C. C. Cheah, "Multi-group coordination control for robot swarms," *Automatica*, vol. 48, no. 10, pp. 2526–2534, 2012.

[100] H. Chen and D. Sun, “Moving Groups of Microparticles Into Array With a Robot–Tweezers Manipulation System,” *IEEE Transactions on Robotics*, vol. 28, no. 5, pp. 1069–1080, 2012.

[101] ——, “Swarm-inspired transportation of biological cells using saturation-controlled optical tweezers,” in *2015 IEEE International Conference on Robotics and Automation (ICRA)*, May 2015, pp. 3531–3536.

[102] R. Haghighi and C. C. Cheah, “Optical Manipulation of Multiple Groups of Microparticles using Robotic Tweezers Optical Manipulation of Multiple Groups of Microparticles using,” *IEEE Transactions on Robotics*, vol. 32, no. April, pp. 275–285, 2016.

[103] F. Arai, M. Ogawa, and T. Fukuda, “Bilateral control system for laser micromanipulation by force feedback,” *Advanced Robotics*, vol. 14, no. 5, pp. 381–383, 2000.

[104] W. Vogl, B. K. L. Ma, and M. Sitti, “Augmented reality user interface for an atomic force microscope-based nanorobotic system,” *IEEE Transactions on Nanotechnology*, vol. 5, no. 4, pp. 397–406, 2006.

[105] A. Bolopion, H. Xie, D. Haliyo, and S. Regnier, “3D haptic handling of microspheres,” in *Intelligent Robots and Systems (IROS), 2010 IEEE/RSJ International Conference on*, Oct 2010, pp. 6131–6136.

[106] C. Pacoret, R. Bowman, G. Gibson, S. Haliyo, D. Carberry, A. Bergander, S. Régnier, and M. Padgett, “Touching the microworld with force-feedback optical tweezers.” *Optics express*, vol. 17, no. 12, pp. 10 259–10 264, 2009.

[107] Z. Ni, C. Pacoret, R. Benosman, and S. Regnier, “2D high speed force feedback teleoperation of optical tweezers,” *2013 IEEE International Conference on Robotics and Automation (ICRA)*, pp. 1700–1705, 2013.

[108] S. A. Bowyer, B. L. Davies, and F. R. y Baena, “Active constraints/virtual fixtures: A survey,” *IEEE Transactions on Robotics*, vol. 30, no. 1, pp. 138–157, 2013.

[109] C. Basdogan, A. Kiraz, I. Bukusoglu, A. Varol, and S. Doganay, “Haptic guidance for improved task performance in steering microparticles with optical tweezers,” *Optics Express*, vol. 15, no. 18, p. 11616, 2007.

[110] M. Ammi and A. Ferreira, “Robotic assisted micromanipulation system using virtual fixtures and metaphors,” *2007 IEEE International Conference on Robotics and Automation (ICRA)*, no. April, pp. 454–460, 2007.

[111] A. Bolopion, B. Cagneau, D. S. Haliyo, and S. Régnier, “Analysis of stability and transparency for nanoscale force feedback in bilateral coupling,” *Journal of Micro-Nano Mechatronics*, vol. 4, no. 4, pp. 145–158, 2009.

[112] K. B. Yesin, K. Vollmers, and B. J. Nelson, “Modeling and control of untethered biomicrorobots in a fluidic environment using electromagnetic fields,” *The International Journal of Robotics Research*, vol. 25, no. 5-6, pp. 527–536, 2006.

[113] N. Dechev, W. L. Cleghorn, and J. K. Mills, “Microassembly of 3-d microstructures using a compliant, passive microgripper,” *Journal of Microelectromechanical Systems*, vol. 13, no. 2, pp. 176–189, April 2004.

[114] D. Heriban and M. Gauthier, “Robotic micro-assembly of microparts using a piezogripper,” in *2008 IEEE/RSJ International Conference on Intelligent Robots and Systems*, Sep. 2008, pp. 4042–4047.

[115] Han Zhang, Y. Bellouard, E. Burdet, R. Clavel, A. . Poo, and D. W. Hutamacher, “Shape memory alloy microgripper for robotic microassembly of tissue engineering scaffolds,” in *IEEE International Conference on Robotics and Automation, 2004. Proceedings. ICRA ’04. 2004*, vol. 5, April 2004, pp. 4918–4924 Vol.5.

[116] W. Hu, K. S. Ishii, and A. T. Ohta, “Micro-assembly using optically controlled bubble microrobots,” *Applied Physics Letters*, vol. 99, no. 9, p. 094103, 2011.

[117] K. B. Yesin and B. J. Nelson, “A cad model based tracking system for visually guided microassembly,” *Robotica*, vol. 23, no. 4, pp. 409–418, 2005.

[118] M. Rakotondrabe, I. A. Ivan, S. Khadraoui, C. Clevy, P. Lutz, and N. Chaillet, “Dynamic displacement self-sensing and robust control of cantilever piezoelectric actuators dedicated for microassembly,” in *2010 IEEE/ASME International Conference on Advanced Intelligent Mechatronics*. IEEE, 2010, pp. 557–562.

[119] D. J. Cappelleri, M. Fatovic, and U. Shah, “Caging micromanipulation for automated microassembly,” in *2011 IEEE International Conference on Robotics and Automation*. IEEE, 2011, pp. 3145–3150.

[120] A. Bolopion, H. Xie, D. S. Haliyo, and S. Régnier, “Haptic teleoperation for 3-d microassembly of spherical objects,” *IEEE/ASME Transactions on Mechatronics*, vol. 17, no. 1, pp. 116–127, 2010.

[121] B. R. Donald, C. G. Levey, and I. Paprotny, "Planar microassembly by parallel actuation of mems microrobots," *Journal of Microelectromechanical Systems*, vol. 17, no. 4, pp. 789–808, 2008.

[122] W.-M. Shen, H. C. Chiu, M. Rubenstein, and B. Salemi, "Rolling and climbing by the multifunctional superbot reconfigurable robotic system," in *AIP Conference Proceedings*, vol. 969, no. 1. AIP, 2008, pp. 839–848.

[123] E. Diller, C. Pawashe, S. Floyd, and M. Sitti, "Assembly and disassembly of magnetic mobile micro-robots towards deterministic 2-d reconfigurable micro-systems," *The International Journal of Robotics Research*, vol. 30, no. 14, pp. 1667–1680, 2011.

[124] A. Terray, J. Oakey, and D. W. Marr, "Fabrication of linear colloidal structures for microfluidic applications," *Applied Physics Letters*, vol. 81, no. 9, pp. 1555–1557, 2002.

[125] P. J. Rodrigo, L. Kelemen, D. Palima, C. A. Alonzo, P. Ormos, and J. Glückstad, "Optical microassembly platform for constructing reconfigurable microenvironments for biomedical studies," *Optics Express*, vol. 17, no. 8, pp. 6578–6583, 2009.

[126] J.-M. Geusebroek, F. Cornelissen, A. W. Smeulders, and H. Geerts, "Robust autofocusing in microscopy," *Cytometry: The Journal of the International Society for Analytical Cytology*, vol. 39, no. 1, pp. 1–9, 2000.

[127] J. L. Pech-Pacheco, G. Cristóbal, J. Chamorro-Martinez, and J. Fernández-Valdivia, "Diatom autofocusing in brightfield microscopy:

a comparative study," in *Proceedings 15th International Conference on Pattern Recognition. ICPR-2000*, vol. 3. IEEE, 2000, pp. 314–317.

[128] K. Simonyan and A. Zisserman, "Very deep convolutional networks for large-scale image recognition," *arXiv preprint arXiv:1409.1556*, 2014.

[129] J. Deng, W. Dong, R. Socher, L.-J. Li, K. Li, and L. Fei-Fei, "ImageNet: A Large-Scale Hierarchical Image Database," in *CVPR09*, 2009.

[130] G. Z. Yang, G. P. Mylonas, K. W. Kwok, and A. Chung, "Perceptual docking for robotic control," *Lecture Notes in Computer Science (including subseries Lecture Notes in Artificial Intelligence and Lecture Notes in Bioinformatics)*, vol. 5128 LNCS, pp. 21–30, 2008.

[131] A. G. Banerjee, S. Chowdhury, W. Losert, and S. K. Gupta, "Survey on indirect optical manipulation of cells, nucleic acids, and motor proteins." *Journal of biomedical optics*, vol. 16, no. 5, p. 051302, 2011.

[132] K. Leibrandt, C. Bergeles, and G.-Z. Yang, "On-Line Collision-Free Inverse Kinematics with Frictional Active Constraints for Effective Control of Unstable Concentric Tube Robots," in *Intelligent Robots and Systems (IROS), 2015 IEEE/RSJ International Conference on*, 2015.

[133] M. Sitti, *Mobile Microrobotics.* MIT Press, 2017.

[134] A. Khan and J. Richardson, "The resistance to motion of a solid sphere in a fluid," *Chemical Engineering Communications*, vol. 62, no. 1-6, pp. 135–150, 1987.

[135] B. R. Munson, D. F. Young, and T. H. Okiishi, "Fundamentals of fluid mechanics," *Oceanographic Literature Review*, vol. 10, no. 42, p. 831, 1995.

[136] D. S. Lemons, A. Gythiel, and P. Langevin's, "paper "on the theory of brownian motion"["sur la théorie du mouvement brownien," cr acad. sci.(paris) 146, 530–533 (1908)]," *Am. J. Phys*, vol. 65, no. 11, pp. 1079–1081, 1997.

[137] T. W. R. Fountain, P. V. Kailat, and J. J. Abbott, "Wireless control of magnetic helical microrobots using a rotating-permanent-magnet manipulator," in *2010 IEEE International Conference on Robotics and Automation*, May 2010, pp. 576–581.

[138] R. M. Murray, *A mathematical introduction to robotic manipulation.* CRC press, 2017.

[139] A. Barbot, D. Decanini, and G. Hwang, "Helical microrobot for force sensing inside microfluidic chip," *Sensors and Actuators A: Physical*, vol. 266, pp. 258–272, 2017.

[140] M. Sarshar, W. Wong, and B. Anvari, "Comparative study of methods to calibrate the stiffness of a single-beam gradient-force optical tweezers over various laser trapping powers," *Journal of biomedical optics*, vol. 19, no. 11, p. 115001, 2014.

[141] E.-L. Florin, A. Pralle, E. Stelzer, and J. Hörber, "Photonic force microscope calibration by thermal noise analysis," *Applied Physics A: Materials Science & Processing*, vol. 66, pp. S75–S78, 1998.